

**FACULTY
OF MATHEMATICS
AND PHYSICS**
Charles University

DOCTORAL THESIS

Vít Zajac

**Ultrafast response of electrons
in nanostructured and disordered semiconductor systems
studied by time-resolved terahertz spectroscopy**

Institute of Physics of the Czech Academy of Sciences

Supervisor of the doctoral thesis: doc. RNDr. Petr Kužel, Ph.D.

Study programme: Physics

Specialization: Quantum Optics and Optoelectronics

Prague 2017

I declare that I carried out this doctoral thesis independently, and only with the cited sources, literature and other professional sources.

I understand that my work relates to the rights and obligations under the Act No. 121/2000 Coll., the Copyright Act, as amended, in particular the fact that the Charles University has the right to conclude a license agreement on the use of this work as a school work pursuant to Section 60 paragraph 1 of the Copyright Act.

In..... date.....

Vít Zajac

Acknowledgements

I would like to express my gratitude to my supervisor, doc. RNDr. Petr Kužel, Ph.D., for his scholarly guidance during my Ph.D. research. He is always willing to share his valuable research experience and his scientific knowledge in an instructive way. I especially appreciate that he trained me in experimental precision and that he always emphasized the educational dimension of publications in our group. His comments and discussions on this work were invaluable. I am very grateful to my advisor, Mgr. Hynek Němec, Ph.D., for all the theoretical and experimental help he keenly gave me. His research enthusiasm and his theoretical knowledge are an inspiration for me. I thank him also for providing me with the source code of the Monte Carlo calculation program and introducing me into the code so that I could adapt the program myself for the purpose of this work.

My work on nanoporous Si nanocrystals would not be possible without the cooperation with prof. RNDr. Ivan Pelant, DrSc. and RNDr. Kateřina Kůsová, Ph.D. who provided us the samples and discussed the unexpected results with us. My thanks also go to RNDr. Ivan Rychetský, CSc. from whose calculations stems the main theoretical model of this work. I thank Dr. Sebastian Gutsch (University of Freiburg) for the set of silicon nanocrystal superlattice samples and Dr. Patrick Mounaix (University of Bordeaux) with Dr. Mario Maglione (French National Center for Scientific Research) for the rutile monocrystal I investigated in this work.

I thank all my colleagues at the Department of Dielectrics, Institute of Physics for creating a pleasant and helpful atmosphere. Namely, I thank Ing. Jiří Hlinka, Ph.D. — the head of the Department — he puts his heart into leading this friendly and scientifically sound collective. I esteem prof. RNDr. Petr Malý, DrSc. — the head of my study specialization at Charles University — for being an example of a kind, erudite and respectful teacher. I am thankful to my colleagues, Ing. Christelle Kadlec, Dr. and Mgr. Filip Kadlec, Dr. for their personal support and experimental help during all my work. I thank to my fellow students Mgr. Volodymyr Skoromets, Ph.D. and Ing. Filip Dominec, Ph.D. for their helpfulness in the laboratory and Mgr. Zoltán Mics, Ph.D. — my predecessor in the THz group — that he lent me the manuscript of his doctoral thesis in order to help me in entering the research field.

I am grateful to my family and all my friends for supporting me throughout my study and work, for their confidence and patience.

I dedicate this work to my wife Blanka and our children.

Title: Ultrafast response of electrons in nanostructured and disordered semiconductor systems studied by time-resolved terahertz spectroscopy

Author: Vít Zajac

Department / Institute: Institute of Physics of the Czech Academy of Sciences

Supervisor of the doctoral thesis: doc. RNDr. Petr Kužel, Ph.D., Institute of Physics of the Czech Academy of Sciences

Abstract: This thesis deals with charge transport in semiconducting nanomaterials on the picosecond time scale studied by time-resolved terahertz spectroscopy. The problematics of the effective response of composite materials is reviewed and the VBD effective medium model is formulated. The wave equation for the THz probing pulse propagating through inhomogeneously excited percolated and non-percolated semiconducting nanomaterials is solved. This theory is used to investigate charge transport in samples of nanoporous-Si-derived nanocrystals and in epitaxial Si nanocrystal superlattices. The experimental spectra are successfully modeled with the use of Monte Carlo calculations of charge carrier mobility in nanocrystals of corresponding sizes and degrees of percolation within the VBD approximation. It is found that the sample signal in THz and optical methods is dominated by nanocrystals from different regions of the nanocrystal size distribution. THz photoconductivity in bulk rutile is investigated after strong inhomogeneous photoexcitation. Mobility of polarons is decreased by an order of magnitude due to electron-hole scattering in the high-density region and increases upon ambipolar diffusion of polarons into less densely populated regions of the sample on the picosecond time scale at low temperatures. At room temperature, a nanosecond-lasting 50% increase of rutile permittivity is observed at high carrier densities.

Keywords: semiconducting nanomaterial, charge transport, time-domain terahertz spectroscopy, effective medium approximation.

Contents

1. Introduction	1
1.1. Conductivity of nanomaterials.....	1
1.2. Relevance of terahertz to nanometer.....	2
1.3. Effective response challenge.....	3
1.4. Structure of the thesis.....	3
2. THz spectroscopy	5
2.1. Terahertz spectral range.....	5
2.2. Time-domain spectroscopy.....	8
2.3. Optical pump–THz probe spectroscopy.....	10
2.3.1. <i>Spectrally averaged transient THz kinetics</i>	13
2.4. Experimental setup.....	14
3. THz spectroscopy of nanomaterials in the literature	20
3.1. Drude model.....	21
3.2. Hopping.....	22
3.3. Localized plasmon	23
3.4. Effective medium response.....	24
3.4.1. <i>Maxwell Garnett EMT</i>	26
3.4.2. <i>Bruggeman EMT</i>	27
3.4.3. <i>Bergman EMT</i>	28
3.5. Monte Carlo simulations of carrier confinement.....	30
3.6. Remarks on nanoscale conductivity.....	31
3.7. Drude-Smith model.....	32
3.8. Quantum confinement.....	34
3.9. Published experimental works	35
3.9.1. <i>Silicon micro- and nanocrystals</i>	35
3.9.2. <i>Titanium dioxide nanocrystals</i>	36
3.9.3. <i>InP, InGaAs, CdS, CdSe, VO₂ nanoparticles</i>	37
3.9.4. <i>Quantum wires, nanotubes</i>	38
4. VBD effective medium theory	40
4.1. Effective permittivity calculation	40
4.2. Equivalent electric circuit model	43
4.3. Application of the VBD model in Optical pump–THz probe experiments	46
4.4. Interpretation in terms of the Maxwell Garnett EMT	48
4.5. Relation to the Bergman EMT	49
4.5.1. <i>Spectral function analysis</i>	50
4.6. General character and limitations of the VBD effective medium model.....	51
5. Wave equation solution — measurable vs. local conductivity	54
5.1. Transient THz wave equation.....	54
5.2. Percolated semiconducting pathways and bulk samples	56
5.2.1. <i>Thin samples</i>	58
5.2.2. <i>Thick samples</i>	58

5.3.	Non-percolated semiconductor inclusions	58
5.3.1.	<i>Depth-profile of effective conductivity</i>	59
5.3.2.	<i>Solution of the wave equation in non-percolated case</i>	60
5.3.3.	<i>Thin film with strong absorption</i>	62
5.4.	General solution	62
5.4.1.	<i>Thick sample with strong absorption</i>	63
6.	Transport in Si-NCs derived from nanoporous Si	64
6.1.	The sample	64
6.1.1.	<i>Non-THz characterization</i>	65
6.1.2.	<i>Preparation of samples for THz measurements</i>	68
6.2.	THz photoconductivity	68
6.2.1.	<i>Measured spectra and fitting model</i>	70
6.2.2.	<i>Spectral oscillations</i>	75
6.3.	Discussion	76
6.4.	Conclusion	80
7.	Si-NC superlattices	81
7.1.	Sample morphology and optical properties	81
7.2.	THz photoconductivity	84
7.3.	Results and Discussion.....	87
7.4.	Kinetics	90
7.5.	Conclusion	91
8.	Dynamics of density-dependent response in bulk rutile	92
8.1.	Picosecond dynamics of charge transport at low temperatures	93
8.1.1.	<i>Published scattering model and data comparison</i>	94
8.1.2.	<i>The general plasma-diffusion model</i>	95
8.1.3.	<i>Kinetics and simplified analysis</i>	97
8.1.4.	<i>Results and discussion</i>	99
8.2.	Temperature dependence of average mobility	107
8.3.	Temperature dependent electron–hole recombination	108
8.3.1.	<i>Theory</i>	108
8.3.2.	<i>Discussion</i>	109
8.4.	Transient permittivity contribution at room temperature.....	113
8.5.	Conclusion	116
9.	Morphological interpretation of probabilistic parameters in Monte Carlo calculations of carrier mobility in nanomaterials	118
9.1.	Carrier mobility in the morphological regime	120
9.2.	Comparison of morphological and probabilistic regime.....	123
9.3.	Conclusion	124
10.	Conclusion	125
11.	Bibliography	129
12.	List of Tables	135

13. List of Abbreviations	136
13.1. Multi-letter abbreviations.....	136
13.2. Roman symbols and their derivatives	136
13.3. Greek symbols and their derivatives.....	140

1. Introduction

Many devices that have been traditionally made from bulk inorganic semiconductors are increasingly replaced by those produced by thin film technologies and nanotechnologies, which are less economically, energetically and environmentally demanding. The tendency is most prominent in the photovoltaic industry but occurs also in processing and transmitting of digital signals. Crystalline and polycrystalline silicon solar cells, which prevail in installed applications, have reached laboratory efficiency of 25% and 20% [1], respectively, but their production is rather expensive because it demands melting, purifying and slicing of large amounts of the source material. On the other hand, dye-sensitized and organic thin film cells reach efficiencies of “only” 11.9% and 11.0% [1], respectively, but thin film and inkjet printing production technologies enable fabrication of these devices with notably reduced energetic and economic costs and with other technological advantages e.g. their low thickness or flexibility.

In the areas of computational and communication technologies, a significant effort is also put into the research of nanoelements that have exceptional conduction properties (graphene, carbon nanotubes) or non-standard light–electricity conversion capabilities (tunable energy levels in nanodots due to quantum confinement, silicon nanocrystals with direct band gap etc.). [2]

This thesis deals with THz photoconductivity spectra of macroscopic (μm - to cm -sized) samples made of more or less ordered ensembles of nanometer-sized semiconducting particles and we use the term nanomaterial in this sense. Below we introduce the basic aspects of nanomaterial (photo)conductivity and show that our method is particularly useful for characterizing this application-decisive property of a various nanomaterials. The work is both theoretical and experimental covering also some methodological aspects. We present original results concerning the theory of macroscopic response of nanostructured materials in general and the implications of this theory for time-resolved THz spectroscopy in particular. We show and discuss our experimental results on nanomaterials made of two technologically important semiconductors: silicon and titanium dioxide, and a refinement of the Monte Carlo numerical method for calculating properties of short-range charge transport.

1.1. Conductivity of nanomaterials

Conduction properties of nanomaterials are closely related to their structure. The efficiency of the charge transport on the long range, which is essential for all electric and electro-optic applications, is limited by the slowest process that the charge carriers undergo on the short range. These microscopic processes include charge carrier generation, separation [3], intra- [4] and inter-nanoparticle motion [5]. However, they can be hardly unambiguously distinguished by contact measurements such as time-of-flight methods, which are usually employed, or in a field-effect transistor configuration. A local probe that senses the behavior of charge carriers on the nanometer length scale is crucial for characterization of the microscopic charge

transport and, subsequently, for the improvement of the macroscopic electric properties of nanomaterials.

Scanning tunneling microscopes with multiple tips allow measurements of the conductivity of individual nanowires [6] but they represent rather expensive devices demanding ultra-high vacuum conditions and are mostly used in combination with high-end sample preparation techniques such as molecular beam epitaxy or electron lithography. Devices whose production is up scalable usually contain more or less complex ensembles of nanoobjects with varying microscopic properties. A method able to sense the local motion of charge carriers and providing its average over the whole ensemble is required. The THz spectroscopy offers this possibility.

1.2. Relevance of terahertz to nanometer

Terahertz spectroscopy probes the interaction of charge carriers with electromagnetic *radiation* in the THz frequency range without any contacts attached to the sample and in an undemanding environment of dried air or primary vacuum. The measurable spectra of complex optical conductivity in this range bear information on the (nano)transport of charge carriers for the three following reasons:

1. the plasma frequency of electrons in semiconductors usually lies near the THz range (e.g. the plasma frequency is 11 THz for electrons at a density of 10^{16} cm^{-3} in silicon);
2. scattering of charge carriers on defects in bulk semiconductors occurs usually on the femto- to picosecond time scale, producing a substantial dispersion directly in the THz range;
3. a charge carrier diffuses a few tens or hundreds of nanometers within the period of a THz pulse (the electron diffusion length $l_{\text{diff}} = \sqrt{D/\nu}$ is $\leq 60 \text{ nm}$ in silicon with the diffusion coefficient $D_e \leq 36 \text{ cm}^2\text{s}^{-1}$ [6] at a frequency $\nu = 1 \text{ THz}$). If there are any conduction barriers with a comparable spacing, such as boundaries of nanoparticles, the interaction of the carriers with them provides spectral features in the THz part of the optical conductivity spectrum of the sample.

The THz spectroscopy is often combined with a synchronized photoexcitation of the sample – in this case, we speak about Time-resolved THz spectroscopy or Optical pump–THz probe (OPTP) spectroscopy. The technique is able to characterize the dynamics of the charge transport from the moment of carrier photoexcitation to its trapping or recombination with sub-picosecond time resolution. The OPTP spectroscopy has at least four experimental degrees of freedom: varying energy and density of excitation photons, time after photoexcitation and sample temperature. Taking advantage of experiments where these quantities are varied, it is possible to characterize the ultrafast microscopic charge transport in nanostructured and disordered semiconductors with a large detail and a deep understanding.

1.3. Effective response challenge

The wavelengths of THz radiation are up to 5 orders larger than the size of the photoconductive nanoelements (nano-crystals, -clusters, -islands, -wires, etc.) that constitute discussed materials. The probing THz beam thus cannot be focused on a single nanoparticle (NP) but it probes an average response of all carriers in a macroscopic piece of the inhomogeneous sample*. A semiconducting nanoparticle containing photoexcited electrons and holes behaves like a polarizable object in the electric field of the probing THz radiation and the spaces between adjacent conducting NPs have finite capacitances. The so called *depolarization fields*, related to these effects, locally alter the field of the probing radiation and cause that the measured macroscopic absorption and dispersion of the THz radiation is related to the actual microscopic conductivity of the charge carriers in a non-linear manner.

This relation between the macroscopic response of the inhomogeneously conductive sample to external electric fields and the microscopic conductivities of its constituents has been described by various effective medium theories (EMT). The most often used approximate EMTs of Maxwell Garnett or Bruggeman sometimes fail when the sample morphology is near to percolation. The most general Bergman EMT is, on the other hand, quite complicated and mostly lacks sufficiently precise input information on the morphology of the system. In this thesis we present an effective medium model (called VBD model), developed recently in our group and, largely, within the framework of the thesis. It is able to describe the measurable photoconductivity in materials that contain semiconducting NPs in the form of *both* non-percolated inclusions *and* complex percolation pathways at the same time and which uses only on 3 independent parameters describing the sample morphology.

1.4. Structure of the thesis

The research in the THz spectral range is relatively young and has brought about its own terminology, methodology, inventions and problems. For this reason, Chapter 2 introduces the THz spectral range with its peculiarities in a wider context and our technique and experimental setup in particular. In Chapter 3, we give an overview of theoretical models of THz photoconductivity that have been used in the literature and of experimental works published in the area of THz spectroscopy of photoconductive nanomaterials.

The subsequent chapters present the original theoretical and experimental results of this thesis, starting with the presentation of the VBD effective medium approach and its comparison to other EMTs in Chapter 4. We also illustrate this model on an equivalent electric circuit analogy. In Chapter 5, we derive the general

* The size of the THz beam focus in a far field experiment is comparable to its wavelength, i.e. several millimeters. Near-field THz microscopy, which is not discussed here, reaches resolution of 3 μm using sub-wavelength apertures [7], or tens of nm using THz scattering on vibrating AFM tips [8].

solution of the wave equation describing the differential (transient) THz field build-up and propagation in an inhomogeneous photoexcited sample; we discuss solutions related to the proposed EMT model in particular. We apply this theory to the experimental spectra of THz photoconductivity of two systems of silicon nanocrystals (Si-NCs): derived from bulk crystalline Si by electrochemical etching in Chapter 6 and grown by crystallization in epitaxial $\text{SiO}_x/\text{SiO}_2$ ($x \leq 1$) multilayers in Chapter 7.

In Chapter 8, we study the charge carrier transport in bulk rutile TiO_2 at high photocarrier densities with the aim to obtain reference bulk data for TiO_2 -based nanosystems. Despite the relatively wide usage of this material, the understanding of charge transport in TiO_2 is still limited due to the strong electron-phonon interaction in it and we present qualitatively new findings thanks to utilizing the ps time resolution of OPTP spectroscopy.

Besides analytical models of (microscopic) carrier conductivity, our group carries out semi-classical Monte Carlo calculations of carrier motion in nanosystems. In Chapter 9, we analyze the relation of probabilistic parameters of a model system (probability of inter-NP transport) to its morphologic properties (spatial layout and touching areas of adjacent nanoparticles).

Finally, we sum up the conclusion of the thesis in Chapter 10. Chapters 11 and 12 contain the bibliographic references and the list of tables, respectively. Chapter 13 provides a *List of symbols and abbreviations* used throughout the thesis for the convenience of the reader.

2. THz spectroscopy

The research in the THz spectral range is quite peculiar and we find it suitable to provide first a short overview of the field, its current technologies and areas of interest. Then we describe techniques relevant for this thesis in detail. For further information we refer to the review of Peter Uhd Jepsen, David G. Cooke and Martin Koch [9].

2.1. Terahertz spectral range

The terahertz region appeared as a new spectral range overlapping partly with optics and electronics in the last two decades – it includes the longest far infrared (FIR) and the shortest microwave waves (see Table 2.1). THz radiation is also known as the “millimeter waves”, according to its wavelength, or the “T-rays”, in an analogy to the X-rays. In the 20th century, the research in this area somewhat lagged behind the adjacent parts of the electromagnetic spectrum because of a lack of efficient sources and detectors. THz frequencies are too high for electronic circuits and transistors [10] and coherent THz emission in the active medium of a FIR laser is highly inefficient [11]. Incoherent low-intensity THz radiation is found in the nature as a part of the thermal radiation of every black-body at temperatures above a few Kelvins*. This fact finds its use in astronomy in chemical analysis of the emission spectra of cold interstellar dust and distant starburst galaxies. [12] Yet, it is absorbed by water vapor in the atmosphere and submillimeter telescopes must be located at very dry and high altitude places, such as the Atacama Desert, or in the free space. As the ranges of laboratory sources of optical and electronic radiation did not overlap for a certain time, the THz part of the electromagnetic spectrum was called the “Terahertz gap”. [13]

	Frequency	Wavelength	Wavenumber	Energy	
	15 THz	15 μm	667 cm^{-1}	83 meV	
	3 THz	100 μm	100 cm^{-1}	12 meV	FIR range [14]
THz range	0.3 THz	1 mm	10 cm^{-1}	1.2 meV	
	0.3 THz	1 mm	10 cm^{-1}	1.2 meV	
	0.1 THz	3 mm	3.3 cm^{-1}	0.41 meV	microwave range [15,16]
	0.3 GHz	1 m	0.01 cm^{-1}	1.2 μeV	

Table 2.1 Borders of THz frequency range overlapping with common optical and electronic ranges of electromagnetic radiation.

Bridging of the “gap” was started in 1985 when Auston and Cheung [17] generated broadband THz pulses via *optical rectification* (OR) of ultrashort laser pulses in a non-linear electro-optic crystal and detected them by *time-domain*

* The maximum of spectral radiance lies at 1 THz for a black body at a temperature of 18 K.

spectroscopy (TDS). Principles of OR and TDS are described in the following sections in detail because they are used throughout the experimental part of this thesis. Since 1985, detection in the time-domain has remained the most frequent method used for spectroscopic measurements in THz laboratories worldwide, while various phenomena other than OR have been employed to generate pulsed broadband and also continuous-wave (cw) THz radiation. *Photoconductive switches*, for example, utilize ultrashort optical laser pulses, similar to OR, and provide THz pulses with similar bandwidths and somewhat lower intensities – these two generation techniques are most widely used in tabletop THz spectroscopic setups nowadays.

Other THz sources and detectors

In 2002, Hebling et al. [18] proposed the *tilted-wave-front* scheme of optical rectification in order to achieve phase matching between a THz and an optical pulse in highly nonlinear materials, such as LiNbO₃. This allows one to generate THz pulses with the peak field of ~ 1 MV/cm*. [19] “*THz wave air photonics*” techniques are used to both generate and detect THz pulses with bandwidths exceeding 30 THz in laser-induced air plasma [20,21].

Quantum cascade lasers (QCL) present the youngest and quite promising technology for emitting narrowband THz radiation. They achieve stimulated emission of FIR radiation on intersubband transitions in quantum wells of a semiconductor superlattice. A QCL is in principle single-component chip that needs only a power supply and can be either used as external emitter or as an integrated element in optoelectronic circuits. Its main drawback is that it requires cryogenic cooling in the few-THz range. QCLs are somewhat tunable and one can already buy a commercial frequency-domain spectroscopic setup with a set of QCL chips covering several adjacent intervals in the THz spectral range.

Photomixing of two coherent laser beams with similar frequencies in a non-linear crystal also yields coherent narrowband pulsed or cw THz radiation and a similar technique can also be used to detect monochromatic THz beams coherently. [9]

Sources based on a beam of free electrons include *backward-wave oscillators*, *synchrotrons*, *free electron lasers* and *gyrotrons*. The first ones use radiation from non-relativistic electrons and can fit into table-top experiments. The others are large-scale facilities that provide tunable pulsed or continuous-wave THz radiation of extraordinary intensities from beams of relativistic electrons.

Novel broadband sources radiating from about one THz to tens of THz are referred to as “*multi-terahertz*” because their principle and functionality are derived from the standard time domain THz spectroscopic techniques. However, by their spectral content, they technically belong to FIR (or even mid-IR) broadband sources.

* classic collinear setups reach peak field of several kV/cm.

Incoherent THz spectroscopy in the frequency domain (e.g. in an Fourier-transform infrared spectrometer) is feasible with thermal sensors such as pyrometers, bolometers or Golay cell detectors. [22] Thermal detectors naturally suffer from relatively long response times and the presence of background thermal radiation. Their sensitivities are generally lower (with the exception of hot-electron bolometers) than that of electro-optic detectors used in TDS. For these reasons, they are used rather in high-intensity or narrow-band experiments or in THz imaging applications.

THz science, technology and applications

The scientific areas of interest, besides charge carrier transport, cover: vibrational modes of molecular crystals, crystals of organic molecules in particular; relaxation processes of permanent or collision-induced dipoles in liquids, particularly in water; [9] strongly correlated electronic systems [23] and phase transitions in multiferroics [24].

THz technologies naturally require means for spectral manipulation of THz beams. This can be done e.g. by using tunable *photonic crystals* or tunable *metamaterials*. It is also possible to achieve on-demand THz properties in THz metamaterials such as *negative refractive index* in a narrow band. [25–27]

Recently, the THz imaging and spectroscopic systems have matured enough to reach first commercial applications. In the field of quality control and safety, THz imaging is a complement to usual rays such as visible light or X-rays. THz waves can penetrate common non-metallic packaging materials that are opaque in the visible range – such as paper, wood, certain plastics or dry fabric – and provide contrast and spectral information on dielectric contents that are mostly without contrast for the X-rays (ceramics, plastics, liquids, narcotics or explosives [9]). THz photons do not ionize the matter and thus are also viable for inspection of living persons (the THz rays can “see” contraband or weapons concealed under the clothing) or susceptible materials. In the field of quality control, THz imaging can locate voids or moisture and other inhomogeneities in dried food [28], molded plastics [29], or composite materials or determine the thicknesses of multi-layered paints and coatings. THz cameras usually contain an 2D array of microbolometers or photoconductive antennas in the focal plane of a silicon lens. These cameras are rapidly approaching real-time applications as they currently reach resolution of hundreds × hundreds of pixels and rates of several frames per second. [30]

As THz waves are strongly absorbed by water, they do not penetrate deep into the skin of living beings and attempts have been made to utilize THz in diagnostics of skin cancer. [31]

THz rays are also utilized in cultural heritage preservation – for non-destructive characterization of the layers of frescoes, plasters, paintings and other opaque artworks. The detailed knowledge on the layers then enables performing of the most appropriate restoring and preserving actions. [32]

For further details and references on THz technology and materials let us refer the reader to the review papers of Tonouchi [33] or Ferguson and Zhang [34].

2.2. Time-domain spectroscopy

The electric field of THz radiation evolves relatively slowly in time (\sim ps) compared to the pulse length of available femtosecond laser sources. An E -field detector, e.g. an electro-optic sensor, gated with fs laser pulses can thus measure the *instantaneous* electric field of a THz wave. [35,36] Changing the time delay t between the THz pulse and the time synchronized laser gating pulse allows one to sample the whole waveform of the electric field $E_t(t)$ of the THz pulse transmitted through a sample. Through Fourier transform one obtains the *complex* spectrum $E_t(\omega)^*$ of the THz pulse (Fig. 2.1).

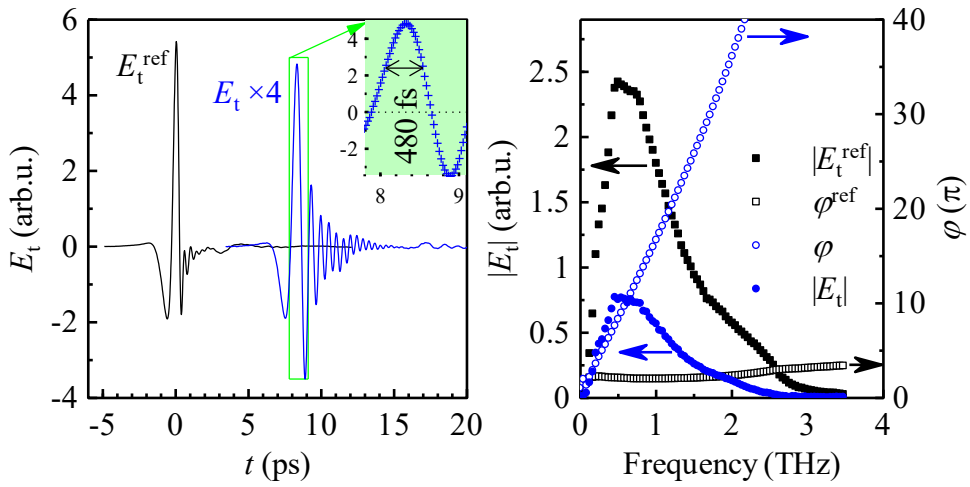


Fig. 2.1 *Left*: Waveforms E_t^{ref} and E_t of a THz pulse transmitted through the setup without sample and through a 0.26 mm thick TiO_2 sample at 70 K, respectively. (*Inset*: sampling points in a section of E_t) *Right*: their complex spectra $E_t = |E_t|e^{i\varphi}$ (same scale as the left plot).

To obtain the THz response function of a sample, one usually places it in the focus or in a collimated section of the pulsed THz beam and measures separately the waveforms of:

1. the “signal” THz pulse $E_t(t)$ transmitted through the sample;
2. the “reference” THz pulse $E_t^{\text{ref}}(t)$ transmitted either through a reference sample or measured without the sample in the beam path.

* We do not introduce any special notation for complex-valued variables; all frequency-resolved quantities in the thesis are complex. Real and imaginary components are denoted as: $X = X' + iX''$. The sign convention $E(t) = E_\omega e^{-i\omega t}$ is used for a monochromatic wave. Angular frequency $\omega = 2\pi\nu$ is used in equations; all spectra are plotted against linear frequency ν .

Both measured waveforms are temporal convolutions of the waveform radiated from the emitter with the transmission coefficient of the sample/reference and an instrumental function which describes propagation of the pulse through the setup and its detection in the sensor. Upon Fourier transform into the frequency domain, the convolutions of temporal functions become products of the respective spectral functions. In the ratio $E_t(\omega)/E_t^{\text{ref}}(\omega)$, the instrumental functions cancel out exactly and one obtains the ratio of the complex transmission coefficient of the sample $t_{\text{sample}}(\omega)$ and of the reference $t_{\text{ref}}(\omega)$. [37] This ratio defines the complex THz transmittance of the sample:

$$T(\omega) = \frac{t_{\text{sample}}(\omega)}{t_{\text{ref}}(\omega)} = \frac{E_t(\omega)}{E_t^{\text{ref}}(\omega)}. \quad (2.1)$$

In the case when the sample is removed from the setup for the reference measurement, we get $t_{\text{ref}} = \exp(i\omega L/c)$, where L is the sample thickness and c is the speed of light in vacuum. The measured complex transmittance $T(\omega)$ of the sample is related to its complex refractive index n . For a homogeneous sample, the relation reads [38]

$$T(\omega) = \frac{4n \exp[i\omega(n-1)L/c]}{(n+1)^2} \sum_{k=0}^m \left[\left(\frac{n-1}{n+1} \right) \exp(i\omega n L/c) \right]^{2k}. \quad (2.2)$$

The sum in (2.2) accounts for the first m Fabry-Perot reflections of the THz pulse in the sample. For thick samples, these reflections form separate echoes of the main pulse in the time domain and can be time-windowed. [39] Then, m is trivially the number of echoes taken into account.

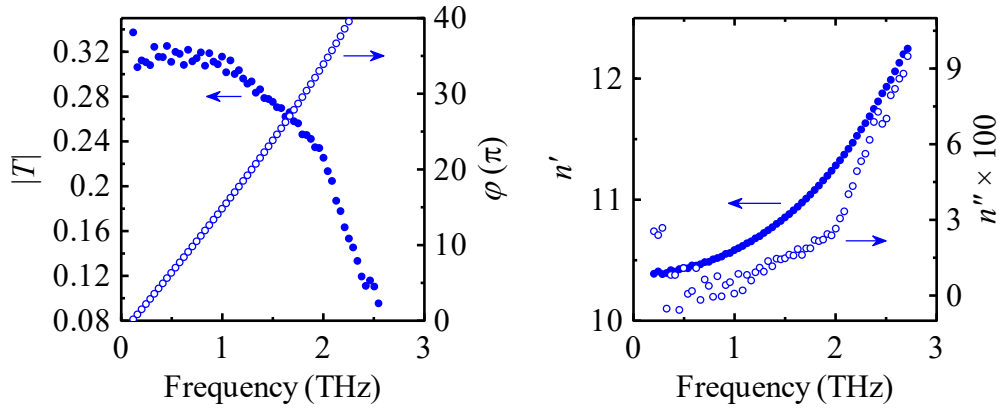


Fig. 2.2 *Left*: THz transmittance of a 0.26 mm thick TiO_2 slab at 70 K and *right*: its refractive index.

For thin samples, the series should be summed up to the infinity, as the echoes overlap in the time domain. [38] The numerical solution of (2.2) is simpler and less sensitive to errors in measurements when separate echoes can be windowed. [40] With THz-opaque samples it is also possible to carry out experiments in reflection

geometry. [41] Fig. 2.2 shows the complex transmittance and refractive index calculated from the data presented in Fig. 2.1.

In this work, THz time-domain spectroscopy without photoexcitation of the sample is used as an auxiliary method for determining the refractive index of a thick sample of bulk rutile in the THz frequency range in Chapter 8. The next section introduces the Optical pump–THz probe technique which is the principal method used in this thesis.

2.3. Optical pump–THz probe spectroscopy

Optical pump–THz probe spectroscopy measures the transient change $\Delta E_t(t)$ of the THz waveform transmitted through the sample upon collinear photoexcitation. Plane-parallel samples are placed perpendicular to the direction of propagation z of the THz pulse; the wavefronts of the THz radiation are planar throughout the thickness of the sample. The formation and propagation of the transient part ΔE of the THz field *inside* the sample is then described by a one-dimensional wave equation [42]

$$\frac{d^2 \Delta E(\omega, z)}{dz^2} + n(\omega)^2 k_0^2 \Delta E(\omega, z) = U(\omega, z), \quad (2.3)$$

where n is the refractive index of the sample in the ground state* and $k_0 = \omega/c$ is the angular wavenumber of the THz wave in vacuum. The right-hand-side function $U(\omega, z)$ describes the source of the transient part of the THz field. In terms of the transient conductivity $\Delta\sigma(\omega, z)$ that arises in the sample after photoexcitation, it reads [42]:

$$U(\omega, z) = -ik_0 Z_0 \Delta\sigma(\omega, z) E(\omega, z), \quad (2.4)$$

where E is the *total* THz field (probe + transient) at a given depth and Z_0 is the vacuum wave impedance. The transient conductivity is generally a function of the depth due to the Lambert-Beer exponential absorption law for the optical excitation beam. Solution of the wave equation with the suitable source function and proper boundary conditions yields the transient part ΔE_t of the electric field transmitted through the sample. Solutions concerning nanomaterials and cases important for this thesis are derived in Chapter 5. In this Section, we demonstrate the solution of (2.3) on a simple pedagogic case.

Equations (2.3) and (2.4) are valid in the *quasi steady-state approximation*, i.e. when the transient conductivity $\Delta\sigma$ does not change substantially during the few-ps duration of the probe pulse. Many transport processes are slow enough not to spoil the approximation, e.g. the carrier recombination causes a decay of $\Delta\sigma$ on a time scale of hundreds of ps to ns. On the other hand, the carrier generation,

* Usage of equilibrium refractive index without its excitation-induced transient contribution is justified in a more technical discussion in the beginning of Chapter 5.

thermalization and other ultrafast processes may take place within a picosecond after photoexcitation. The measurement of a single probe waveform is meaningless in such time intervals: each point in the few-ps-lasting THz waveform would have interacted with the sample in a different conductivity state. In order to assess the transient conductivity during such fast processes, one must follow a more elaborate measuring procedure which is not the subject of this thesis. Briefly speaking, the transient THz field must be experimentally sampled in a 2D grid of the probe–sampling and pump–probe delays t and t_p , respectively. A two-dimensional Fourier transform $\Delta E_t(t, t_p) \rightarrow \Delta E_t(\omega, \omega_p)$ must then be performed and equations must take into account a mixing of both frequencies ω and ω_p *. [43] All experimental THz photoconductivity spectra in this thesis comply with the requirement of the quasi steady-state approximation.

Having measured the transient part $\Delta E_t(t)$ of the transmitted waveform, one uses the waveform of the THz pulse transmitted through the unexcited sample $E_t(t)$ as the reference. In the frequency space, the transient complex transmittance spectrum $\Delta T(\omega)$ of the photogenerated excitations is obtained (see Fig. 2.3):

$$\Delta T(\omega) = \frac{\Delta t_{\text{sample}}(\omega)}{t_{\text{sample}}(\omega)} = \frac{\Delta E_t(\omega)}{E_t(\omega)}. \quad (2.5)$$

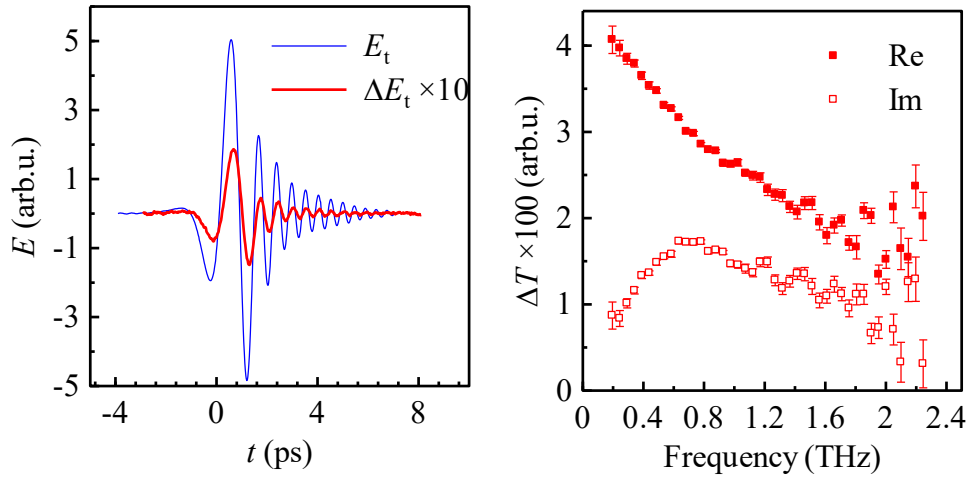


Fig. 2.3 *Left:* Waveforms E_t and ΔE_t of the probe pulse transmitted through a 0.26 mm thick rutile slab at 70 K in equilibrium and 11 ps after excitation with 1.6×10^{14} photons/cm² at 266 nm, respectively. *Right:* Transient transmittance of the excitations (the scale is in relation with the left plot).

In a homogeneous sample with a thin photoexcited layer, the experimental transient transmittance spectrum is directly defined by the transient change of the conductivity spectrum of the sample [42]:

* ω_p is used for the Fourier counterpart of pump–probe delay t_p solely in this place. It is not to be confused here with the plasma frequency that is defined in Section 3.3 and used thereafter.

$$\Delta T(\omega) = -\frac{\Delta\sigma(\omega)}{\alpha} \frac{Z_0}{n_1 + n_2}, \quad (2.6)$$

where α is the sample absorption coefficient for the pump light and n_1, n_2 stand for the THz refractive indices of the media in front and behind the photoexcited layer, respectively (vacuum, substrate, cuvette faces, unexcited part of the sample etc.).

The transient transmittance includes response from all polar excitations that are active in the THz range such as band carriers, polarons, excitons, optical phonons etc. This thesis deals with the ultrafast transport of mobile carriers; for this purpose, pumping with over-the-band-gap photons is used to generate charge carriers in the conduction and valence band of the sample.

In the simplest theoretical case of a thin homogeneous sample with a single (or one dominant) type of photocarriers, the overall transient conductivity is proportional to the mobility $\mu(\omega)$ of the single charge carrier:

$$\Delta\sigma(\omega) = eN_0\mu(\omega), \quad (2.7)$$

where e is the elementary charge. The density N_0 of photocarriers at the sample surface is given by

$$N_0 = \alpha\phi\xi, \quad (2.8)$$

where ξ is the quantum yield of photogeneration and ϕ is the pump photon fluence in a single excitation pulse (in photons/cm², also referred to as the excitation fluence here). While α is usually taken from the literature or measured independently and ϕ is determined experimentally, the quantum yield is mostly a priori unknown and in some cases it may substantially differ from 100%. [44] For this reason, the quantum yield and the magnitude of the carrier mobility mostly cannot be distinguished from each other in the transient conductivity (2.7) and only the yield-mobility product can be calculated from the measured transient transmittance. Equations (2.5)–(2.8) together show that in the case of a thin homogeneous sample with one dominant type of photocarriers, an OPTP measurement yields straightforwardly the complex mobility spectrum of the charge carriers (multiplied by the quantum yield which is the only unknown parameter to be discussed):

$$\xi \cdot \mu(\omega) = -\frac{1}{e\phi} \frac{n_1 + n_2}{Z_0} \frac{\Delta E_t(\omega)}{E_t(\omega)}. \quad (2.9)$$

Because of the clear physical meaning of the equation above for homogeneous semiconductors, we use its right-hand side to define the *normalized* transient transmittance spectrum

$$\Delta T_{\text{norm}}(\omega) = -\frac{1}{e\phi} \frac{n_1 + n_2}{Z_0} \frac{\Delta E_t(\omega)}{E_t(\omega)} \quad (2.10)$$

and consider it as a suitable normalized experimental output quantity of Optical pump–THz probe experiments. [45] Also in samples with a more complicated response (with several types of photoconductive excitations and with a complicated

morphology) ΔT_{norm} holds the meaning of the average photoconductive response of the sample per single absorbed pump photon and per elementary charge and it is expressed in units of the mobility. This quantity becomes especially useful for experiments in inhomogeneous samples.

The equations above were derived for a general pump–probe delay t_p within the steady-state approximation. By changing t_p , OPTP spectroscopy can measure the carrier THz photoconductivity spectrum at different stages of the generation–transport–trapping/recombination process. With picosecond THz probe pulses, it provides resolution which cannot be achieved with other conductivity measuring techniques.

By changing the pump photon fluence ϕ , one can generate carriers in a sample at a broad range of densities without the need of preparing sets of samples with different dopant concentrations. This enables characterization of the studied material in different conductivity states. Notably, our research (Chapter 4) shows that the response originating from conductively *percolated* semiconducting parts of a (nano)material sample scales *linearly* with the carrier density while the response of *non-percolated* parts of the sample depends *non-linearly* on the carrier density. This allows one to distinguish between samples containing percolated and non-percolated semiconductor particles and even discriminate and characterize separately the percolated and non-percolated semiconducting subsystems in a single structure, provided that the data are obtained over a broad range of excitation densities. [4,45]

2.3.1. Spectrally averaged transient THz kinetics

Besides measuring the complete waveforms $\Delta E_t(t)$ (and Fourier-transforming them to transient conductivity spectra) at selected times t_p after photoexcitation, one can carry out the following useful experiment. The probe–sampling delay t is set to correspond to the maximum of the transient signal ΔE_t waveform and a scan of the pump–probe delay t_p is performed (Fig. 2.4). In this way, a 1-dimensional scan of the transient THz dynamics is obtained. These scans provide *spectrally averaged* THz response to the photoexcitation, i. e. the time evolution of the transient absorption (photoconductivity) of the sample in the whole frequency range of the given experimental setup. The highest resolution is here given by the timewidth of the main peak of the THz electric field which is usually a few hundreds of femtoseconds (cf. inset in Fig. 2.1).

One cannot directly determine whether the evolution of the measured dynamics is caused by changes of carrier concentration or of their mobility. Different processes are usually attributed to the observed kinetics according to their characteristic time constants and according to the observed changes of transient THz conductivity spectra measured at selected pump–probe delays. The kinetics may display for example ultrafast cooling of hot electrons [47], photocarrier injection and electron–hole separation [48] or expansion of a dense electron plasma (Section 8.1) in the first units or tens of ps, and usually the decay of mobile carriers through their

recombination or trapping on longer time scales (see Fig. 2.4, discussed in Section 7.4).

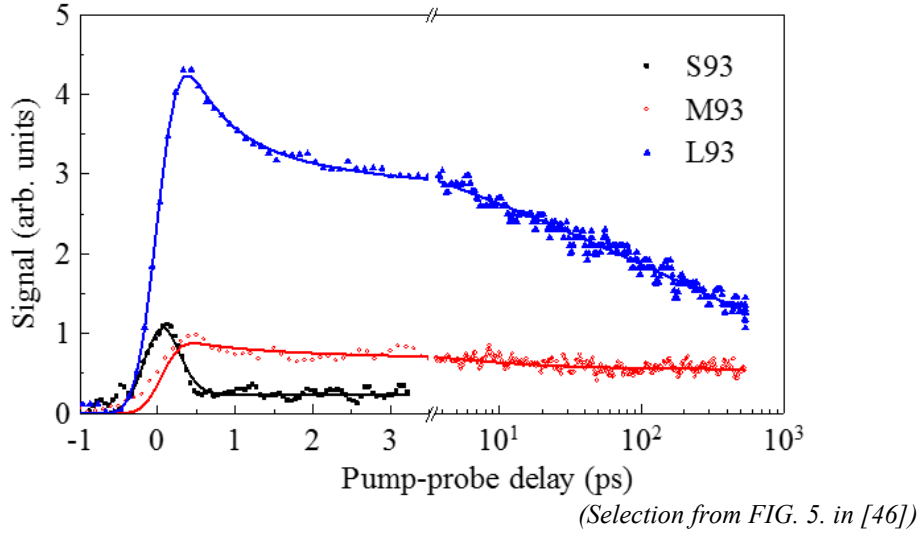


Fig. 2.4 Example of transient THz kinetics measured by pump–probe scan on superlattices of Si nanocrystals in SiO₂ matrix. Legend refers to different nanocrystal sizes; lines serve as guides to the eye.

2.4. Experimental setup

In this chapter the experimental methods used throughout this thesis are introduced from the practical point of view. We stress experimental characteristics and limitations. All OPTP experiments in this thesis were performed by using the output train of pulses of a regenerative Ti:sapphire amplifier (Spitfire ACE, Spectra-Physics/Newport) with 1 mJ pulse energy, 35–50 fs pulse length, repetition rate 5 kHz and central wavelength $\lambda = 800$ nm. The linearly polarized laser beam was split into three beams by 800 nm beam splitters as indicated in Fig. 2.5: the probe, the sampling and the pump beam.

Each optical *probe* beam pulse generates a THz pulse via optical rectification (described later) in a 1 mm thick (110)-ZnTe crystal (the *emitter*). The emitted divergent THz beam is collected and focused with an ellipsoidal aluminum mirror that has its foci at the output face of the emitter and at the aperture of the sample holder. After transmission through the sample plane, the probe THz pulse is focused with a second ellipsoidal mirror through a THz-transparent pellicle beam splitter onto the front face of another 1 mm thick (110)-ZnTe crystal (the *sensor*).

The optical *sampling* beam pulses undergo adjustment of intensity and polarization and are introduced perpendicular to the pellicle beam splitter which reflects them collinearly with the THz beam onto the sensor. The instantaneous electric field of the THz pulse induces birefringence in the sensor crystal through the linear electro-optic effect (the Pockels effect) and the polarization state of the simultaneously passing sampling pulse is thus changed.

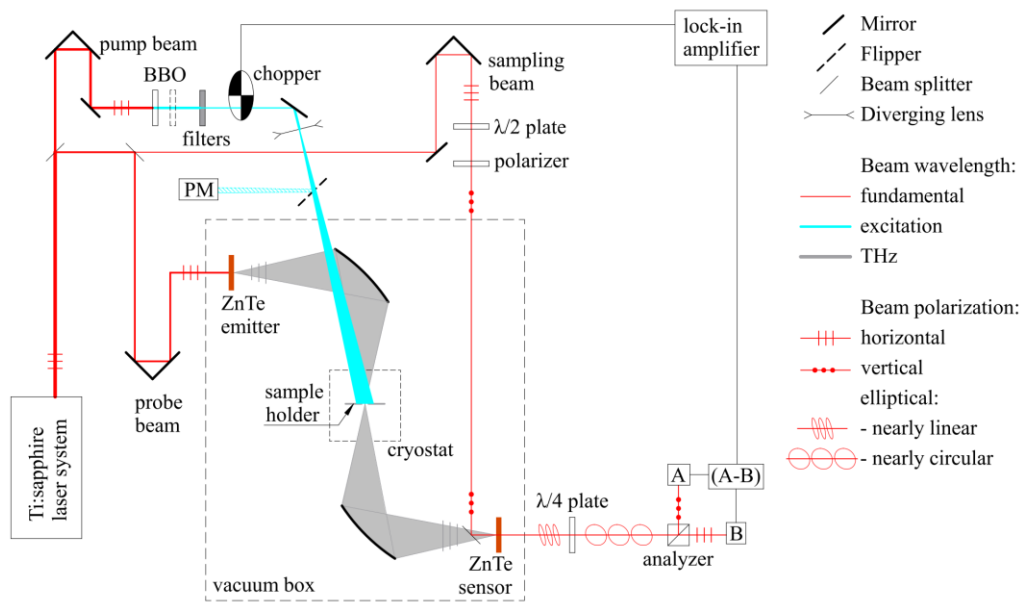


Fig. 2.5 Diagram of experimental setup. Thickness of red (fundamental) laser beam lines indicates qualitatively the power of individual beams.

The polarization of the sampling pulse is then converted into nearly circular with a quarter-wave plate (a Babinet-Soleil compensator is used and fine tuned before each experimental session to act as the $\lambda/4$ plate in actual laboratory conditions). The general elliptical polarization of the sampling pulse is subsequently resolved into its two orthogonal linearly polarized components by using a Wollaston prism (the analyzer in the diagram). The intensities of these two components are measured with two antiparallel silicon photodiodes A and B. The difference signal ($A - B$) from the photodiodes is linearly proportional to the instantaneous THz field in the sensor. Phase-sensitive detection synchronized with the chopping frequency of the pump beam detects the transient change $\Delta E_t(t)$ as the difference between the signal with the pump-beam on and off.

To avoid absorption of THz radiation on water vapor, the THz part of the experiment is enclosed in a custom-made aluminum box with optical windows that is evacuated with a primary vacuum pump to a pressure of less than 1 mbar during the measurement. The sample is placed onto the front face of a planar metal holder with a circular aperture either directly inside the box or within a continuous-flow optical cryostat (Oxford Optistat) that has a pair of sapphire input windows and a pair of Mylar output windows. The delay between pulses in individual beams is controlled with delay lines with a resolution of 3 fs.

The *pump* beam photons are either used to excite charge carriers in the sample directly at their fundamental frequency or they are converted to a higher energy that exceeds the band gap of the sample. Most often a (110)-oriented BBO crystal is used for second harmonic generation, occasionally followed with another (110)-oriented BBO crystal to generate the third harmonic frequency (via sum frequency generation from the second harmonic beam and the collinearly passing

idle remainder of the fundamental beam). An optical parametric amplifier system TOPAS is alternatively used to convert the pump beam to other photon energies if needed.

At any excitation wavelength, the pump beam is defocused with a CaF₂ plano-concave lens so that a relatively homogeneous excitation density is achieved across the measured area of the sample. (The lens is placed in such distance from the sample holder that less than 1/3 of the power of the incident pump beam passes through the holder aperture. The excitation density at the edge of the aperture is at least 67% of that in its center with such setting.) The angle of incidence of the pump beam on the sample is about 10° which means that it takes 1.8 ps to excite the 3 mm width of the measured area of the sample.

The power of the pump beam is controlled by using neutral density filters or a variable polarizing attenuator and measured with a power meter. The power meter (PM in Fig. 2.5) is placed in an accessible section of the pump beam between the attenuator and the vacuum box as it cannot be placed in the position of the sample inside the evacuated vacuum box (or inside a chilled cryostat) after each change of attenuation. The fraction K_{box} of the pump power measured before the box (P_{meas}) that transmits through the aperture of an empty sample holder is measured before each experimental session with unevacuated box. The power incident on the probed area of the sample is then calculated as $P_{\text{inc}} = K_{\text{box}} \cdot P_{\text{meas}}$ during the experiment whenever the attenuation is changed. Two thin sapphire plates are placed in front of the sample holder to mimic reflection of the pump beam on cryostat input windows when determining K_{box} for measurements at low temperatures as the used power meters cannot fit into the cryostat chamber. P_{meas} is either measured with a thermopile detector (PowerMax PM3 from Coherent) that is placed manually directly into the pump beam path (for powers $P_{\text{meas}} \geq 20$ mW); or the pump beam is deflected by a flipper mirror into a silicon photodiode power meter (Coherent LM-2 VIS for $1060 \text{ nm} \geq \lambda \geq 400 \text{ nm}$ and LM-2 UV for $400 \text{ nm} \geq \lambda \geq 250 \text{ nm}$; for powers $P_{\text{meas}} \leq 25$ mW). The photon fluence incident on the sample front surface is calculated as

$$\phi_{\text{inc}} = \frac{P_{\text{inc}}}{\frac{hc}{\lambda} f_{\text{rep}} \pi r^2} \quad (2.11)$$

where h is the Planck constant, f_{rep} is the repetition rate of the source laser and r is the radius of the sample holder aperture ($r = 1.5$ mm throughout this thesis). The reflectivity R of the sample front face (and possibly of a cuvette front face) for the pump light is found in the literature or measured and the excitation fluence is $\phi = (1 - R)\phi_{\text{inc}}$. When measuring the reference field waveform E transmitted through the sample in the ground state, the pump beam is blocked and the chopper is placed in the path of the probe beam. Table 2.2 sums up the characteristics of our setup.

	Feature	Value/Range	Note
Detection	dynamic range (typical)	8×10^{-5} amplitude ~ 82 dB power	200 accumulations
	dynamic range (best achieved)	7.5×10^{-6} amplitude ~ 100 dB power	6000 accumulations (16 hours)
	spectral range (82 dB)	0.2 – 2.3 THz	
	spectral range (100 dB)	0.4 – 1.4 THz	
	spectral resolution	0.1 THz	typically (with $\lesssim 10$ ps waveform scan)
Excitation	pump–probe scan range	660 ps	
	pump–probe scan resolution	0.2 ps	
	max. $\phi_{\text{inc}}(\lambda = 800 \text{ nm})$	1×10^{16} ph/cm ²	} homogeneous over 3 mm diameter *
	max. $\phi_{\text{inc}}(\lambda = 400 \text{ nm})$	2×10^{15} ph/cm ²	
max. $\phi_{\text{inc}}(\lambda = 266 \text{ nm})$	4×10^{14} ph/cm ²		
Conditions	temperature range	6 – 900 K	cryostat/furnace
	peak THz field	~5 kV/cm	without cryostat

*The excitation density at the edge of the aperture is at least 67% of that in its center.

Table 2.2 Characteristics of the OPTP experimental setup. *

Optical rectification

One of the most common processes for table-top generation of broadband THz pulses is optical rectification of ultrashort optical pulses inside a second-order non-linear crystal. It is a process somewhat similar to difference frequency generation but it takes place among the photons of a single laser pulse. The electric field of the laser pulse drives oscillations of bound charges (ions) in the crystal lattice around certain average positions. These oscillations are natural also in linear optics — their interaction with light is expressed by the complex values of first-order susceptibility or refractive index of the material (blue in Fig. 2.6). However, in non-linear crystals, the average positions of the oscillating ions differ from their equilibrium positions due to the asymmetry of lattice forces; the higher is the intensity of the driving field, the further are the new average positions of the ions from their equilibrium locations.

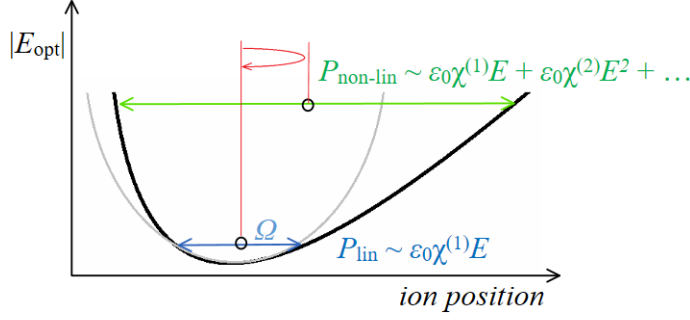


Fig. 2.6 Schematics of ion oscillations in an asymmetric potential (black line) in an optical electric field. *Gray*: parabolic approximation at the bottom of the potential, *blue*: linear oscillation, *green*: non-linear oscillation, *red*: rectified low-frequency component of non-linear polarization.

This shift of *average* positions of bound charges (red in Fig. 2.6) constitutes a net polarization in the crystal which is proportional to the intensity of the field that is necessarily rectified (unipolar, non-alternating). This is because the asymmetrical lattice forces allow shifts of the average positions of the oscillating ions only in specific lattice directions and back to the equilibrium. Considering illumination by an ultrashort optical pulse, the unipolar (rectified) polarization current pulse becomes a source of a low-frequency field proportional to its time derivative. Quantitatively, the non-linear polarization P of the medium with second-order susceptibility tensor $\chi^{(2)}$ at a general frequency ω is equal to:

$$P_i(\omega) = \varepsilon_0 \int_{\Omega_0 - \Delta\Omega/2}^{\Omega_0 + \Delta\Omega/2} \chi_{ijk}^{(2)}(\omega, \Omega + \omega, -\Omega) E_j(\Omega + \omega) E_k^*(\Omega) d\Omega, \quad (2.12)$$

where ε_0 is the permittivity of vacuum, asterisk denotes complex conjugation, Ω_0 is the central frequency and $\Delta\Omega$ is the bandwidth of the laser pulse $E(\Omega)$. The spectrum of the emitted pulse and its temporal shape is determined by the bandwidth of the optical pulse. The phase matching condition is given by the equality of the refractive index of the emitted waves and the group refractive index n_{group} of the incident optical light:

$$n(\omega) = n(\Omega) + \Omega \frac{dn(\Omega)}{d\Omega} \equiv n_{\text{group}}(\Omega). \quad (2.13)$$

ZnTe crystals display good phase-matching and frequency-mixing properties for rectification of femtosecond optical pulses at 800 nm to THz frequencies and low absorption up to 3 THz. Fig. 2.7 shows the absorption coefficient and refractive index of ZnTe. Absorption (Fig. 2.7(a)) at high THz frequencies is dominated by the transverse optical phonon mode at 5.32 THz; at lower frequencies there occur two bands that were assigned by Gallot et al. [49] to transverse acoustic phonon at 1.6 THz and longitudinal acoustic phonon at 3.7 THz. The refractive index of ZnTe (Fig. 2.7(b)) is governed by the optical phonon in the THz range.

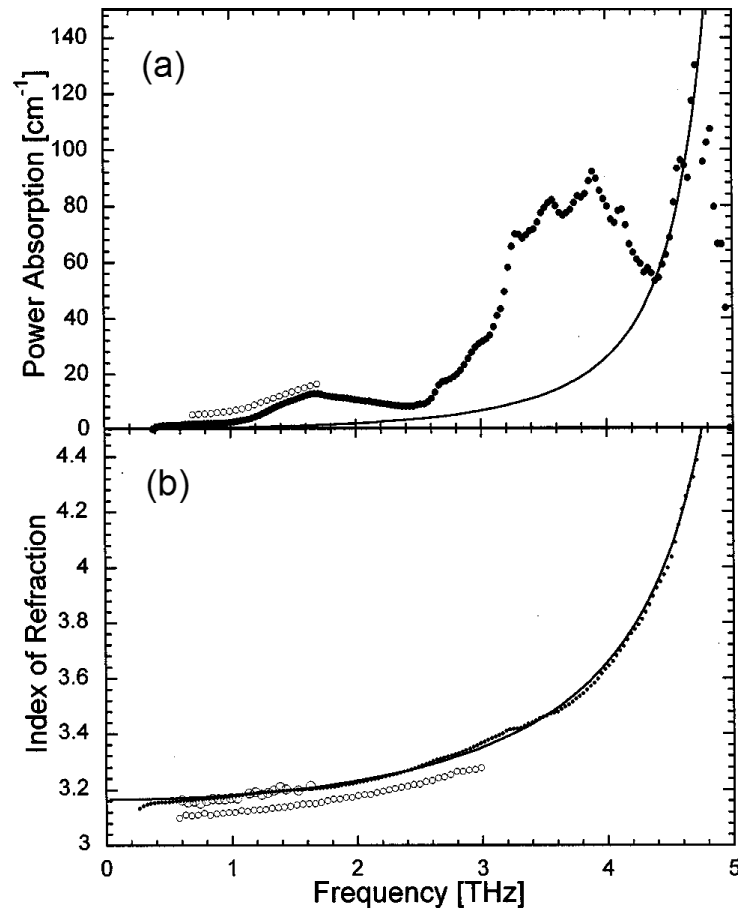


(FIG. 1(b,c) in [49])

Fig. 2.7 THz properties of (001)-ZnTe at room temperature (a) absorption coefficient and (b) refractive index. *Symbols*: experimental data, *line*: theoretical response of TO-phonon at 5.32 THz.

3. THz spectroscopy of nanomaterials in the literature

In the Introduction we pointed out that the THz spectral range is particularly sensitive to the properties of charge transport on the nanoscale. In this chapter we mention the approaches most frequently used to model and/or fit THz photoconductivity of nanostructured, disordered and bulk semiconductors. We emphasize the difference between the effects of *charge carrier localization** and *effective medium response* in semiconductor nanostructures. These two effects have similar impact on measured THz photoconductivity spectra and occur inseparably in semiconductor nanostructures containing non-percolated semiconducting nanoparticles (NPs) but have physically different origins. In the following sections, we remind the Drude model and Dyre's hopping models of the mobility, the Localized plasmon model of the conductivity, various Effective medium theories, Monte Carlo simulations of microscopic transport in the classical limit and the phenomenological Drude-Smith model. The Drude-Smith model deserves certain attention as it is relatively widely used in the area of THz photoconductivity but extensive discussions about its meaning have pointed out possible misconceptions in the physical interpretation of its parameters. In the end of this Chapter, previous important experimental works are reviewed.

Bulk vs. Nano

Published papers of THz laboratories worldwide confirm a distinct difference between the THz photoconductivity spectra of materials based on semiconducting nanoparticles (polycrystals, nanodots, nanotubes/wires, etc.) and those of bulk semiconductors. [50] Generally speaking, photocarriers in the *bulk* exhibit a real part of conductivity decreasing with frequency and a positive imaginary conductivity (Fig. 3.1(a)). In contrast, photocarriers in many *nanomaterials* show a THz response with the real part increasing with frequency and a negative imaginary part (Fig. 3.1(b)). In an analogy to electrical circuits, the bulk response represents a current that lags behind the applied electric field, i.e. the response of a non-polarizable material described by certain resistivity and a self-*inductance*. The negative imaginary conductivity in the response of nanomaterials is, in this sense, characteristic to a polarizable medium described by a certain *capacitance*. [50,51]

* also referred to as *charge carrier confinement* (in the *classical*, morphological meaning of confinement). Charge carriers in the regime of substantial *quantum* confinement were not detected by OPTP in this thesis, although it is possible.

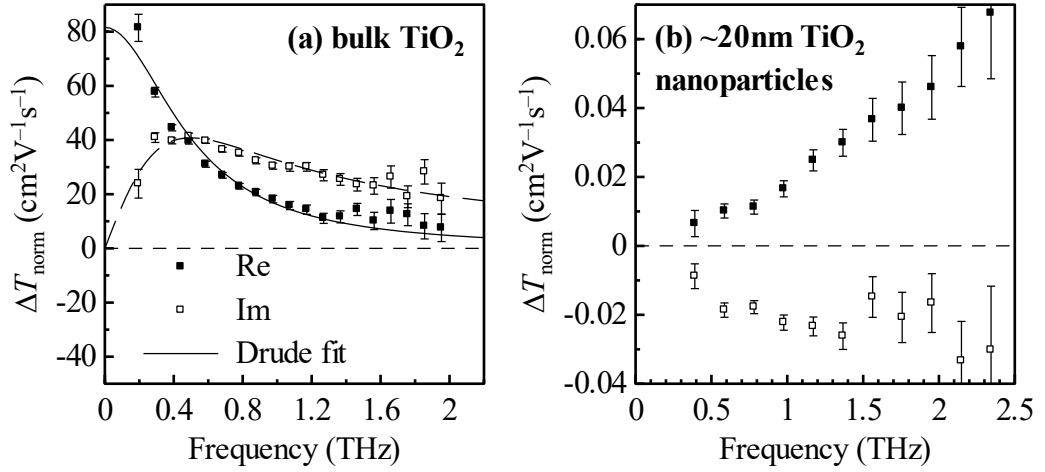


Fig. 3.1 *Symbols*: THz photoconductivity spectra of rutile excited at 266 nm: (a) bulk at 70 K, $\phi = 1.8 \times 10^{13}$ photons/cm², (b) ~20 nm TiO₂ nanocrystals $\phi = 3.3 \times 10^{14}$ photons/cm² at 300 K. *Lines*: Drude fit with $m^* = 6.9 m_e$, $\tau_S = 320$ fs;

3.1. Drude model

The inductive THz response of mobile charge carriers to weak probing fields (below a few tens of kVcm⁻¹) in bulk materials is usually well described by the Drude model of electron mobility:

$$\mu_{\text{Drude}}(\omega) = \frac{e\tau_S}{m^*} \frac{1}{1 - i\omega\tau_S}, \quad (3.1)$$

where τ_S is the momentum relaxation time (the mean free time between collisions of a carrier after which its velocity is randomized) and m^* is the effective mass of the carrier (electron or hole) in the given (conduction or valence) band. At a photocarrier density N , the transient conductivity of Drude carriers is

$$\Delta\sigma(\omega) = \frac{e^2 N}{m^*} \frac{\tau_S}{1 - i\omega\tau_S} = \epsilon_0 \omega_p^2 \frac{\tau_S}{1 - i\omega\tau_S}, \quad (3.2)$$

where ω_p is the plasma frequency of the photocarrier plasma.

Fig. 3.1(a) shows in lines the Drude fit of the THz response of photoelectrons in bulk rutile. The Drude model is based on a classical approach to the electron transport and was employed many times for the description of charge transport in bulk metals and semiconductors (we utilize it for bulk rutile in Chapter 8). It also describes charge transport in larger percolated parts of nanomaterials (Si microcrystals in [52], large Si nanocrystals in Chapter 6) or along nanowires [53].

The Drude model considers neither finite density of electron states nor a possible dependence of τ_S on the energy of carriers. These two effects can be taken into account by using the Boltzmann transport equation to calculate the conductivity spectrum of electrons in a given material but that approach is computationally demanding. [54] For conductivity spectra that slightly depart from the Drude model,

several phenomenological parametrizations are used, e.g. the Cole-Davidson (CD) model with exponent $\beta < 1$ and the Cole-Cole (CC) model with exponent $(1 - \delta) < 1$, where the exponents are introduced in the denominator of the Drude model as follows:

$$\Delta\sigma(\omega) = \frac{e^2 N}{m^*} \frac{\tau_s}{(1 - (i\omega\tau_s)^{1-\delta})^\beta}, \quad \beta, \delta \in (0;1). \quad (3.3)$$

The Cole–Davidson models was used for fitting equilibrium THz spectra of complex conductivity of silicon with extremely low carrier density $< 10^{13} \text{ cm}^{-3}$ by Jeon and Grischkowsky. [55,56] Beard et al. [57] studied THz photoconductivity of bulk GaAs and Si and extensively discussed the CC and CD models as well as their combination, as written in (3.3).

3.2. Hopping

Hopping represents a conduction process qualitatively different from band conduction. In materials with high densities of localized states such as defect states in the band gap of doped glasses and semiconductors or in specific molecular sites in organic crystals, electrons dwell in states below the conduction band edge.

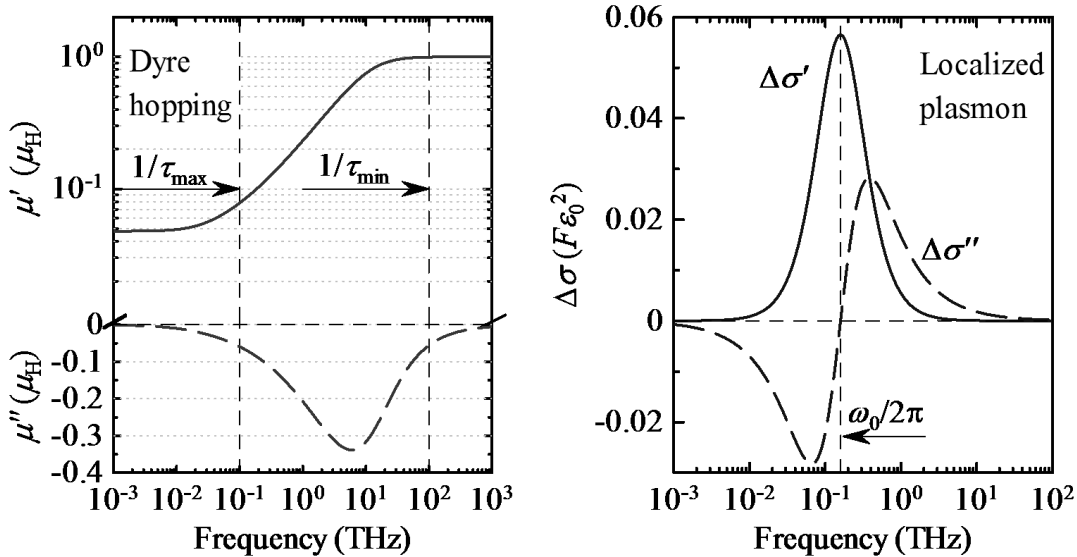


Fig. 3.2 Left: Dyre random free energy model of hopping mobility ($\tau_{\min} = 10 \text{ fs}$, $\tau_{\max} = 10 \text{ ps}$). Right: Localized plasmon conductivity model ($\omega_0 = 1 \text{ THz}$, $\gamma = 2 \text{ THz}$).

The Random free energy model introduced by Dyre [58] assumes that photocarriers jump randomly over energy barriers between the localized states with mobility

$$\mu(\omega) = i\omega\mu_H \left[1 - \frac{\ln(\tau_{\min} / \tau_{\max})}{\ln(1 - i\omega\tau_{\min}) - \ln(1 - i\omega\tau_{\max})} \right] \frac{\ln(\tau_{\max} / \tau_{\min})}{1/\tau_{\min} - 1/\tau_{\max}}, \quad (3.4)$$

where the frequency of the hops lies between $1/\tau_{\max}$ and $1/\tau_{\min}$. The formula describes a monotonous increase of the real part of the conductivity between the limit frequencies (Fig. 3.2). The low frequency and DC transport is determined by the hopping mobility amplitude μ_H and $1/\tau_{\max}$. The model ceases to be valid at frequencies high above $1/\tau_{\min}$ because it omits a necessary high-frequency conductivity drop due to finite carrier inertia. It was used e.g. to model transport of trapped carriers in hydrogenated microcrystalline silicon [43].

3.3. Localized plasmon

In contrast to the previous two models that describe mobility of individual charge carriers, the localized plasmon (LP) model characterizes the collective response of a carrier plasma in an isolated inclusion (such as in semiconducting nanoparticles). (It is also referred to as the localized surface plasmon as it describes the behavior of a surface plasmon in a sub-wavelength particle.) It is based on the consideration that positive and negative charges in the inclusion get spatially separated by an applied electric (THz) field — the opposite charges accumulate at opposite sides of the inclusion which subsequently exhibits an apparent polarization. The LP model describes the interaction between these two plasmas of opposite charges by a restoring electrostatic force that pulls the charge carriers back to their initial positions. The motion of charge carriers is then described as the response of a driven damped harmonic oscillator [52]

$$\Delta\sigma(\omega) = -i\omega\varepsilon_0 \frac{F}{\omega_0^2 - \omega^2 - i\omega\gamma} \quad (3.5)$$

where F is the oscillator strength, γ is the damping rate and ω_0 is the undamped resonance frequency. The resonance frequency is linearly proportional to the plasma frequency of the (photo)carrier ensemble enclosed within the inclusion

$$\omega_0 = \eta\omega_p = \eta\sqrt{\frac{Ne^2}{\varepsilon_0 m^*}}. \quad (3.6)$$

The proportionality constant η can be determined for inclusions of a given shape and orientation relative to the probing field direction. [53,59]

The overdamped limit of LP ($\omega_0 \ll \gamma$) is the Debye model with relaxation time $\theta = \gamma/\omega_0^2$

$$\Delta\sigma(\omega) = \frac{e^2 N}{m\gamma} \frac{i\omega\theta}{i\omega\theta - 1} \quad (3.7)$$

that can be used to describe the conductivity of carriers in a potential well or the diffusive type of conductivity at low-frequencies in 1D systems with energy barriers. [44]

The LP model is useful for modelling the macroscopic response of charge carriers in *diluted* ensembles of non-percolated NPs where the intra-nanoparticle

carrier interactions are much more important than inter-nanoparticle interactions (capacitive couplings across the gaps between adjacent NPs). The same case is equivalently described below in terms of the Maxwell Garnett effective medium approximation. For more complex geometries, another effective medium theory must be considered.

3.4. Effective medium response

Nanomaterials examined by THz spectroscopy are generally made of pieces of a semiconducting material dispersed in vacuum or in an insulating material that serves as the matrix. In the ground state, the matrix material is characterized by its permittivity ε_m and the semiconducting particles have a ground state permittivity ε_p . From the point of view of THz (= millimeter) waves, the material is inhomogeneous on the subwavelength scale and is seen as a homogeneous composite with a single *effective* (or *macroscopic*) permittivity ε . The measurable permittivity ε is related to the *microscopic* permittivities ε_m and ε_p *

$$\varepsilon = f_{\text{EMT}}(\varepsilon_m, \varepsilon_p, \dots), \quad (3.8)$$

where f_{EMT} is a function or a functional that also depends on the filling fractions and the morphology of the components. Various Effective Medium Theories (EMTs) have been formulated to concretize (3.8).

After photoexcitation, generated charge carriers exhibit a *microscopic* transient conductivity $\Delta\sigma^{\text{mic}}$, which contributes to the permittivity of the particles

$$\varepsilon_p \xrightarrow{\text{photoexcitation}} \varepsilon_p + \frac{i\Delta\sigma^{\text{mic}}}{\omega\varepsilon_0}. \quad (3.9)$$

This microscopic transient conductivity $\Delta\sigma^{\text{mic}}$ is the sought-after quantity that characterizes the transport of the electric charge *inside* the nanoelements. However, in the probing THz field, photocarriers are separated due to sample morphology (as in the LP concept) and the accumulated positive and negative charge clouds give rise to intra- and interparticle depolarization fields that sum with the probing field. The microscopic transient conductivity $\Delta\sigma^{\text{mic}}$ constitutes the response of the charge carriers to the *local* field which differs from the applied probing THz field. The composite thus exhibits a measurable *macroscopic* transient conductivity $\Delta\sigma$

$$\varepsilon \xrightarrow{\text{photoexcitation}} \varepsilon + \frac{i\Delta\sigma}{\omega\varepsilon_0}, \quad (3.10)$$

which is related to the microscopic one through the applicable EMT:

*We drop the frequency argument (ω) of ε and σ variables in the general EMT equations for the sake of legibility.

$$\begin{aligned}\Delta\sigma &= -i\omega\varepsilon_0 \left[\varepsilon^{\text{photoexcited}} - \varepsilon^{\text{groundstate}} \right] = \\ &= -i\omega\varepsilon_0 \left[f_{\text{EMT}} \left(\varepsilon_m, \varepsilon_p + \frac{i\Delta\sigma^{\text{mic}}}{\omega\varepsilon_0}, \dots \right) - f_{\text{EMT}} \left(\varepsilon_m, \varepsilon_p, \dots \right) \right].\end{aligned}\quad (3.11)$$

The microscopic transient conductivity $\Delta\sigma^{\text{mic}}$ can be retrieved from the macroscopic one only if one knows in which manner it is encoded therein, i.e. which form does f_{EMT} take in the particular sample. The mathematical complexity of the retrieval of $\Delta\sigma^{\text{mic}}$ from THz photoconductivity spectra is in a sense the trade-off for the experimental advantage of not needing any physical electrical contacts attached to the sample. We begin below with the concept of the depolarization factor A of a single polarizable particle and review three well known EMTs in order to present our own EMT transparently and in a wider context in the following chapter.

Depolarization factor and shape factor

The polarizability of a semiconducting nanoparticle in the THz frequency range occurs generally mostly due to the separation of electrons and holes (both conductive/valence or bound in excitons or localized in surface states), rather than ions. The local electric field in a single particle is

$$E_{\text{loc}} = E - A \frac{P}{\varepsilon_0}, \quad (3.12)$$

where P is the polarization of the inclusion caused by separation of charges in it due to the ambient THz field E . The dimensionless depolarization factor A is connected to the shape and orientation of individual nanoparticle. $A=1$ for a plane perpendicular to the field; $A=1/2$ for a cylinder perpendicular to the field and $A=1/3$ for a sphere. A (semi)conductor parallel to the field has depolarization factor equal to 0 — it does not polarize, naturally. Polarization in (3.12) is proportional to the microscopic permittivity of the particle and to the local field:

$$P = \varepsilon_0 (\varepsilon_p - 1) E_{\text{loc}}. \quad (3.13)$$

After substituting (3.13) into (3.12), one can factor out E_{loc} :

$$E_{\text{loc}} = E \frac{\varepsilon_m}{A\varepsilon_p + (1-A)\varepsilon_m}. \quad (3.14)$$

The first two EMTs mentioned below (Maxwell Garnett and Bruggeman) stem from this single-particle view and are suitable for description of composites with inclusions that all have the same shape (i.e. the same A). Their equations take simple forms when using an alternative of A , the so called shape factor $K \equiv 1/A - 1$. ($K=2$ for spheres or $K=1$ for cylinders perpendicular to the probing field.) The third well known EMT (Bergman) and also our approach (introduced in Chapter 4) are more clearly linked to the depolarization factor A .

3.4.1. Maxwell Garnett EMT

Maxwell Garnett (MG) theory [60,61] is one of the simplest EMTs and is applicable when one of the components forms *non-percolated* and rather sparse inclusions in the other component. The relation between the macro- and microscopic parameters takes a rather symmetric form

$$\frac{\varepsilon - \varepsilon_m}{\varepsilon + K\varepsilon_m} = s \frac{\varepsilon_p - \varepsilon_m}{\varepsilon_p + K\varepsilon_m}, \quad (3.15)$$

where s is the volume filling fraction of the non-percolated component (it may be either the semiconducting or the insulating component). In the case of semiconducting inclusions in an insulating matrix, the macroscopic transient conductivity in this approximation is related to the microscopic one as

$$\Delta\sigma = \frac{s(K+1)^2 \varepsilon_m^2}{\left(\varepsilon_m(s+K) + \varepsilon_p(1-s)\right)} \frac{\Delta\sigma_{\text{mic}}}{\left(\varepsilon_m(s+K) + \varepsilon_p(1-s) + \frac{i\Delta\sigma_{\text{mic}}(1-s)}{\omega\varepsilon_0}\right)}. \quad (3.16)$$

Mics shows in the Subsection 2.1.1 of his thesis [37] that when the transient *microscopic* conductivity of charge carriers in the inclusions follows the Drude model (3.2), the effective response of the composite takes the form of a damped harmonic oscillator

$$\Delta\sigma = \frac{s(K+1)^2 \varepsilon_m^2}{\left(\varepsilon_m(s+K) + \varepsilon_p(1-s)\right)^2} \frac{e^2 N}{m^*} \frac{-i\omega}{\omega_0^2 - \omega^2 - i\omega/\tau_s} \quad (3.17)$$

with damping $\gamma = 1/\tau_s$.

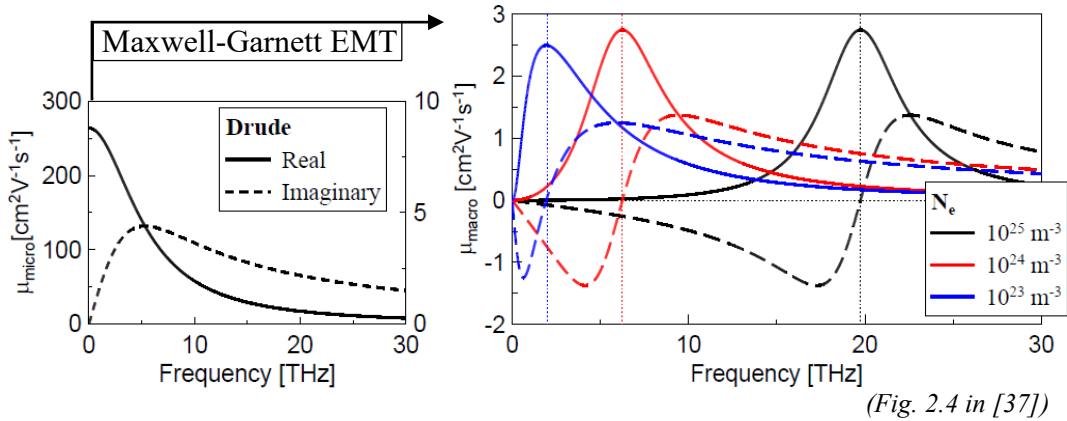


Fig. 3.3 Multi-THz mobility $\mu = \sigma/(e \cdot N_e)$ of a sparse semiconducting spheres with Drude type of microscopic conductivity — *left*: the microscopic mobility; *right*: the macroscopic mobility according to Maxwell-Garnett EMT at different carrier densities N_e .

This response is exactly equivalent to the conductivity of the localized plasmon (3.5) with the coefficient between the resonance and the plasma frequency (3.6) given

solely by the morphology of the structure and its *equilibrium* microscopic permittivities

$$\eta = \sqrt{\frac{1-s}{\varepsilon_m(s+K) + \varepsilon_p(1-s)}}. \quad (3.18)$$

The effective response of inclusions thus shows a resonance (see Fig. 3.3) at a frequency that shifts with the square root of carrier density (cf. (3.6)).

The MG model is exact in the limit of low filling fractions. [62] In that case, the impact of mutual capacitances between the inclusions on the macroscopic conductivity is negligible in comparison with the intra-nanoparticle effect of charge separation and plasmon oscillation.

3.4.2. Bruggeman EMT

The Bruggeman EMT treats the phases of a heterogeneous system completely symmetrically in a way similar to that of Maxwell Garnett. Each individual piece of the material with local permittivity ε_p , ε_m is considered as an inclusion that is embedded in the rest of the composite which possesses the effective (macroscopic) permittivity ε . The two materials are thus treated symmetrically. The Bruggeman mixing rule can be easily derived using the MG formula (3.15): ε plays the role of the matrix in the Bruggeman model, therefore the permittivity of the matrix ε_m is replaced by ε in (3.15) and a second term is added to the right-hand-side of the equation to account for the inclusions of the matrix material present in the rest of the composite with the complementary filling fraction $(1-s)$. The Bruggeman formula then reads:

$$\frac{\varepsilon - \varepsilon}{\varepsilon + K\varepsilon} = s \frac{\varepsilon_p - \varepsilon}{\varepsilon_p + K\varepsilon} + (1-s) \frac{\varepsilon_m - \varepsilon}{\varepsilon_m + K\varepsilon} \equiv 0. \quad (3.19)$$

The numerator on the left hand side is clearly identical to zero and one obtains the Bruggeman summation [63] in which the matrix and the photoconductive particles play symmetrical roles. The formula (3.19) is additive and can be expanded with another fraction describing a third component of the composite with a different permittivity and/or shape factor.

In contrast to the MG model, The Bruggeman EMT is valid for any filling fraction s . However, it dictates the following percolation thresholds of the two components based only on their filling fractions and depolarization factor, independent of different possible spatial arrangements. For $s > 1/(K+1) \equiv A$ the photoconductive component is percolated and it is non-percolated for lower values. The percolation threshold is found analogically for the matrix with filling fraction $(1-s)$. In the case of spherical inclusions, for instance, the semiconductor is non-percolated for $s < 1/3$, matrix is non-percolated for $s > 2/3$ and both are required to be percolated in between. Vice versa, with photoconductive cylinders perpendicular to the field ($A \geq 1/2$), the two components for can never be percolated simultaneously. In morphologies composed of higher portions of non-percolated

inclusions or with more complex percolation morphology, another EMT must be used.

3.4.3. Bergman EMT

The Maxwell Garnett EMT characterizes the photoconductive inclusions with a single shape factor; the Bruggeman EMT can take into account a specific distribution of shape factors but requires mathematical bonds between filling fractions and percolation thresholds of individual components. The Bergman EMT, in contrast, is technically able to parametrize a two-component system of any morphology, e.g. a sample containing both percolated and non-percolated semiconducting elements with a continuous distribution of shape factors in a matrix. We first overview several equivalent formulations of the Bergman EMT that occur in the literature and then shortly discuss its properties. The material is described by the volume filling fractions of the percolated parts V_m and V_p (called also percolation strengths) of the matrix and the photoconductive components, respectively, and by a so called spectral function (or distribution) $v(l)$, which characterizes the density of non-percolated parts with various shapes (denoted by the parameter l : $0 < l < 1$) in the sample.

In the general case, the spectral function and the filling fractions are normalized as

$$V_m + V_p + \int_0^1 v(l) dl = 1. \quad (3.20a)$$

$$V_p + \int_0^1 v(l) dl = s \quad (3.20b)$$

The effective permittivity of the structure is then given by an integral over the whole spectral distribution

$$\varepsilon = V_m \varepsilon_m + V_p \varepsilon_p + \int_0^1 \frac{v(l) \varepsilon_m \varepsilon_p}{l \varepsilon_p + (1-l) \varepsilon_m} dl. \quad (3.21)$$

We use this variant of the Bergman EMT that is more suitable for interpretation of our VBD EMT in the next chapter. The Bergman EMT is more frequently found in an equivalent form in the literature [64–66] with a different definition of the spectral function and of the percolation factor:

$$\frac{\varepsilon}{\varepsilon_m} - 1 = s \left[C_p \left(\frac{\varepsilon_p}{\varepsilon_m} - 1 \right) + \int_0^1 \frac{g(l)}{\frac{\varepsilon_m}{\varepsilon_p - \varepsilon_m} + l} dl \right], \quad (3.22)$$

where C_p is the percolation factor of the photoconductive material (the portion that is percolated) and $g(l)$ is a variant of the spectral density function:

$$C_p = \frac{V_p}{s}, \quad \nu(l) = -s \frac{g(l)}{l}. \quad (3.23)$$

The normalized percolation strength is sometimes included as a delta function in an extended spectral function [67]:

$$g_{\text{ext}}(l) = \begin{cases} C_p \delta(l), & l = 0 \\ g(l), & 0 < l < 1 \end{cases}, \quad (3.24)$$

reducing (3.22) to

$$\varepsilon = \varepsilon_m \left[1 + s \int_0^1 \frac{g_{\text{ext}}(l)}{\frac{\varepsilon_m}{\varepsilon_p - \varepsilon_m} + l} dl \right]. \quad (3.25)$$

Bergman [68] and Bergman and Stroud [69] equivalently represent the spectral function $g_{\text{ext}}(l)$ with a sum of real simple poles $0 \leq s_n < 1$ of the integrand in (3.25) with real positive residues $0 < F_n < 1$

$$\frac{\varepsilon}{\varepsilon_m} - 1 = \sum_n \frac{F_n}{\frac{\varepsilon_m}{\varepsilon_p - \varepsilon_m} + s_n}, \quad (3.26)$$

where the residues are normalized to the filling fraction of the photoconductive component:

$$\sum_n F_n = s. \quad (3.27)$$

A comparison of the denominator in the integral of (3.21) to that in the local electric field in a polarizable inclusion (3.14) suggests that the parameter l has the intuitive meaning of the depolarization factor A . Indeed, in the limit of very low filling fractions (inclusions with negligible mutual electrostatic interaction), the spectral distribution would feature a series of delta peaks positioned at the depolarization factors belonging to the respective shapes present in the sample ($l = A$) and their amplitudes would correspond to the values of the filling fractions of these shapes. With increasing filling fractions, mutual capacitive coupling between individual (photo)conductive inclusions increasingly change their polarizability in a complex way. This behavior is represented by widening and shifting of the peaks in the spectral distribution $\nu(l)$ and even by completely new peaks arising due to complex electrostatic couplings between near and far parts of the structure. This observation shows the general character of this description, compared to the terminology of discrete depolarization factors.

From the mathematical point of view, in the case when one of the permittivities is negative (metallic behavior), there exists an l (or A in (3.14)) for which the denominator vanishes. The contribution of the integral to the effective

permittivity then describes plasmon oscillations in inclusions of a particular shape (localized plasmon resonance). The spectral function $\nu(l)$ can thus also be understood as the distribution of oscillator strengths for the different shapes of semiconducting inclusions present in the sample.

The Bergman EMT is seldom used to interpret experimental data because the spectral function of the particular sample cannot be usually easily found (see the related discussion in [65,66]). In our work it provided us with a background for the development of a simpler expression which appeared to be particularly suitable for the interpretation of THz photoconductivity spectra and which is described in Chapter 4.

3.5. Monte Carlo simulations of carrier confinement

Our group has developed a program that calculates the mobility spectrum of classical thermal motion of a charge carrier in a semiconductor (nano)particle of a given shape [70]. The main physical input variables are:

- size and shape of the semiconductor nanoparticles (cubes, spheres, ellipsoids);
- scattering time of the carrier in the bulk volume of the particle, together with carrier velocity it defines the carrier mean free path l_{free} ;
- temperature and velocity distribution (Maxwell-Boltzmann or Fermi-Dirac) from which the carrier randomly selects its velocity magnitude after a scattering event;
- probabilities that the carrier scatters at, reflects from or tunnels through the particle boundary to an adjacent particle;
- distribution of a static electric and/or magnetic field inside the particle.

The algorithm records the carrier velocity vector coordinates v_i ($i = x, y, z$) in time t' for a statistical ensemble of initial conditions and trajectories determined by the temperature T . The Kubo formula then yields its mobility spectrum from the velocity autocorrelation function [71]:

$$\mu_{ij}(\omega) = \frac{e}{k_B T} \int_0^{\infty} \langle v_i(0) v_j(t') \rangle \exp(i\omega t') dt', \quad i, j = x, y, z, \quad (3.28)$$

where k_B is the Boltzmann constant and brackets denote averaging over a canonical ensemble with given temperature. Note that μ_{ij} is generally a tensor — its diagonal elements describe motion along the axes (these are identical when modeling isotropic structures); the off-diagonal elements reflect the impact of possible external magnetic field on the carrier motion, as discussed in [72]. The simulation program is capable to take into account other processes such as carrier trapping on bulk and surface defects and their thermal reemission or the presence of a non-uniform electric field in the nanocrystals.

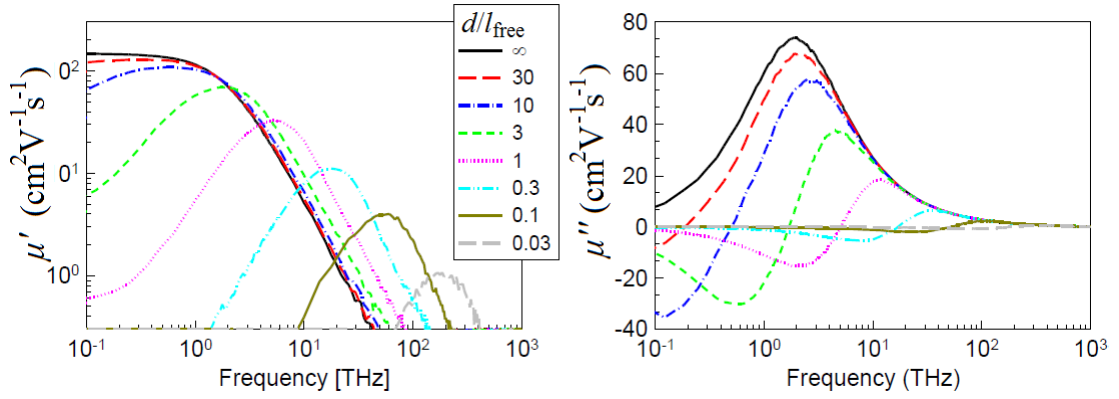


(FIG. 1. in [70], notation adapted)

Fig. 3.4 Mobility spectra of carriers ($m^* = 1 m_e$) at 300 K (thermal velocity 1.17×10^5 m/s, scattering time 85.6 fs) in isolated spherical particles (100% probability of carrier reflection at particle boundary) with various ratio of nanocrystal diameter d and carrier mean free path.

Fig. 3.4 shows the calculated mobility spectra of a carrier in an isolated spherical particle with different ratios between the particle diameter and the carrier mean free path. With infinite particle diameter (black line), the carrier exhibits a bulk behavior and shows the Drude type of mobility. With a finite inclusion diameter, the theoretical DC mobility must drop to zero because the insulating boundaries of the inclusion deny the long-range transport. The real mobility peak (centered at zero frequency for Drude mobility) shifts with decreasing particle size to a higher frequency that is related to the round-trip of the carrier in the inclusion. [70] The imaginary part of the mobility simultaneously decreases to negative values in the range below the resonance frequency, producing a capacitive type of response there.

This type of spectral change is qualitatively (!) similar to that caused by the depolarization fields in samples with non-percolated nanoparticles, compare in Fig. 3.4 and Fig. 3.3.

3.6. Remarks on nanoscale conductivity

We have shown in the previous two sections that the capacitive type of photoconductive response is own to nanomaterials but that it may be produced by two different effects: the effective medium response of a non-percolated composite and confinement of charge carrier in individual nanoparticles. Let us point out the difference.

On the *nanoscale*, the *microscopic* mobility of carriers depends dramatically on the *size* of the confining nanoparticle (Fig. 3.4): with particle size below the carrier mean free path, the mobility changes from inductive to capacitive. The carrier *density* does not play a role here (carrier–carrier interaction may come into play at high densities).

By contrast, the absolute *size* of the photoconductive particles does not play any role in their *macroscopic* (effective) response. Instead, the macroscopic

conductivity of the composite depends strongly on the carrier *density* (or, strictly speaking, on their microscopic conductivity), see Fig. 3.3.

We thus see that the capacitive type of THz photoconductive response is not necessarily connected to charge carrier localization on the most expected length scale (usually the size of an elementary building block of the nanomaterial) and a more detailed analysis should ensue from such results. For example, Mics et al. [47] studied THz photoconductivity of CdS nanocrystals (NCs) with diameters of 10.4 nm and observed capacitive type of response. Their analysis of depolarization fields and possible arrangements of the sample surprisingly showed that charge localization occurs at ~ 40 nm length scale. Transmission electron microscopy (TEM) images then confirmed that individual 10-nm NCs were packed to clusters of a corresponding size.

3.7. Drude-Smith model

In 1968, N. V. Smith proposed a modification of the Drude model to describe the unusual, capacitive-like conductivity of mercury — such behavior is very uncommon among both liquid and solid metals. [73] His so-called Drude-Smith (DS) model was used later on by different groups to fit the THz photoconductivity spectra of nanostructured semiconductors, although the physical interpretation of its fitting parameters remained unclear, namely in the cases when the effect of the depolarization fields was not carefully evaluated. In 2009, Nĕmec et al. [70] published an analysis trying to relate the parameters of the DS model to actual physical properties of a wide range of model systems. Below, we review the DS model and its drawbacks according to that paper.

Smith suggested that “the backscattering of the electrons in mercury is so strong that, after a time of the order of the scattering time τ , an electron tends to reverse its direction of motion.” [73] To describe this assumption, he introduced the parameter c_p (denoted originally β) as “the expectation value of $\cos \vartheta$ after a collision where ϑ is the scattering angle” [73], which is supposed to be the measure of persistence of the initial velocity of an electron after p collisions. (The collisions are counted from the beginning of the motion of the electron when it was accelerated with a unit impulse of electric field.) The complex conductivity with Drude-Smith time τ_{DS} then reads [74]:

$$\Delta\sigma(\omega) = \frac{Ne^2\tau_{DS}}{m^*} \frac{1}{1-i\omega\tau_{DS}} \left[1 + \sum_{p=1}^{\infty} \frac{c_p}{(1-i\omega\tau_{DS})^p} \right]. \quad (3.29)$$

Smith pointed out that in the case of independent collision, $c_p = (c_1)^p$, (3.29) actually does not lead to qualitatively new behavior as it is easily summed up to take the form of the Drude conductivity (3.2) with a modified scattering time $\tau_s = \tau_{DS}/(1-c_1)$. To benefit from the new parameter c_p , Smith truncated the series by setting $c_p = 0$ for $p > 1$ and thus introduced the so-called *single scattering approximation*. The conductivity of mercury was fitted with the obtained equation

$$\Delta\sigma_{\text{Drude-Smith}}(\omega) = \frac{Ne^2\tau_{\text{DS}}}{m^*} \frac{1}{1-i\omega\tau_{\text{DS}}} \left[1 + \frac{c_1}{1-i\omega\tau_{\text{DS}}} \right], \quad (3.30)$$

yielding a good agreement with experimental data with $N = 2.7$ electrons per atom and $c_1 = -0.49$. Equation (3.30) is since then referred to as the Drude-Smith model of conductivity. The justification for single scattering approximation was unclear in the original work of Smith [73]. In 2001, Smith suggested that only the first scattering is ballistic, with preferential backscattering, and the following events are diffusive [74].

In samples with DS type of THz (photo)conductivity, it is assumed that the first collision of a carrier accelerated by the probing THz field is its backscattering on the boundary of the nanoparticle in which it was generated and the following scattering events in the volume of the particle are random. The parameter c_1 with values between 0 and -1 is then interpreted as the extent of the localization of carriers inside the particles. [75]

Němec et al. [70] fitted the Drude-Smith model to the broadband mobility spectra calculated from the Monte Carlo simulations (cf. Section 3.5) of classical motion of a charge carrier in various systems of particles. They found out that:

- The DS model fits well the carrier mobility only when a limited part of the spectral range is considered.
- The low-frequency extrapolation of the DS model that was fitted on actual (experimental, simulated) data in a limited spectral range may lead to quantitatively wrong conclusions on long-range transport in the NP system.
- An analytical connection between the DS parameters c_1 and τ_{DS} and physical transport parameters of the nanosystem (namely the probability of carrier backscattering on the particle boundary, bulk scattering time τ_{S} and the time of carrier round trip in the particle) can be found only when the diameter of the particle is smaller than l_{free} .

The truncated DS model is thus physically adequate for describing the *microscopic* conductivity of particles that are smaller than the mean free path of the charge carriers in them. [70] Nevertheless, in this case the depolarization fields that affect the measurable macroscopic conductivity should be taken into account independently; the DS model should be put inside an applicable EMT in the place of the microscopic conductivity term $\Delta\sigma^{\text{mic}}$ to obtain a model of the measurable *macroscopic* conductivity $\Delta\sigma$. If this step is overlooked, the Drude-Smith parameters may lose their physical significance completely as described below; in addition, they would strongly depend on the photocarrier density.

The review of experimental papers in Section 3.9 shows that this procedure was not always followed in practice — the DS model has been relatively frequently used to fit the measured *macroscopic* response of different nanomaterials. Below we show that this approach cannot yield physical information as it leads to intermixing of several phenomena in too few parameters. With $c_1 = 0$, the DS model clearly

reduces to the Drude conductivity of an ensemble of delocalized electrons (3.2). In the other limit, $c_1 = -1$, equation (3.30) can be easily rearranged into the form of a damped harmonic oscillator:

$$\Delta\sigma(\omega) = \frac{Ne^2}{m^*} \frac{-i\omega}{(1/\tau_{\text{DS}})^2 - \omega^2 - 2i\omega/\tau_{\text{DS}}}, \quad (3.31)$$

where, adopting the localized plasmon notation according to (3.5), the undamped angular frequency $\omega_0 = 1/\tau_{\text{DS}}$ and the damping rate $\gamma = 2/\tau_{\text{DS}}$ are bound together in a fixed ratio $\gamma = 2\omega_0$, which represents critical damping of the oscillator.

The DS parameter c_1 thus constitutes a smooth parametrization of a transition between two special cases of *macroscopic* conductivity: Drude model and the localized plasmon model in the regime of critical damping. However, even the simplest example of macroscopic response of particles with Drude microscopic conductivity within the Maxwell Garnett EMT (3.17) showed that there is no requirement for the plasma frequency and the damping rate to be bound in an exact ratio. The DS model is thus essentially under-parametrized for the purpose of physical interpretation of *macroscopic* response of a composite (although it often provides satisfactory fits in a limited spectral range). In other words, if the DS model is used to fit directly the measured THz conductivity spectra, the effects of both the carrier confinement and depolarization fields are mixed in each of the DS fitting parameters c_1 and τ_{DS} and the physical interpretation of such fits would be completely obscure. The information obtained from DS fits of macroscopic THz photoconductivity spectra can be useful for categorizing the data and e. g. for describing evolution of the spectra in a series of samples with systematically varied parameters such as those presented in [76].

We use the DS model in this thesis solely as an instrument for analytical reproduction of Monte Carlo mobility spectra in a limited spectral range in order to speed up fitting with these spectra that are based on time-consuming simulations.

3.8. Quantum confinement

Quantum confinement, i. e. discretization and shifting of energy levels in a semiconductor due to decreased size of the crystal, is an important property of nanomaterials. It occurs on sizes below ~ 10 nm or less, depending on the material. Samples containing nanocrystals with substantial quantum confinement are studied in Chapter 6 but the size distribution of these NCs was too wide to enable monitoring of single energy levels by THz spectroscopy in this thesis. Hendry et al. [77] used kinetics of spectrally averaged transient THz response to observe electron-to-hole energy transfer in CdSe quantum dots (QDs) in dependence on QD diameter (from 1.7 to 10 nm). This was possible because the \sim meV energies of THz photons are small enough to avoid interband excitations in the QDs. The lowest energy hole state has the highest polarizability in the given system according to Wang et al. [78] and transient THz absorption thus served as a measure of the population of this state.

3.9. Published experimental works

A selection of experimental papers on THz photoconductivity gives an overview of the achievements and uncertainties of our method in the debated field. We mention some systems that may be relevant for our study. The results in this section are grouped into subsections by the studied material. First two parts are dedicated to semiconductors most relevant for this study — silicon and titanium dioxide. Some other inorganic nanocrystals are briefly review in subsection afterwards and the last subsection covers studies on 1-dimensional structures.

3.9.1. Silicon micro- and nanocrystals

Nienhuys and Sundström [52] investigated silicon microcrystals (1–30 μm in diameter, produced by grinding of a Si wafer) in a polymer matrix. They found a good agreement between the measured THz photoconductivity spectra and the localized plasmon model (3.5) and identified the plasmon damping time of about 150 fs with the Drude scattering time of electrons in the volume of microcrystals. The expected plasma frequency dependence $\omega_0 \sim \sqrt{N}$ (3.6) was approximately reproduced in the examined pump fluence range.

The group of Frank A. Hegmann [75] measured THz photoconductivity spectra of Si nanocrystals (NCs) in SiO_2 matrix produced by annealing of 1 μm thick SiO films. Samples with NC diameter from 3 nm to 7 nm and with an increasing average interparticle spacing of 0.7–1.4 nm were obtained. The Drude-Smith model was found to provide the best fit after considering also some other approaches (effective medium theory alone, two-site hopping model [79], localized Drude model [80]). The parameter of the Drude-Smith model c_1 decreased towards -0.98 with decreasing NC diameter. The non-zero DC transport corresponding to $c_1 > -1$ was confirmed by contact measurements; the fitted values of $\tau_{\text{DS}} \sim 15$ fs were successfully linked to the NC sizes.

In another paper of the same group [76], silicon-rich SiO_x ($x = 0.2\text{--}1.0$) films were annealed similarly to obtain samples of Si nanocrystals with different degrees of percolation in SiO_2 matrix with different degrees of percolation. The time evolution and Si-content dependence of the measured THz photoconductivity spectra were evaluated by using the Drude-Smith model and by random-walk simulations of carrier motion in a 3D array of closely packed nanospheres without bulk scattering. Percolation threshold for Si filling fractions above 38% was observed and a carrier diffusion length on the order of 100 nm was derived in percolated samples.

Fekete et al. [43] studied hydrogenated microcrystalline silicon with variable degree of crystallinity, prepared by plasma enhanced chemical vapor deposition from silane and hydrogen. The transient THz kinetics scans showed a sub-ps ultrafast component attributed to a Drude-like transport of carriers inside the grains with a mobility of $70 \text{ cm}^2\text{V}^{-1}\text{s}^{-1}$; within ~ 600 fs, the carriers got captured in shallow states at the boundaries of 20–30 nm large grains and the transport at longer times was dominated by the hopping process.

3.9.2. Titanium dioxide nanocrystals

Turner, Beard and Schmittenmaer [81] studied 25 nm large Degussa P25 TiO₂ nanoparticles sensitized with the Ru535 dye at 77 K. The carrier cooling was observed during the first ~300 fs and, at longer times, the carrier mean free path was estimated to range between 1.6 and 4.0 nm. The complex conductivity spectra were fitted by the Drude-Smith model and it was shown that charge carriers, whose long-range mobility is reduced by the disorder, are still quite mobile on a short range inside nanoparticles. From our perspective the parameters of the Drude-Smith model do not carry a clear physical meaning in this case since l_{free} was much smaller than the nanoparticle diameter.

Hendry et al. [82] also noted that the interpretation of the results in [81] using the DS model is problematical and they investigated samples sintered from the same commercial precursor (Degussa P25 TiO₂) without any sensitizing dye. Fits with the Drude model of microscopic conductivity within the Maxwell Garnett EMT reproduced well the main features of the measured THz photoconductivity spectra. Moreover, the carrier density and temperature dependences of the measured THz photoconductivity were fully explained as consequences of the dependence of the carrier mobility on these parameters. Carrier mobilities of ~0.01 cm²/(V·s) in the nanoparticles and ~1 cm²/(V·s) in a reference bulk rutile sample were reported at room temperature.

The study by Němec et al. [70] presenting Monte Carlo simulations and comparing them with the Drude-Smith model of the conductivity (cf. Section 3.5), was supported by experimental data measured on 7 nm TiO₂ and 15 nm ZnO NCs. The effective response of the samples was found to be a linear function of the microscopic carrier conductivity because the NCs were conductively percolated. Fitting of the experimental data with the mobility spectra obtained by Monte Carlo calculations provided reasonable values of the quantum yield of photoexcitation and of the probability of carrier backscattering on NC boundaries.

Nanocrystalline mesoporous films made of 4 nm percolated TiO₂ were also studied by Němec et al. [83] and the Monte Carlo method gave excellent fits to the spectra, providing microscopic parameters of the carrier localization. The NCs were dielectrically percolated or at least “glued” together with amorphous titania and linear scaling between microscopic and effective conductivity was justified.

In another paper of Němec et al. [48] a comparison of sub-ps dynamics of charge carrier injection in two pairs of samples made of 9 nm TiO₂ and 15 nm ZnO NCs sensitized with two different dyes (Ru- and Zn-based) showed a striking difference between the two materials, independent of the dye. Electrons in TiO₂ exhibit a low mobility due to the very strong electron-phonon coupling in contrast with ZnO where the electron mobility is higher by nearly two orders of magnitude. On the other hand, sensitized TiO₂ NCs accept photoelectrons from the excited dye molecule much faster than ZnO NCs because the high permittivity of TiO₂ provides better screening of the excited dye cation. Attraction between the dye cation and the injected electron then significantly slows down the transport in ZnO. Spectra of THz

photoconductivity were interpreted within the framework of the Monte Carlo method that took into account distribution of the electric field of the dye cation inside the NCs. [3]

Tiwana et al. [84] studied THz photoconductivity kinetics both in dye-sensitized and bare sintered films of 20 nm TiO₂ nanoparticles. In the bare films, the photoconductivity onset was faster than the experimental time resolution and the signal decayed on the ~1.5 ns time scale. Sensitization with a Ru-based dye led to an appreciable slower injection speed — the photoconductivity kinetics displayed a 70 – 200 ps rise followed by a ~5 ns decay. Mobility of about 0.1 cm²/(V·s) was reported at room temperature both in the bare and dye-sensitized samples.

Another study of this group [85] compared the THz photoconductivity kinetics in three promising photovoltaic materials, nanoporous films of TiO₂, ZnO and SnO₂ sensitized with the same dye. Parallel transient device photocurrent measurements showed a correlation between the in-device carrier mobility and the rate of early-stage carrier injection rate observed by THz spectroscopy. The carrier injection into TiO₂ was faster (in accord with the findings of Němec et al. [48]) and the in-device mobility was closer to the bulk value than in the other two oxides.

3.9.3. InP, InGaAs, CdS, CdSe, VO₂ nanoparticles

Beard et al. [86] observed almost purely imaginary capacitive THz photoconductivity in disordered arrays of InP nanoparticles (3.2 nm in diameter). The photoconductivity increased 6 times when the average spacing between NPs was decreased from 1.8 to 0.9 nm and the spectra were fitted with the Drude-Smith model. Transient THz kinetics scans showed that NPs with smaller spacing have longer trapping time; this was attributed to enhanced inter-NP tunneling. Control sample of bulk InP epitaxial layer displayed relatively slow (~3 ps) photoconductivity onset due to the scattering of hot electrons to low-mobility L and X valleys, this process was missing in samples with nanoparticles.

In another study [87], this group successfully used the Bruggeman EMT with Drude mobility to characterize the size-dependence of THz photoconductivity in CdSe nanoparticles of various sizes between 2.5 and 25 nm. The decrease of electron mobility with particle size was explained in terms of scattering on nanoparticle boundaries at sizes above the electron Bohr radius (4.9 nm).

Merchant et al. [88] studied depletion regions around surface states at 50 nm pores in S-doped nanoporous InP membranes by means of both transient and equilibrium THz spectroscopy. In the steady state, the depletion regions of adjacent pores nearly touch and carriers in the remaining non-depleted regions exhibit localized (capacitive) response of the membrane. Upon photoexcitation, the depletion regions narrow as many of the pore surface states fill and the conductive photocarriers exhibit Drude type of conductivity

Cocker et al. [89] investigated metal-insulator transition of nanogranular VO₂ (94 ± 26 nm grain diameter) film between 320 and 390 K by steady-state THz spectroscopy. The variation of the macroscopic conductivity with temperature

(changing filling fractions of grains in metallic and in insulating state) could not be reproduced using Bruggeman nor Maxwell Garnett EMT with Drude microscopic mobility. Direct fit with the Drude-Smith model and evaluation of its amplitude (via plasma frequency) yielded electron densities in the metallic state consistent with values reported elsewhere. The condition of comparable carrier mean free path and nanoparticle size (cf. Section 3.7) was partly justified.

Mics et al. [47] studied a thin film of 10 nm CdS nanocrystals prepared from chemical bath followed by annealing. Fits of the THz photoconductivity spectra with the result of Monte-Carlo calculations showed that electron localization occurs at length scales > 28 nm, suggesting that groups of adjacent NCs are in a good conductive contact and form aggregates that are mutually connected only by narrow channels. THz photoconductivity spectra and kinetics measured at different excitation densities and with two pump photon energies revealed existence of energy barriers between the NCs; electrons with high excess energy (soon after photoexcitation or at high excitation densities due to band filling) showed higher probabilities of passing to adjacent NCs and clusters.

3.9.4. Quantum wires, nanotubes

Parkinson et al. [53] examined an array of randomly oriented GaAs nanowires (50–100 nm in diameter, 5–10 nm long). They successfully fitted THz photoconductivity spectra with a sum of the Drude model (conductivity of nanowires parallel to THz field) and a localized plasmon mode (conductivity of perpendicular nanowires). The same sum conductivity model was successfully used in their next study [90] that compared THz photoconductivity spectra and dynamics of GaAs nanowires after different production and post-growth conditions. The importance of surface passivation was pointed out in order to increase carrier lifetime in GaAs, based on experimental results.

In another paper of this group [91], THz (photo)conductivity of randomly oriented GaAs, InAs and InP nanowires of various diameters (20-200 nm) was compared. The localized plasmon model was used and the behavior of plasma frequency ($\omega_p \sim N^{1/2}$) was examined in detail. The THz photoconductivity kinetics showed a decrease of carrier lifetime with decreasing NW diameter due to the surface recombination in all 3 materials. InP NWs showed the lowest surface recombination velocity and were studied further in [92] with the help of time-resolved photoluminescence and HRTEM* images of the NWs. HRTEM images revealed transversal stacking faults that on the one hand increase the carrier scattering rate but, on the other hand, effectively separate electrons from holes and thus increase the carrier lifetime.

The first Optical pump–THz probe study of GaN nanowires [93] was also accomplished by the group of Parkinson et al. High-quality NWs grown by

* High-resolution transmission electron microscopy

molecular-beam epitaxy exhibit a ~ 2.5 ns lifetime which is several times longer than in bulk and thin film samples. Conductivity spectra of randomly oriented NWs lying on a substrate were successfully fitted with the sum Drude+LP model yielding a mobility of $800 \pm 100 \text{ cm}^2 \text{V}^{-1} \text{s}^{-1}$ in the NWs, comparable to or higher than in a reference commercial bulk sample.

The group of Frank A. Hegmann [94] detected large anisotropy in the photoconductivity of a high-mobility 2D wetting layer of InGaAs which had parallel chains of self-assembled InGaAs quantum dots on it. Transient THz kinetics revealed that the nanochains act as fast and efficient traps for carriers moving perpendicular to them in the 2D wetting layer at low temperatures while thermal emission from the nanochains and nanodots into the 2D wetting layer dominates the THz photoconductivity spectra at temperatures above 90 K.

The same group found [95] also a strong anisotropy in transient THz kinetics of laterally ordered InGaAs quantum wires embedded in a GaAs matrix. Here, the carriers excited in the matrix and in the wetting layer were captured in the quantum wires in the first 6-30 ps after photoexcitation and then showed the Drude type of mobility along the nanowires.

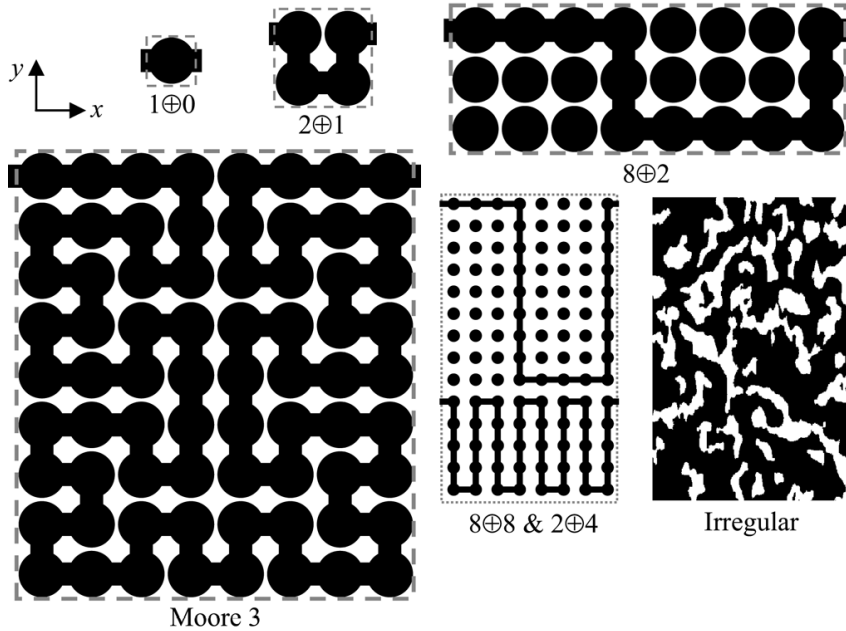
Ponseca et al. [96] measured the transverse THz photoconductivity of a regular array of heavily Sn-doped InP nanowires (150 nm in diameter). The structure exhibited strong waveguiding effects of the excitation light that were evaluated by precise numerical calculations. The mobility of electrons localized in the transverse direction of the NWs was evaluated by Monte Carlo simulations (cf. Section 3.5). Sets of THz photoconductivity spectra measured over a wide range of excitation densities at two pump wavelengths (400 nm and 610 nm) were successfully fitted with the effective conductivity obtained from the Monte Carlo mobilities through Maxwell Garnett EMT.

4. VBD effective medium theory

The VBD effective medium model was developed in our group on the basis of numerical calculations of electric field distribution in nanomaterials with various morphologies. The formula for the effective conductivity/permittivity of a composite that we propose within this model may be understood from a simple equivalent electric circuit approach depending on 3 parameters: V , B , D . In this Chapter, we first summarize the derivation of the model that we published in [97]. Next, we relate it to the experimental method of this thesis. We interpret the parameters V , B , D in terms of the Maxwell Garnett EMT for some morphologies and we further show that the model can be understood in the framework of the Bergman effective medium approach with a *single* representative depolarization factor. The model itself was developed by Ivan Rychetský, Hynek Němec and Petr Kužel; the author participated in the discussions and interpretations of the model in the later parts of this Chapter.

4.1. Effective permittivity calculation

Numerical electrostatic calculations were carried out with a number of model structures. Fourteen different periodic two-dimensional structures consisting of spherical particles and linear connectors with an equilibrium permittivity of $\varepsilon_p = 35$ in a matrix with the permittivity $\varepsilon_m = 1$ were designed (Fig. 4.1 shows several examples).



(selection from Fig. 1. in [97])

Fig. 4.1 Examples of 2D structures examined in presented model; *black*: particles with adjustable permittivity, *white*: dielectric matrix, *gray dashed line*: boundary of elementary periodic unit cell.

Each structure was non-percolated along the y coordinate and featured a more or less complex percolation pathway across the unit cell along the x coordinate and thus it was utilized to obtain data for both percolation regimes in our calculations. Four different classes of structures were analyzed:

- 7 structures were variants of a simple chain type “ $n\oplus m$ ” (first row in Fig. 4.1); purpose: inspecting the effects of the length of the pathway and of the spacing between parallel sections of the pathway.
- 4 structures combined 2 different types of simple chains — like the “ $8\oplus 8$ & $2\oplus 4$ ” structure in Fig. 4.1 inspecting a possibly different coupling between the chains than in simple chain structures.
- 3 fractal structures showed the effects of increasing fractal complexity of backward meanders, starting from one of the simple chains and ending with “Moore 3” in Fig. 4.1.
- 2 irregular structures (one percolated, shown in Fig. 4.1, and one non-percolated) were investigated as a reference to the ordered ones.

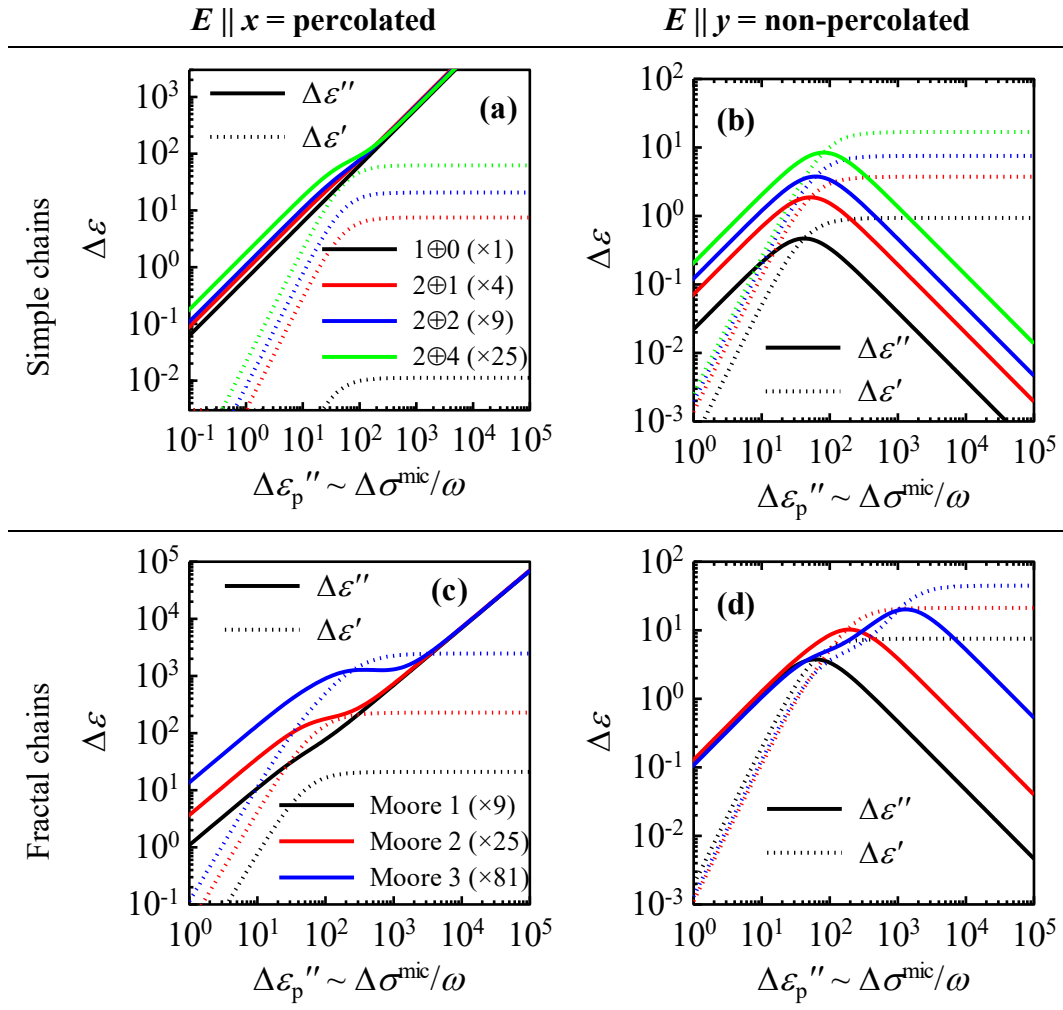
The structures were approximated by non-uniform triangular meshes by a suitable image processing procedure [98] for the purpose of the numerical calculations.

The distribution of the local electric field $\mathbf{E}(x, y)$ in each structure upon applying external static electric field along one of the coordinates was calculated by solving quasi-static Maxwell equations with periodic boundary conditions using the finite element method (namely the programming language FreeFem++ and the software of the same name). The calculated *distribution* of electric energy was *averaged* over the volume of the unit cell and equated to the situation where the same amount of energy was distributed *homogeneously* in a unit cell with the permittivity ε :

$$\frac{1}{2V} \iint_V \varepsilon(x, y) \mathbf{E}^2(x, y) dx dy = \frac{1}{2V} \varepsilon \iint_V \mathbf{E}^2(x, y) dx dy, \quad (4.1)$$

where $\varepsilon(x, y)$ is the microscopic permittivity in the structure, i.e. it equals ε_p inside particles and ε_m inside the matrix. The calculated permittivity ε then represents by definition the effective (macroscopic) permittivity of the structure in the non-photoexcited state.

Finally, an imaginary contribution $i\Delta\varepsilon_p''$ was added to the particle permittivity ε_p (in order to simulate the photoexcitation) and the calculation was repeated for a wide range of values of $\Delta\varepsilon_p''$. The complex valued change $\Delta\varepsilon$ of the effective permittivity (with respect to its equilibrium value ε) as a function of the additional imaginary permittivity of the particles $\Delta\varepsilon_p''$ was thus obtained. We further refer to $\Delta\varepsilon$ and $\Delta\varepsilon_p''$ as to the transient effective permittivity and transient imaginary permittivity or particles, respectively, to keep in the context of the thesis chapters. However, we stress that the field calculations above are performed in the quasi-static limit and the adjective *transient* refers only to the fact that transient (photo)excitation is used to induce these changes in the experiment.



(selection from Fig. 2. in [97], labels added)

Fig. 4.2 Calculated dependences of the change of effective permittivity on the transient imaginary permittivity of particles in examined structures with the field applied (a,c) along the percolation pathways and (b,d) perpendicular to the percolation pathways. Color legend is the same for both plots on a row.

Fig. 4.2 shows $\Delta\varepsilon(\Delta\varepsilon_p'')$ dependences for several simple chain and fractal morphologies for the field applied along x and y (i.e. in both percolation regimes). Both the real part (dashed lines) and the imaginary part (full lines) of transient effective permittivity show a power dependence for $\Delta\varepsilon_p'' < 10$, and the power dependences have the same slopes in the log-log scale for all percolated and non-percolated structures. For high values of the particle transient permittivity ($\Delta\varepsilon_p'' > 10^3$ in chains and $\Delta\varepsilon_p'' > 10^4$ in the most complex fractal Moore 3), the real part of effective permittivity shows a saturated behavior in both percolation regimes. The imaginary effective permittivity, in contrast, shows a distinct difference between the percolation regimes for high $\Delta\varepsilon_p''$: it further *increases* steadily for percolated structures (Fig. 4.2(a,c)) and it *decreases* for non-percolated structures

(Fig. 4.2(b,d)). A transition region is observed in between, whose spectral width increases with increasing complexity of the structure.

Compared to the phenomena observed in Fig. 4.2, neither the irregular structures, nor the other periodic ones exhibited qualitatively new features in the effective permittivity dependences. Before we analyze the obtained dependences further, let us introduce the *equivalent electric circuit* model. It provides an analytic formula that fits these dependences well and gives an intuitive interpretation of the calculated response of examined structures.

4.2. Equivalent electric circuit model

Our EMT works in the quasi-static approximation and thus we can consider electric circuit analogies to our structures on the same level of approximation. The particles in the photoexcited state are basically just pieces of a conductor that 1) are connected along the percolation pathways into wires with some resistivity and/or 2) behave as capacitors with certain capacitance wherever they are separated from each other by a sheet of the dielectric matrix in the direction of the applied field. We want to find the simplest possible electric circuit whose response is in a general agreement with the results of the numerical simulations above. Fig. 4.3 shows the two simplest circuits that may represent a percolated and a non-percolated structure.

The capacitor C_{NP} in the RC branches in both circuits accounts for the capacitance of the matrix-filled gaps between the non-percolated particles or between parallel sections of particle chains and the resistor R_{NP} stands for the resistance across these elements in the direction of the applied field. The lower branch in Fig. 4.3(a) stands for the resistance along the percolation pathway R_p . (A rigorous analogy would require additional parallel R and RC branches for different pathways and different capacitive gaps that can be found in the modeled structures. As it will be shown later, single representative capacitive and resistive factors satisfactorily describe the response of most structures.)

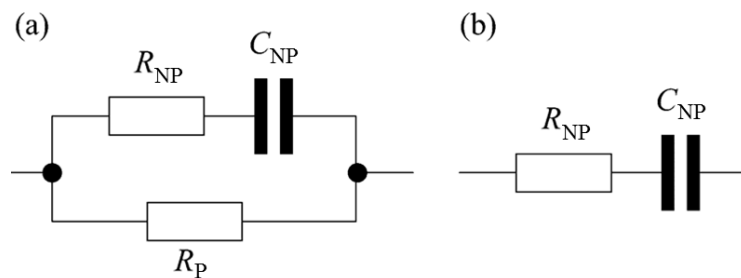


(Fig. 3. in [97], notation adapted)

Fig. 4.3 Equivalent electric circuits of modelled structures: (a) with and (b) without a percolation pathway.

The admittance of the circuits in Fig. 4.3 is simply found as

$$Y = \frac{1}{R_p} + \frac{\frac{1}{R_{NP}}}{1 + \frac{i}{\omega C_{NP} R_{NP}}}, \quad (4.2)$$

with the standalone $1/R_p$ term omitted in the admittance of the non-percolated circuit in Fig. 4.3(b). The inverse resistances $1/R_{p,NP}$ are naturally proportional to the real part of particle transient conductivity $\Delta\sigma^{\text{mic}}$, as opposed to the capacitance C_{NP} that is related only to the morphology of the sample and the permittivity of the matrix.

We do not seek specific relations between the quantities describing the circuit and the nanostructure. The definition of the admittance (4.2) serves us merely as the function pattern for our EMT – the relation between the microscopic and the effective conductivity. The total circuit admittance is analogous to the effective transient conductivity $\Delta\sigma$ of the represented structure:

$$\Delta\sigma = V\Delta\sigma^{\text{mic}} + \frac{B\Delta\sigma^{\text{mic}}}{1 + \frac{iD\Delta\sigma^{\text{mic}}}{\omega\varepsilon_0}}, \quad (4.3)$$

where V is the percolation strength of the photoconductive material (cf. Subsection 3.4.3). Note that, from now on, we simplify the notation $V \equiv V_p$ as we deal only with the *change* of the effective conductivity/permittivity. The constant percolation strength V_m of the dielectric matrix does not play a role in the change of the effective quantities and using V only for V_p is thus unambiguous. B and D constitute morphology parameters whose interpretation is discussed in the following subsections.

Equation (4.3) defines the VBD effective medium model in terms of complex conductivity. In order to fit it to the calculated effective transient permittivities, we convert it using the definition

$$\Delta\varepsilon = \frac{i\Delta\sigma}{\omega\varepsilon_0}; \quad \Delta\varepsilon_p = \frac{i\Delta\sigma^{\text{mic}}}{\omega\varepsilon_0} \quad (4.4)$$

to the probably briefest variant in terms of complex permittivity

$$\Delta\varepsilon = \Delta\varepsilon_p \left[V + \frac{B}{1 + D\Delta\varepsilon_p} \right]. \quad (4.5)$$

For purely imaginary $\Delta\varepsilon_p = i\Delta\varepsilon_p''$, the dependence is explicitly

$$\Delta\varepsilon' + i\Delta\varepsilon'' = \frac{DB\Delta\varepsilon_p''^2}{1 + (D\Delta\varepsilon_p'')^2} + i \left[V\Delta\varepsilon_p'' + \frac{B\Delta\varepsilon_p''}{1 + (D\Delta\varepsilon_p'')^2} \right]. \quad (4.6)$$

Equation (4.6) was found to fit the calculated $\Delta\varepsilon(\Delta\varepsilon_p'')$ dependences very well for all examined structures (see Fig. 4.4), except for the non-percolated direction of the most complex fractal ‘‘Moore 3’’. (See Section 4.6 below for comments on the

larger deviation between the simulations and our analytical model in that case.) This confirms that a set of only 3 parameters, V , B and D is sufficient to characterize the impact of morphology on the way in which the transient *microscopic* permittivity of nanoparticles translates into the transient *macroscopic* permittivity of the composite structure. In Section 4.5, we provide the interpretation of these fitting parameters within the framework of the Bergman EMT.

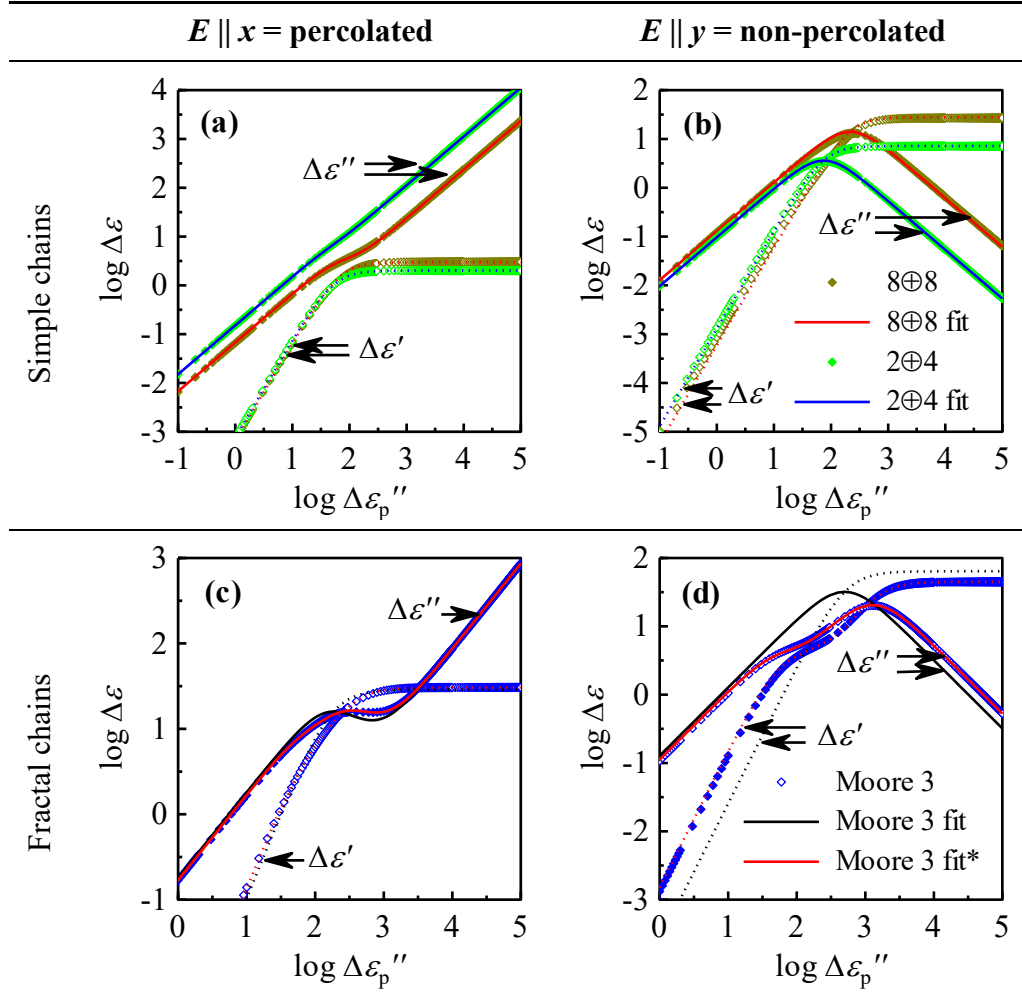


Fig. 4.4 *Symbols*: calculated $\Delta\epsilon(\Delta\epsilon_p'')$ dependences (selection of curves from Fig. 4.2); *lines*: fits with the VBD model. Color legend is the same for both plots on a row. *Red lines in (c,d): fit of the Moore 3 fractal chain with a two-component VBD model (two parallel RC branches are considered).

Let us explain the trends in Fig. 4.4 or Fig. 4.2 in terms of the VBD model (4.6). The response of *non-percolated* structures (panels (b,d) in both Figures) is characterized by the two fractions on the right hand side of (4.6):

- as long as $(D\Delta\epsilon_p'')^2 \ll 1$, the real effective permittivity $\Delta\epsilon'$ increases with the second power of $\Delta\epsilon_p''$ and the imaginary effective permittivity $\Delta\epsilon''$ is directly proportional to $\Delta\epsilon_p''$; this corresponds to specific slopes of the curves in the log-log scale in the Figures for small $\Delta\epsilon_p''$;

- for $(D\Delta\varepsilon_p'')^2 \gg 1$, $\Delta\varepsilon'$ saturates and $\Delta\varepsilon''$ is *inversely* proportional to $\Delta\varepsilon_p''$.

The position of the elbow of the curves in the Figures is characteristic for the RC resonance which will be interpreted also as the localized plasmon resonance of the non-percolated nanoparticles later on. (An additional bend appears in the mid-range in structures with increased fractal complexity.)

Percolated structures (panels (a,c) in the Figures) show a behavior similar to non-percolated ones in $\Delta\varepsilon'$ in the whole range, and also in $\Delta\varepsilon''$ for $(D\Delta\varepsilon_p'')^2 \ll 1$. The main difference to the non-percolated structures is marked with the additional $iV\Delta\varepsilon_p''$ term in (4.6), due to which:

- the imaginary part of transient effective permittivity $\Delta\varepsilon''$ continues to be *directly proportional* to $\Delta\varepsilon_p''$ also in the upper range, $(D\Delta\varepsilon_p'')^2 \gg 1$.

The sharp difference between the effective permittivity of percolated and non-percolated structures in the high- $(D\Delta\varepsilon_p'')^2$ regions constitutes a useful experimental marker for characterizing real samples in Optical pump–THz probe experiments as shown below.

4.3. Application of the VBD model in Optical pump–THz probe experiments

An OPTP experiment yields the transient effective conductivity $\Delta\sigma$ of the studied sample. For a correct interpretation of the results the relation between $\Delta\sigma$ and $\Delta\sigma^{\text{mic}}$ is of prime importance. In the previous paragraph we discussed the role of the threshold value of the imaginary part of the permittivity $(D\Delta\varepsilon_p'')^2 \approx 1$. In a similar manner, the discussion can be carried out for a complex microscopic conductivity which appears in (4.3). We are again interested in the threshold value of the denominator term $D\Delta\sigma^{\text{mic}}/(\omega\varepsilon_0) \approx 1$:

- for $|D\Delta\sigma^{\text{mic}}/(\omega\varepsilon_0)| \ll 1$, $\Delta\sigma$ is *proportional* to $\Delta\sigma^{\text{mic}}$ both in percolated and non-percolated structures;
- for $|D\Delta\sigma^{\text{mic}}/(\omega\varepsilon_0)| \geq 1$, $\Delta\sigma$ depends on $\Delta\sigma^{\text{mic}}$ in a complex *non-linear* manner in non-percolated structures; the linear proportionality $\Delta\sigma \propto \Delta\sigma^{\text{mic}}$ holds in percolated structures.

The amplitude of $D\Delta\sigma^{\text{mic}}/(\omega\varepsilon_0)$ can be easily varied in Optical pump–THz probe experiments because the transient microscopic conductivity $\Delta\sigma^{\text{mic}}$ scales with the photocarrier *density* — it can be controlled by the excitation *fluence* ϕ of the optical pump beam. A linear dependence of the measured effective response on ϕ means that the measured transient conductivity $\Delta\sigma$ spectrum has the shape of $\Delta\sigma^{\text{mic}}$ (i.e. of the microscopic *mobility* spectrum of photocarriers). A non-linear dependence of $\Delta\sigma$ on ϕ , directly indicates that a substantial portion of photocarriers is confined in non-percolated inclusions in the sample. These two regimes can be simply discerned in the plots of the transient transmittance per single excitation photon ΔT_{norm} (2.10): *any* dependence of ΔT_{norm} on ϕ indicates the non-linear regime.

In an ideal experimental case, the linear regime of a structure is achieved by decreasing the excitation fluence and the spectrum measured under these conditions yields the actual microscopic carrier conductivity spectrum $\Delta\sigma^{\text{mic}}$ (without the effect of depolarization fields). Subsequently, photoconductivity spectra measured over the widest possible range of higher excitation fluences show whether the structure exhibits the non-linear response (i.e. whether non-percolated inclusions contribute to the conductivity of the sample) or whether the response remains linear (i.e. the structure is percolated). Below, we provide an estimate of the photocarrier density that should be reached in order to distinguish between contributions from percolated and non-percolated parts. A global fit of the fluence dependent conductivity spectra of the sample then can be performed and the parameters V , B , D yielded by the fit can be linked to the morphological properties of the structure such as the filling fraction of the non-percolated inclusions or the representative depolarization factor of the structure. This procedure is extremely sensitive to:

- percolated parts of the structure, whose signal scales up with ϕ ;
- large inclusions in which the carrier mobility can be quite high and whose response exhibits strong non-linearity versus ϕ .

For example, in Chapter 6, OPTP spectroscopy discovered large inclusions with high carrier mobility at a particularly low filling fraction of 10^{-4} . These inclusions were not detectable by other employed techniques due to their low concentration.

Kužel and Němec [45] have derived an estimate of carrier density in typical non-percolated inclusions ($D \sim 10^{-2}$) that brings about a transition between the linear and the non-linear regime in the THz range as:

$$N(\text{cm}^{-3}) \approx 10^{18} \frac{\nu(\text{THz})}{\mu(\text{cm}^2 \text{V}^{-1} \text{s}^{-1})}. \quad (4.7)$$

We stress that the transition region is several orders of magnitude wide (cf. Fig. 4.4) and the value of 10^{18} presents an order of magnitude estimate. Specific morphologies with high capacitances (e.g. containing field-parallel semiconducting chains separated with thin sheets of the matrix) are characterized with a lower D (D in (4.3) is in inverse position to C_{NP} in (4.2)). The response of such structures can thus be measured in the linear (mobility-like) regime at higher carrier concentrations than indicated by (4.7). High-mobility materials, on the other hand, require lower densities to measure the true carrier mobility spectral shape. Obtaining linear response above the estimated threshold density means that the material does not contain a substantial portion of non-percolated inclusions with the expected mobility and morphology D factor.

Fig. 4.5 shows the behavior of a THz spectrum in non-percolated inclusions with Drude type of mobility upon a change of the carrier density. At low carrier densities (red squares), the transient photoconductivity spectrum still resembles Drude response with a decreasing real part and a peaking positive imaginary part.

With increasing carrier density, the conductivity peak decreases and blueshifts and the imaginary part flips to negative values in the accessible frequency range. This resonant behavior can be understood also as the signature of the localized plasmon in photoconductive inclusions.

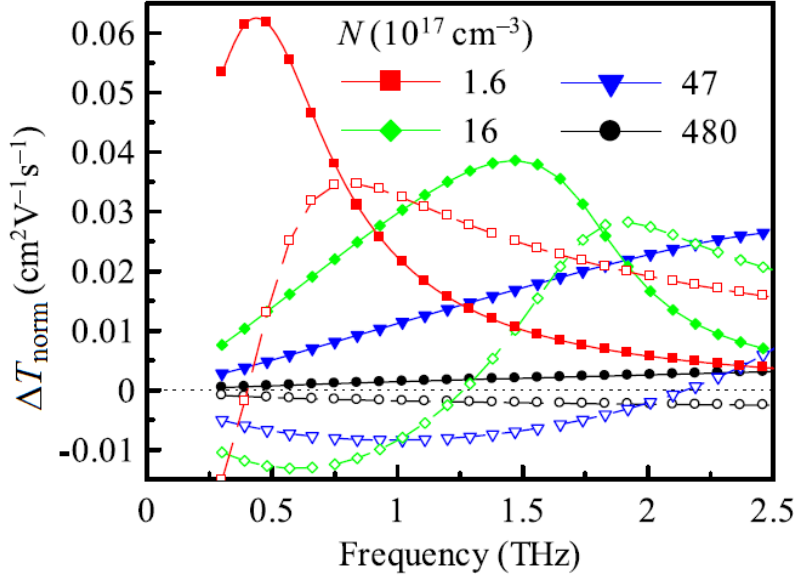


(Fig. 5(b) in [4], notation adapted)

Fig. 4.5 Theoretical spectra of normalized transient transmittance of a model non-percolated thin film sample with Drude mobility spectrum at various excitation densities; *full symbols*: real part, *empty symbols*: imaginary part. The displayed frequency range is typical to time-domain THz spectroscopic setups with ZnTe sensor. The input properties of the model nanostructure correspond to sample A in Chapter 6 at 20 K.

4.4. Interpretation in terms of the Maxwell Garnett EMT

In the case of a composite with well isolated particles described with a single shape factor K , our model (4.5) reduces exactly to the Maxwell Garnett EMT as introduced in Subsection 3.4.1 with the parameters defined by the ground state properties of the composite

$$V = 0, \quad (4.8)$$

$$B = \frac{\varepsilon_m(1 + sK) - \varepsilon(1 - s)}{\varepsilon_m(s + K) + \varepsilon_p(1 - s)}, \quad (4.9)$$

$$D = \frac{(1 - s)}{\varepsilon_m(s + K) + \varepsilon_p(1 - s)}, \quad (4.10)$$

where ε is here the ground state effective permittivity of the composite in the Maxwell Garnett approximation (3.15).

4.5. Relation to the Bergman EMT

The effective permittivity in Bergman EMT was introduced in Subsection 3.4.3 as:

$$\varepsilon = V_m \varepsilon_m + V_p \varepsilon_p + \int_0^1 \frac{\nu(l) \varepsilon_m \varepsilon_p}{l \varepsilon_p + (1-l) \varepsilon_m} dl. \quad (3.21)$$

The integrand in (3.21) has in fact the form of the total capacitance of two planar capacitors with permittivities ε_p and ε_m , thicknesses $(1-d)$ and d , respectively, and of the same area A , connected *in series*:

$$C_{\text{series}}(d) = \left(\left(\varepsilon_p \frac{A}{1-d} \right)^{-1} + \left(\varepsilon_m \frac{A}{d} \right)^{-1} \right)^{-1} = \frac{A \varepsilon_m \varepsilon_p}{d \varepsilon_p + (1-d) \varepsilon_m}. \quad (4.11)$$

In this view, the depolarization factor l in the Bergman EMT is related to the relative thickness of the dielectric matrix and of the photoconductive material along the field. Integration over l in (3.21) is equivalent to summing up the total capacitance of capacitors $C_{\text{series}}(d)$ with various thickness ratios that are connected *in parallel* — the weighing function $\nu(l)$ then has the meaning of the effective cross-section of the morphology subpattern with a given depolarization factor. The Bergman EMT thus virtually describes an electric circuit with an infinite number of parallel RC branches with different values of R_{np} and C_{np} and the analogy to an equivalent electric circuit (cf. Fig. 4.3) is very pertinent.

We have found that, up to a certain level of complexity, many two-component structures can be approximated by a single dominant RC branch (cf. fits in Fig. 4.4), i.e. by a single δ -peak in $\nu(l)$ at a “representative” depolarization factor A in the Bergman spectral function with an amplitude v :

$$\nu(l) \approx v \delta(l - A) \quad (4.12)$$

The Bergman transient permittivity then reads:

$$\Delta \varepsilon = V \Delta \varepsilon_p + \frac{v \varepsilon_m (\varepsilon_p + \Delta \varepsilon_p)}{A (\varepsilon_p + \Delta \varepsilon_p) + (1-A) \varepsilon_m} - \frac{v \varepsilon_m \varepsilon_p}{A \varepsilon_p + (1-A) \varepsilon_m}, \quad (4.13)$$

which is identical to our VBD formula (4.5) with the following relations between B , D and v , A :

$$B = \frac{(1-A) \varepsilon_m^2 v}{[A \varepsilon_p + (1-A) \varepsilon_m]^2}, \quad (4.14)$$

$$D = \frac{A}{A\varepsilon_p + (1-A)\varepsilon_m}. \quad (4.15)$$

The value of D obtained from a fit of experimental data as proposed in Section 4.3 thus yields the representative depolarization factor of the structure

$$A = \frac{1}{1 + \frac{D\varepsilon_p}{1 - D\varepsilon_p}}. \quad (4.16)$$

4.5.1. Spectral function analysis

To study the meaning of A , we reconstructed the Bergman spectral functions of the model structures. The reconstruction (reproduction of values of $v(l)$ for every $0 < l < 1$) can be done by analyzing the Bergman EMT formula. A localized plasmon resonance corresponds to a pole in the denominator of the integrand in (3.21)

$$l\varepsilon_p + (1-l)\varepsilon_m = 0, \quad (4.17)$$

i.e., for a given l , one can find a real negative $\varepsilon_p \in (-\infty; 0)$ which provides the resonance. Using the residual theorem and analogously to [66,97], one can evaluate the spectral function using the limit

$$v(l) = -\frac{1}{\pi(1-l)} \lim_{\delta \rightarrow 0} \left[\text{Im} \left(1 - \frac{\varepsilon(\varepsilon_m, \tilde{\varepsilon}_p)}{\varepsilon_m} \right) \right], \quad (4.18)$$

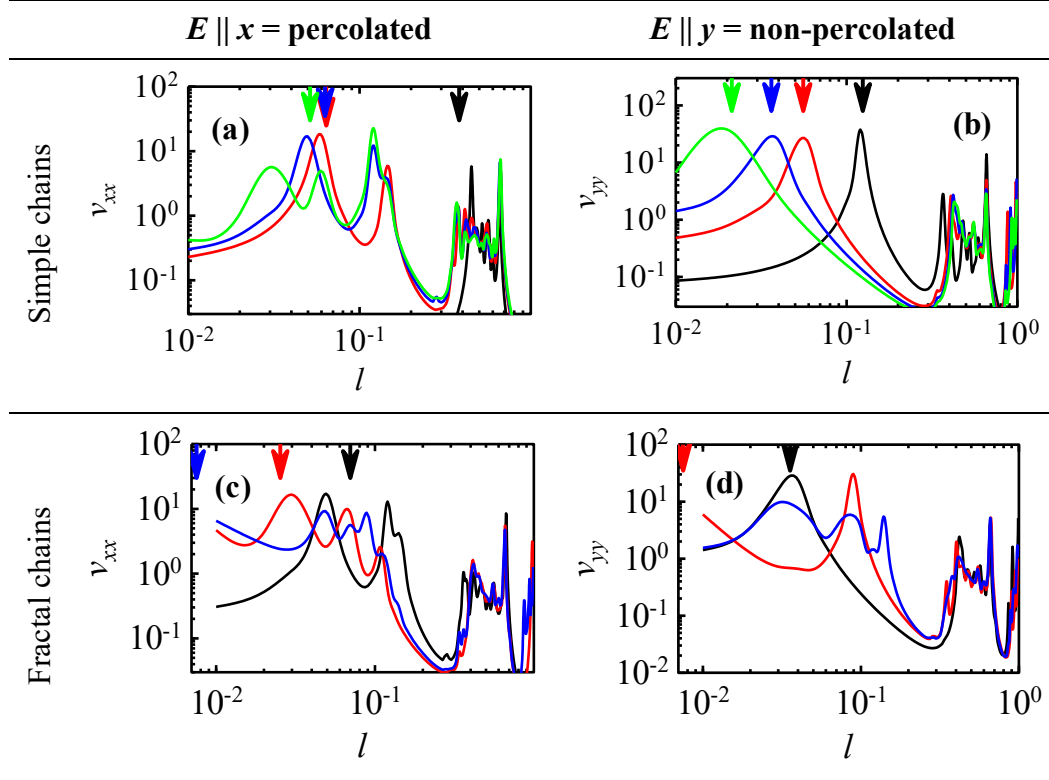
where the complex $\tilde{\varepsilon}_p$ is chosen near the resonance (4.17) such that

$$\left(\frac{\tilde{\varepsilon}_p}{\varepsilon_m} - 1 \right)^{-1} = -(l + i\delta). \quad (4.19)$$

The effective permittivity $\varepsilon(\varepsilon_m, \tilde{\varepsilon}_p)$ with the particle permittivity $\tilde{\varepsilon}_p$ for a given structure is again calculated numerically following (4.1) and the value of the spectral function (4.18) is then evaluated with a very small positive value of δ ($\delta = 0.005$ in our calculations).

Fig. 4.6 shows the calculated spectral functions of several structures. The vertical arrows above the spectral functions indicate the representative depolarization factor A as calculated through (4.16) from the value of D that provided the best fit of the effective permittivity with the VBD model (4.6) in each structure. Note that A coincides with the global maximum of the spectral function in non-percolated structures (second row in Fig. 4.6). In these cases, A bears the meaning of the depolarization factor that is dominant in the spectral function. This is not exactly true in structures with a percolation pathway — e.g. the green curve in Fig. 4.6(a) features a maximum at $l = 0.12$, far from the green arrow at $A = 0.05$. Instead, the representative depolarization factor falls to the peak or the group of peaks that lies at the *lowest* l in the spectral function. This means that morphological features with

lower depolarization factors play a more important role in determining the effective response of the composite than the morphological features with high depolarization factors in a broad range of particle permittivities. Let us remind that low depolarization factors correspond either to percolation pathways ($A=0$ for infinite wires parallel to the field) or, for example, to field-parallel chains of particles separated by narrow gaps. High depolarization factors, on the other hand, characterize isolated inclusions or thin field-perpendicular disks and layers.



(selection from Fig. 2. in [97], notation adapted)

Fig. 4.6 *Lines*: Reconstructed Bergman spectral functions of the model structures. *Vertical arrows*: Fitted values of representative depolarization factors A . Color scheme and panel labelling is identical to that in Fig. 4.2.

4.6. General character and limitations of the VBD effective medium model

The VBD model of effective medium response was explicitly confirmed by application of the numerical calculations of the macroscopic permittivity of composites with a purely imaginary particle permittivity contribution $\Delta\epsilon_p''$. The VBD model (4.3,4.5) is nevertheless valid for any complex-valued particle permittivity contribution, as long as the total particle permittivity $\epsilon_p + \Delta\epsilon_p$ stays positive. In this case, the integral in the Bergman representation of the structure avoids poles and no qualitatively new behavior is expected in comparison to the effective permittivities shown in Fig. 4.2. Bringing a semiconductor nanomaterial out of this regime, i.e. to a completely metallic behavior, by photoexcitation is seldom achievable. It would be

possible for example in high-mobility semiconductor structures (nanoislands, nanowires, nanotubes, etc.) under very strong excitation.

The simple variant of the VBD model, stemming from the admittance of an equivalent electric circuit model with only one conductive and one capacitive branch, proved to be adequate for reproducing the effective properties of a wide range of morphologies. However, thanks to the additive character of the formulas (4.3,4.5), it can be straightforwardly extended to more complex composites containing several types of inclusions with different transient permittivities $\Delta\varepsilon_j$ (transient microscopic conductivities $\Delta\sigma_j^{\text{mic}}$), percolation strengths V_j and morphology factors B_j , D_j , corresponding to an equivalent electric circuit with multiple parallel branches:

$$\Delta\varepsilon = \sum_j \Delta\varepsilon_j \left[V_j + \frac{B_j}{1 + D_j \Delta\varepsilon_j} \right], \quad (4.20)$$

$$\Delta\sigma = \sum_j \Delta\sigma_j^{\text{mic}} \left[V_j + \frac{B_j}{1 + \frac{iD_j \Delta\sigma_j^{\text{mic}}}{\omega\varepsilon_0}} \right]. \quad (4.21)$$

Namely, in the case of the most complex non-percolated fractal structures (Moore 3 in Fig. 4.1), the calculated dependences of effective permittivity (blue lines in Fig. 4.4(c,d)) cannot be reproduced with the simple 3-parameter VBD model both in the high- and low- $\Delta\varepsilon_p''$ regions at the same time (black lines in Fig. 4.4(c,d)). Red lines in Fig. 4.4(c,d) show excellent fits with the two-component variant of the VBD model (eq. (4.20) with $j = 1, 2$). The two-component VBD model was reduced in this case to one type of semiconductor in both photoconductive components ($\Delta\varepsilon_1 = \Delta\varepsilon_2 \equiv \Delta\varepsilon_p''$), naturally with a single percolation strength V_1 ($V_2 \equiv 0$) and two pairs of morphology parameters B_1, D_1 and B_2, D_2 .

Another reduced variant of the two-component VBD model is applicable in samples containing both very small and relatively large* photoconductive particles of one semiconductor. Such structures are obtained e.g. after chemical or thermal aggregation of small precursor nanoparticles, which is a relatively frequent production procedure. The Monte Carlo simulations of our group (Section 3.5) showed that the carrier mobility spectrum (and thus also the transient contribution $\Delta\sigma^{\text{mic}}$ to the *microscopic* conductivity) may be sharply different inside the small isolated particles and inside large interconnected clusters or percolation chains made of the same material (same ground state permittivity ε_p). In a sample containing particles in both these regimes, the contribution to the transient effective conductivity

* By small or large we mean here that the characteristic size of the particle is comparable to or much larger than l_{free} , respectively, cf. Fig. 3.4.

is $B/[1 + iD\Delta\sigma_{\text{non-perc}}^{\text{mic}}/\omega\varepsilon_0]$ for the non-percolated component and $V\Delta\sigma_{\text{perc}}^{\text{mic}}$ for the percolated one. The transient effective conductivity in the VBD approximation then reads

$$\Delta\sigma = V\Delta\sigma_{\text{perc}}^{\text{mic}} + \frac{B\Delta\sigma_{\text{non-perc}}^{\text{mic}}}{1 + \frac{iD\Delta\sigma_{\text{non-perc}}^{\text{mic}}}{\omega\varepsilon_0}}. \quad (4.22)$$

This is again the point where the localization of mobile carriers in nanoparticles of a semiconducting material has a two-level impact: the conductivity of the semiconducting material is altered on the short-range — it takes the microscopic spectrum $\Delta\sigma_{\text{non-perc}}^{\text{mic}}$ due to the interactions of *individual* carriers with boundaries of small particles — and this spectrum is further modified in the *collective* carrier THz response due to depolarization fields originating in the macroscopic (long-range) morphology of these particles.

5. Wave equation solution — measurable vs. local conductivity

In this chapter we derive the theoretical measurable transient THz transmittance spectrum $\Delta T_{\text{norm}}(\omega)$ of a semiconducting nanomaterial and the relation of this quantity to the microscopic conductivity of its constituents in the framework of the VBD effective medium theory. Our approach is based on the linearization of the wave equation for a THz probe pulse (respectively for its transient part) that was introduced in 2002 [99] and revised in 2007 [42]. These publications deal with homogeneous (or layered) media and focus on the retrieval of ultrafast (sub-ps) dynamics from transient THz response. Our aim here is to generalize this approach for nano- or microstructured media with or without percolation pathways. We restrict our attention to the phenomena which occur on the time scale longer than the THz pulse length, i. e. \sim ps or slower (the quasi-steady-state approximation, cf. Section 2.3).

We first review the wave equation for the transient THz field and its boundary conditions. Subsequently, we solve the wave equation in terms of $\Delta T_{\text{norm}}(\omega)$, which represents the transmitted transient THz field, both in the case of percolated and non-percolated (nano)structures and discuss some experimentally useful approximations. These results are used for the interpretation of our experimental results obtained with Si nanostructures in Chapters 6, 7. Lastly, we show the general solution of the wave as the starting point for the cases that are not covered by the VBD approximation. This general solution is utilized in Chapter 8 for bulk TiO₂ that features electron–hole scattering upon strong excitation. The results were partly published in [4] and [97] and summarized in a review paper [45].

5.1. Transient THz wave equation

The wave equation for the transient THz field ΔE (2.3) was mentioned in Section 2.3 along with its right-hand side source term (2.4). Put into one equation, they read:

$$\frac{d^2 \Delta E(\omega, z)}{dz^2} + n(\omega)^2 k_0^2 \Delta E(\omega, z) = -ik_0 Z_0 \Delta \sigma(\omega, z) E(\omega, z) \equiv U(\omega, z). \quad (5.1)$$

The THz field in the sample E together with the effective transient conductivity $\Delta \sigma$ on the right-hand side of (5.1) constitute a transient current $\Delta j = \Delta \sigma \cdot E$ which emits the transient THz field ΔE . The driving THz field is the sum of the primary probe field E_{probe} and of the transient field: $E = E_{\text{probe}} + \Delta E$. The main assumption of this model is that $\Delta E \ll E_{\text{probe}}$ and $E(\omega, z)$ can be replaced by $E_{\text{probe}}(\omega, z)$. The wave equation is then linear and its solutions can be found analytically. [42]* The

* This linearization also justifies using of equilibrium refractive index $n(\omega)$ without a transient contribution of $\Delta \sigma$ on the left-hand sides in (2.3), (5.1) and further.

distribution of the primary probe field in the sample of thickness L can be calculated from the incident field E_{inc} :

$$E_{\text{probe}}(\omega, z) = E_{\text{inc}}(\omega) t_1 a [\exp(ikz) + r_2 \exp(-ik(z - 2L))], \quad (5.2)$$

where $k = k_0 n(\omega)$ is the wavenumber of the THz wave in the unexcited sample and

$$a = \sum_{j=0}^{\infty} [r_1 r_2 \exp(2ikL)]^j = [1 - r_1 r_2 \exp(2ikL)]^{-1} \quad (5.3)$$

is the sum accounting for Fabry-Perot reflections of the THz probe pulse in the sample. The transmission coefficients through the front (index 1) and rear (index 2) interface of the sample $t_{1,2}$ and the internal reflection coefficients for the normal incidence $r_{1,2}$ are given by the Fresnel equations where refractive indices n_1 and n_2 of the media surrounding the photoconductive layer are introduced:

$$\begin{aligned} t_1 &= \frac{2n_1}{n + n_1}, & t_2 &= \frac{2n}{n + n_2}; \\ r_1 &= \frac{n - n_1}{n + n_1}, & r_2 &= \frac{n - n_2}{n + n_2}. \end{aligned} \quad (5.4)$$

The first summand in the square brackets in (5.2) represents the forward propagation of the THz pulse through the sample and the second term stands for its backward propagation after being reflected from the sample rear surface.

The solution of the Equation (5.1) is found as a linear combination

$$\Delta E(z) = A_1 \exp(-ikz) + A_2 \exp(ikz) + G(z), \quad (5.5)$$

where $A_{1,2}$ are the factors of the homogeneous solution and $G(z)$ is the particular solution with the given right-hand side. The formula for the transmitted transient field $\Delta E_t(\omega)$ is obtained by applying the proper boundary conditions — i.e. the continuity of the tangential components of the electric and magnetic field at the front and the rear surfaces of the sample. The intensity of the transient magnetic field is proportional to the space derivative of the electric field:

$$\Delta H = -\frac{i}{\mu_0 \omega} \frac{d\Delta E}{dz} \quad (5.6)$$

with μ_0 being the vacuum permeability. The boundary conditions for the electric intensity then can be formulated as follows [42]:

$$\begin{aligned} \Delta E_r &= \Delta E(z = 0), & n_1 k_0 \Delta E_r &= i \left. \frac{d\Delta E}{dz} \right|_{z=0}, \\ \Delta E_t &= \Delta E(z = L), & -n_2 k_0 \Delta E_t &= i \left. \frac{d\Delta E}{dz} \right|_{z=L}, \end{aligned} \quad (5.7)$$

where ΔE_r is the transient electric field emitted from the sample in the backward direction (measurable optionally as the transient change of the probe field reflected from the sample in an experiment arranged in the reflection geometry). The derived

transmitted transient field ΔE_t then only needs to be compared to the reference field transmitted through the sample in equilibrium, which is simply

$$E_t(\omega) = t_1 t_2 a \exp(ikL) E_{\text{inc}}(\omega). \quad (5.8)$$

One thus obtains the theoretical transient transmittance (2.5) (or its normalized form (2.10)) of the model photoconductivity $\Delta\sigma(\omega, z)$ that was injected into the right hand side of the wave equation (5.1). The model conductivity may consist of several additive contributions originating in different types of photoconductive elements in the sample. These conductivity components translate linearly into the transient transmittance thanks to the linearity of the wave equation. In the following sections, we derive the solutions of the wave equations for the effective photoconductivity separately for a sample with percolated photoconductive pathways and for a sample with non-percolated photoconductive inclusions. Below we introduce a notation which is common to these two cases.

The microscopic transient conductivity is proportional to the density and mobility of the carriers inside the inclusions. With a negligible dependence of the mobility of a single carrier on the carrier density, the microscopic transient conductivity takes on a variable-separated form

$$\Delta\sigma^{\text{mic}}(\omega, z) = eN(z)\mu(\omega) \quad (5.9)$$

The photocarrier density in the semiconductor (nano)particles is proportional to the excitation fluence, the local absorption coefficient of the inclusions α^{mic} and decays with depth according to the macroscopic (effective) absorption coefficient α of the sample:

$$N(z) = \alpha^{\text{mic}} \phi \zeta \exp(-\alpha z) \equiv N_0^{\text{mic}} \exp(-\alpha z). \quad (5.10)$$

Where we abbreviated the photocarrier density in the particles at the photoexcited surface as N_0^{mic} . To shorten the following formulas, we introduce the transient *microscopic* conductivity spectrum at the surface of the sample $\Delta\sigma_0^{\text{mic}}(\omega)$ as:

$$\begin{aligned} \Delta\sigma^{\text{mic}}(\omega, z) &= e N_0^{\text{mic}} \mu(\omega) \exp(-\alpha z) \\ &\equiv \Delta\sigma_0^{\text{mic}}(\omega) \exp(-\alpha z). \end{aligned} \quad (5.11)$$

(Note that $\Delta\sigma_0^{\text{mic}}$ was denoted $\Delta\sigma_0$ in [45]. We keep the superscript ‘‘mic’’ in this work to stress that the quantity has the microscopic character and has the spectral shape of charge carrier mobility.)

5.2. Percolated semiconducting pathways and bulk samples

In nanomaterials where the semiconductor forms percolated pathways, the macroscopic photoconductivity is just the microscopic one multiplied by the percolation strength:

$$\Delta\sigma^{\text{perc}}(\omega, z) = V \Delta\sigma_0^{\text{mic}}(\omega) \exp(-\alpha z). \quad (5.12)$$

The source term of the wave equation (5.1) is then

$$U(\omega, z) = -ik_0 Z_0 \cdot V \Delta \sigma_0^{\text{mic}}(\omega) \exp(-\alpha z) E_{\text{probe}}(\omega, z) \quad (5.13)$$

and the particular solution reads

$$G(z) = -ik_0 Z_0 \cdot V \Delta \sigma_0^{\text{mic}}(\omega) \frac{\exp(-\alpha z)}{\alpha^2} E_{\text{probe}}(\omega, z). \quad (5.14)$$

Applying the boundary conditions (5.7) yields the transient transmitted field

$$\begin{aligned} \Delta E_t(\omega) = & -\frac{1}{n_2 + n} Z_0 \cdot \frac{V \Delta \sigma_0^{\text{mic}}(\omega)}{\alpha} E_{\text{inc}}(\omega) t_1 a^2 \exp(ikL) \\ & \times \left\{ (1 + r_1 r_2 \exp(2ikL)) [1 - \exp(-\alpha L)] \right. \\ & \left. + r_1 \frac{1 - \exp(2ikL) \exp(-\alpha L)}{1 - 2ik/\alpha} + r_2 \frac{\exp(2ikL) - \exp(-\alpha L)}{1 + 2ik/\alpha} \right\}. \end{aligned} \quad (5.15)$$

The general contribution of percolated semiconducting elements to the normalized transient transmittance (2.10) with the reference field (5.8) is then

$$\begin{aligned} \Delta T_{\text{norm}}^{\text{perc}}(\omega) = & \frac{n_1 + n_2}{2n} \cdot V \frac{\Delta \sigma_0^{\text{mic}}(\omega)}{e\alpha\phi} a \\ & \times \left\{ (1 + r_1 r_2 \exp(2ikL)) (1 - \exp(-\alpha L)) \right. \\ & \left. + r_1 \frac{1 - \exp(2ikL) \exp(-\alpha L)}{1 - 2ik/\alpha} + r_2 \frac{\exp(2ikL) - \exp(-\alpha L)}{1 + 2ik/\alpha} \right\}. \end{aligned} \quad (5.16)$$

Let us remind that according to (5.10,5.11):

$$\Delta \sigma_0^{\text{mic}}(\omega) = e\alpha^{\text{mic}} \phi \zeta \mu(\omega), \quad (5.17)$$

i.e. ϕ cancels out

$$\Delta T_{\text{norm}}^{\text{perc}}(\omega) = \frac{n_1 + n_2}{2n} \cdot V \frac{\Delta \sigma_0^{\text{mic}}(\omega)}{e\alpha\phi} a \times \{ \dots \} \propto \frac{n_1 + n_2}{2n} \cdot \frac{\alpha^{\text{mic}}}{\alpha} V \zeta \mu(\omega) \quad (5.18)$$

and the *normalized* transient transmittance spectrum of percolated components (5.16) retains the shape of the carrier mobility spectrum and does not depend on excitation density in most experimental cases. This is not exactly true only when n , n_1 or n_2 exhibit a substantial dispersion in the THz range or with a specific combination of THz optical thickness and pump light absorption coefficient. In the latter case, additional modulation may occur in the spectra due to Fabry-Pérot interferences of the primary or transient THz field, as described by the term a or the term in the curly brackets in (5.16). These terms depend on the THz wave vector only and not on the microscopic conductivity; thus the true interpretation of the THz spectra cannot be missed if their analysis is carefully carried out.

For *bulk* samples, one trivially finds that $V \equiv 1$ and $\alpha^{\text{mic}} \equiv \alpha$. In the following, we review several analytical limits of (5.16) that will be applied in the experimental chapters.

5.2.1. Thin samples

In the case of a thin sample ($kL \ll 1$), all $\exp(2ikL)$ terms tend to 1 and the normalized transient transmittance condenses to:

$$\Delta T_{\text{norm}}^{\text{perc}}(\omega) = V \frac{\alpha^{\text{mic}}}{\alpha} \xi \mu(\omega) \cdot [1 - \exp(-\alpha L)]. \quad (5.19)$$

In the case of strong absorption of the optical pump pulse $1 \ll \alpha L$

$$\Delta T_{\text{norm}}^{\text{perc}}(\omega) = V \frac{\alpha^{\text{mic}}}{\alpha} \xi \mu(\omega), \quad (5.20)$$

while in the case of weak absorption $\alpha L \ll 1$

$$\Delta T_{\text{norm}}^{\text{perc}}(\omega) = V \alpha^{\text{mic}} L \xi \mu(\omega). \quad (5.21)$$

It is clearly seen that the *measurable* spectrum $\Delta T_{\text{norm}}(\omega)$ has directly the shape the photocarrier *mobility spectrum* in the three cases above.

5.2.2. Thick samples

With a thick sample ($kL \gg 1$), the direct pass of the THz probe pulse is well separated in time from Fabry-Pérot echoes. The time-domain windowing of the signal then can be applied experimentally [37]. In our calculations, the time-domain windowing means that the terms with the phase larger than $2ikL$ are omitted from the wave equation solution (5.16):

$$\Delta T_{\text{norm}}^{\text{perc}}(\omega) = \frac{n_1 + n_2}{2n} V \frac{\alpha^{\text{mic}}}{\alpha} \xi \mu(\omega) \left\{ 1 - \exp(-\alpha L) + \frac{r_1}{1 - 2ik/\alpha} - \frac{r_2 \exp(-\alpha L)}{1 + 2ik/\alpha} \right\}. \quad (5.22)$$

Under conditions of strong optical absorption ($1 \ll \alpha L$), the normalized transient transmittance of percolated components reads

$$\Delta T_{\text{norm}}^{\text{perc}}(\omega) = \frac{n_1 + n_2}{n + n_1} V \frac{\alpha^{\text{mic}}}{\alpha} \xi \mu(\omega). \quad (5.23)$$

5.3. Non-percolated semiconductor inclusions

Let us remind the contribution of non-percolated semiconducting particles to the macroscopic conductivity in the VBD approximation (4.22):

$$\Delta \sigma^{\text{non-perc}}(\omega, z) = \frac{B \Delta \sigma^{\text{mic}}(\omega, z)}{1 + \frac{iD \Delta \sigma^{\text{mic}}(\omega, z)}{\omega \epsilon_0}}. \quad (5.24)$$

In Optical pump–THz probe experiments, photocarrier density decreases exponentially from the photoexcited surface of the sample at $z = 0$. We first comment on the specific depth-profile of $\Delta\sigma^{\text{non-perc}}$ in this case because it somewhat clarifies the relatively complex solution of the corresponding wave equation that we derive subsequently.

5.3.1. Depth-profile of effective conductivity

We already pointed out that the macroscopic conductivity (5.24) is proportional to the microscopic one for low microscopic conductivity values and that it saturates with increasing microscopic conductivity. With the transient microscopic conductivity decreasing exponentially below the photoexcited surface (5.11), the saturation effect translates into a non-exponential depth profile of the effective conductivity:

$$\Delta\sigma^{\text{non-perc}}(\omega, z) = \frac{B\Delta\sigma_0^{\text{mic}}(\omega)\exp(-\alpha z)}{1 + \frac{iD\Delta\sigma_0^{\text{mic}}(\omega)}{\omega\epsilon_0}\exp(-\alpha z)}. \quad (5.25)$$

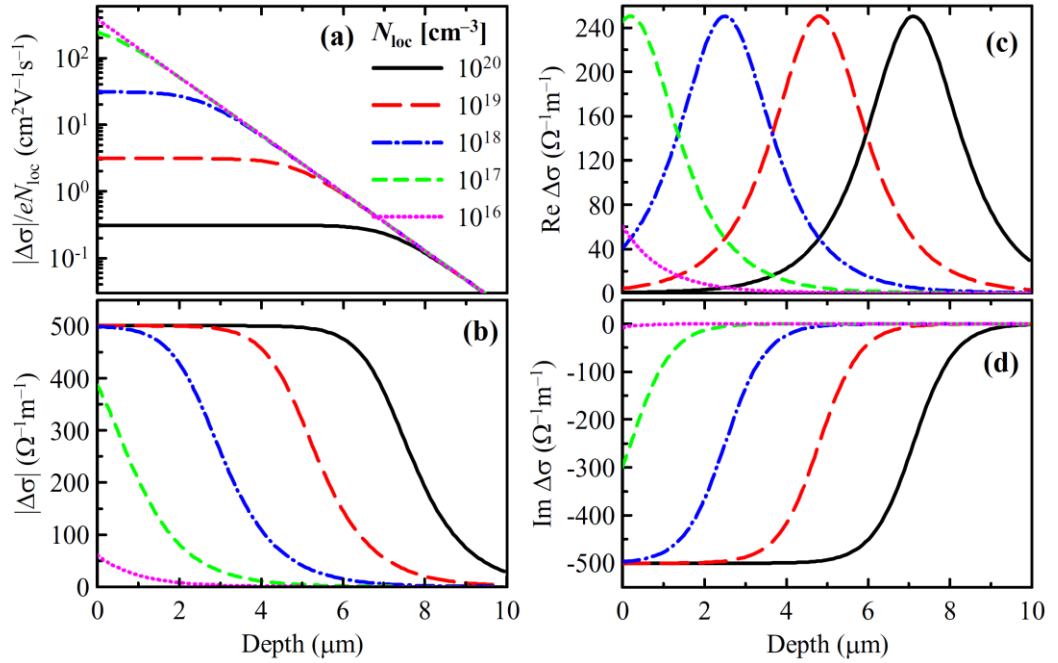


(Fig. 2. in [45])

Fig. 5.1 Depth profiles of transient effective conductivity in the VBD approximation (5.24) in a model non-percolated semiconducting structure with the usual exponential microscopic conductivity profile due to the Lambert-Beer absorption law (5.11) with $\xi = 1$, $\mu = 1350 \text{ cm}^2\text{V}^{-1}\text{s}^{-1}$, $1/\alpha = 1 \text{ }\mu\text{m}$, $V = 0$, $B = 0.28$ and $D = 0.031$ at various densities at 1 THz, $B\omega\epsilon_0/D = 502 \text{ }\Omega^{-1}\text{m}^{-1}$: (a) magnitude per single charge carrier (= mobility), (b) magnitude, (c) real part and (d) imaginary part.

At low excitation densities, the effective conductivity linearly follows the exponential depth profile of the carrier density (magenta lines in all panels in Fig. 5.1). For higher excitation densities (other colors in Fig. 5.1), the macroscopic conductivity retains the linear regime (and follows the exponential depth-profile of excitation) only in deep layers of the sample, where the intensity of the excitation light is decreased by absorption and the microscopic conductivity is low enough. The frontmost layer of a strongly excited sample exhibits a capacitive effective conductivity saturated at the value $-iB\omega\varepsilon_0/D$ (Fig. 5.1(b)) that is given only by the morphology factors, i.e. the capacitive properties of the insulating matrix. The intermediate region presents a transient resistive layer that features a peak of the real part of effective transient conductivity as shown in Fig. 5.1(c).

5.3.2. Solution of the wave equation in non-percolated case

The source term of the wave equation (5.1) in non-percolated samples with exponential excitation depth profile is

$$U(\omega, z) = -ik_0 Z_0 \frac{B\Delta\sigma_0^{\text{mic}}(\omega)\exp(-az)}{1 + \frac{D\Delta\sigma_0^{\text{mic}}(\omega)}{i\omega\varepsilon_0}\exp(-az)} E_{\text{probe}}(\omega, z) \quad (5.26)$$

To abbreviate notation, we condense what is analogous to the capacitive impedance spectrum of the RC branch in the equivalent electric circuit in the VBD theory (4.2):

$$Z(\omega, z) \equiv \frac{iD\Delta\sigma_0^{\text{mic}}(\omega)}{\omega\varepsilon_0} \exp(-az). \quad (5.27)$$

The solution of the wave equation with the (5.26) right-hand side is found in terms of the following integrals

$$\int \frac{\exp(-az)}{1 + Z(0)\exp(-az)} dz = -\frac{\text{Ln}[1 + Z(0)\exp(-az)]}{\alpha Z(0)}, \quad (5.28)$$

where Ln stands for the principal value of the logarithm function, and

$$\begin{aligned} & \int \frac{\exp[(2ik - \alpha)z]}{1 + Z(0)\exp(-az)} dz = \\ & = -\frac{\exp[(2ik - \alpha)z]}{-2ik + \alpha} {}_2F_1\left(1; 1 - \frac{2ik}{\alpha}; 2 - \frac{2ik}{\alpha}; -Z(0)\exp(-az)\right), \end{aligned} \quad (5.29)$$

where ${}_2F_1$ is the Gaussian hypergeometric function of 4 complex arguments. [100]

For our specific bonds between the arguments, we can define a 2-argument function

$$F(\kappa, Z) = \frac{{}_2F_1(1, \kappa, 1 + \kappa, -Z)}{\kappa}, \quad (5.30)$$

with $\kappa = 1 - 2ik/\alpha$. This specific variant of the hypergeometric function can be expressed as the power expansion

$$F(\kappa, Z) = \sum_{j=0}^{\infty} \frac{(-Z)^j}{\kappa + j} \quad (5.31)$$

for $|Z| < 1$ (Statement 15.1.1 in [100]), and

$$F(\kappa, Z) = \sum_{j=0}^{\infty} \frac{(-Z)^{-(j+1)}}{1 - \kappa + j} + \frac{\Gamma(1 - \kappa) \Gamma(1 + \kappa)}{\kappa} \exp[-\kappa \cdot \text{Ln}(-Z)] \quad (5.32)$$

for $|Z| > 1$ (Statement 15.3.7 in [100]).

The particular solution of the wave equation for the right-hand side given by (5.26) is then

$$\begin{aligned} G(z) = & \frac{1}{2n} Z_0 B \Delta \sigma_0^{\text{mic}}(\omega) E_{\text{inc}}(\omega) t_1 \frac{a}{\alpha} \\ & \times \left\{ \left[\frac{\text{Ln}(1 + Z(\omega, z))}{Z(\omega, 0)} - \exp(-az) \cdot F(\kappa, Z(\omega, z)) \right] \exp(ikz) \right. \\ & \left. - r_2 \left[\frac{\text{Ln}[1 + Z(\omega, z)]}{Z(\omega, 0)} - \exp(-az) \cdot F(\kappa^*, Z(\omega, z)) \right] \exp(-ik(z - 2L)) \right\}, \end{aligned} \quad (5.33)$$

where κ^* denotes the complex conjugate of κ . Applying the boundary conditions (5.7) yields the transient transmitted field

$$\begin{aligned} \Delta E_t = & -\frac{1}{n + n_2} Z_0 B \frac{\Delta \sigma_0^{\text{mic}}(\omega)}{\alpha} E_{\text{inc}} a^2 t_1 \exp(ikL) \\ & \times \left\{ [1 + r_1 r_2 \exp(2ikL)] \left[\frac{\text{Ln}(1 + Z(\omega, 0)) - \text{Ln}(1 + Z(\omega, L))}{Z(\omega, 0)} \right] \right. \\ & + r_1 [F(\kappa, Z(\omega, 0)) - \exp(2ikL) \exp(-\alpha L) F(\kappa, Z(\omega, L))] \\ & \left. + r_2 [F(\kappa^*, Z(\omega, 0)) \exp(2ikL) - \exp(-\alpha L) F(\kappa^*, Z(\omega, L))] \right\}, \end{aligned} \quad (5.34)$$

The general contribution of non-percolated inclusions to normalized transient transmittance (2.10) with reference field (5.8) is then

$$\begin{aligned} \Delta T_{\text{norm}}^{\text{non-perc}}(\omega) = & \frac{n_1 + n_2}{2n} B \frac{\Delta \sigma_0^{\text{mic}}(\omega)}{e\alpha\phi} a \\ & \times \left\{ [1 + r_1 r_2 \exp(2ikL)] \left[\frac{\text{Ln}(1 + Z(\omega, 0)) - \text{Ln}(1 + Z(\omega, L))}{Z(\omega, 0)} \right] \right. \\ & + r_1 [F(\kappa, Z(\omega, 0)) - \exp(2ikL) \exp(-\alpha L) F(\kappa, Z(\omega, L))] \\ & \left. + r_2 [F(\kappa^*, Z(\omega, 0)) \exp(2ikL) - \exp(-\alpha L) F(\kappa^*, Z(\omega, L))] \right\}. \end{aligned} \quad (5.35)$$

In the linear regime, i.e. for low microscopic conductivities or high probing frequencies, the depth profile of effective conductivity follows the exponential absorption law (magenta in Fig. 5.1), $Z(\omega, z)$ decreases towards zero according to (5.27), and the hypergeometric function ${}_2F_1$ tends to 1. The equation (5.35) then reduces to the form of the percolated sample (5.16) with B in the place of V .

Following Eq. (5.1), the process of THz probing can be understood as an emission process of the transient wave ΔE , i.e. when the probing THz pulse E_{probe} propagates through the sample, it generates the transient signal ΔE proportional to $\Delta\sigma$ at the given depth. The total transmitted transient pulse ΔE_t is then composed of many partial waves generated at different times and positions in the sample. This is exactly taken into account by the term in the curly brackets in (5.15) and (5.34). For example, in the simple case when $\Delta\sigma$ decays exponentially with depth (e.g. in the percolated case without a strong carrier diffusion), the transient signal arises dominantly in a thin frontmost layer of the sample and the partial transient waves sum up to a transmitted pulse with a relatively simple analytical shape like (5.15). In the case when $\Delta\sigma$ attains a saturated value in a several- μm thick layer (non-percolated case depicted in Fig. 5.1), the partial transient waves are generated within a relatively thick region with comparable amplitudes. The dephasing and interferences between these waves are then analytically described with the so-called hypergeometric function as given in (5.34). We will show later with the help of our experimental results that these terms lead to peculiar interferences in the spectra of ΔT_{norm} . Eqs. (5.16) and (5.35) correctly describe these effects and allow deconvoluting them properly.

5.3.3. Thin film with strong absorption

In the important case of pump light penetration depth substantially shorter than probing THz wavelengths, $\alpha \ll k$, the hypergeometric function simplifies

$$F(\kappa \rightarrow 1; Z) \rightarrow \frac{\text{Ln}(1+Z)}{Z} \quad (5.36)$$

and the normalized transient transmittance reads:

$$\begin{aligned} \Delta T_{\text{norm}}^{\text{non-perc}}(\omega) &= \frac{n_1 + n_2}{2n} B \frac{\Delta\sigma_0^{\text{mic}}(\omega)}{e\alpha\phi} a \\ &\times \left[\frac{\text{Ln}(1+Z(\omega,0))}{Z(\omega,0)} (1+r_1)(1+r_2 \exp(2ikL)) \right. \\ &\quad \left. - \frac{\text{Ln}(1+Z(\omega,L))}{Z(\omega,0)} (1+r_1 \exp(2ikL))(1+r_2) \right]. \end{aligned} \quad (5.37)$$

In a thin film sample, ($1 \ll kL$, $k \ll \alpha$), the response finally is

$$\Delta T_{\text{norm}}^{\text{non-perc}} = B \frac{\Delta\sigma_0^{\text{mic}}(\omega)}{e\alpha\phi} \frac{\text{Ln}(1+Z(\omega,0)) - \text{Ln}(1+Z(\omega,L))}{Z(\omega,0)}. \quad (5.38)$$

5.4. General solution

The THz wave equation (5.1) can be also solved for any general depth profile of transient conductivity of the sample $\Delta\sigma(\omega, z)$. Without knowing the exact form of the source function, the solution reads:

$$\begin{aligned}
\Delta T_{\text{norm}}(\omega) = & \frac{n_1 + n_2}{2n} \cdot \frac{a}{e\phi} \\
& \times \left\{ (1 + r_1 r_2 \exp(2ikL)) \int_0^L \Delta\sigma(z, \omega) dz \right. \\
& + r_1 \int_0^L \exp(2ikz) \Delta\sigma(z, \omega) dz \\
& \left. + r_2 \exp(2ikL) \int_0^L \exp(-2ikz) \Delta\sigma(z, \omega) dz \right\},
\end{aligned} \tag{5.39}$$

which can be solved analytically or numerically after injecting the applicable $\Delta\sigma(\omega, z)$.

5.4.1. Thick sample with strong absorption

For a thick sample with a short penetration depth ($1 \ll ak$), the general normalized transient transmittance is:

$$\Delta T_{\text{norm}}(\omega) = \frac{1}{e\alpha\phi} \frac{1}{1+n} \Delta\Sigma(\omega), \tag{5.40}$$

where

$$\Delta\Sigma(\omega) = \int_0^L \Delta\sigma(\omega, z) dz = e \int_0^L \mu(\omega; N) N(z, t_p) dz \tag{5.41}$$

is the transient sheet conductivity.

In the experimental Chapter 8, photocarrier mobility in thick rutile slabs with an extremely short optical penetration depth (12 nm) are analyzed and the excitation light readily generates carrier densities $> 10^{19} \text{ cm}^{-3}$. The carrier mobility itself then depends on carrier density due to electron–hole scattering and evolves in time through diffusion. We use the numerical solution of (5.40) in that case.

6. Transport in Si-NCs derived from nanoporous Si

In this chapter we present the results of our research of Si-NC samples that were prepared in the Center of Nanotechnology and Materials for Nanoelectronics at our Institute (the Nanocenter). The samples contain Si NCs with an average size of 3 nm; such small NCs feature strong quantum confinement manifested as luminescence visible to the naked eye under UV illumination. Extensive studies of the optical properties of these samples have been conducted at the Nanocenter and we were invited to a collaboration with the aim to characterize the ultrafast transport of photogenerated carriers inside the nanocrystals.

We have found that the distribution of sizes of NCs has a crucial impact on the outcomes of photoluminescence and THz photoconductivity measurements in silicon. On the one hand, photoluminescence is by the nature of quantum confinement sensitive to *small* NCs with size below several nm. THz photoconductivity response, on the other hand, is dominated by the conductivity of *larger* NCs with sizes in tens of nm or more, although such NCs are relatively sparse in the studied samples. We thus demonstrate here the complementarity of Optical pump–THz probe spectroscopy to more traditional methods such as photoluminescence, dynamic light scattering or atomic force microscopy for characterizing samples that contain semiconducting nanoparticles of various sizes.

The first section below gives details on the preparation of the sample and of its morphological composition as determined by our collaborators at the Center of Nanotechnology and Materials for Nanoelectronics by non-THz characterization methods. Section 6.2 presents our original results obtained by THz photoconductivity measurements that were also summarized in [4].

6.1. The sample

The sample was fabricated by electrochemical etching from a *p*-type crystalline silicon (c-Si) wafer ((100)-orientation, doped by boron to 0.075–0.100 Ωcm) in an ethanol solution of hydrofluoric acid at a current density of 1.6 mA/cm². See Fig. 6.1 for a scheme of the production process. In 2 hours, a nanoporous layer was etched at the front face of the wafer. The sample was then put into H₂O₂ for several minutes, thoroughly rinsed in pure ethanol, dried and finally oxidized for several hours in an air environment with stabilized temperature and humidity. The resulting system of SiO₂-covered Si NCs was mechanically scraped off the remaining substrate. The obtained fine powder was further pulverized in an ultrasonic bath in pure ethanol for several hours. The size of the non-oxidized c-Si cores of the obtained nanoparticles depends on the duration of the post-etching treatment in H₂O₂ and also on other parameters of the production procedure. This was documented in detail in the photoluminescence study by Dohnalová et al. [101]; the samples used here are referred to as “blue” in that paper. The non-THz properties of the material reviewed in this Section were measured with nominally the same samples that were used for the THz photoconductivity measurements.

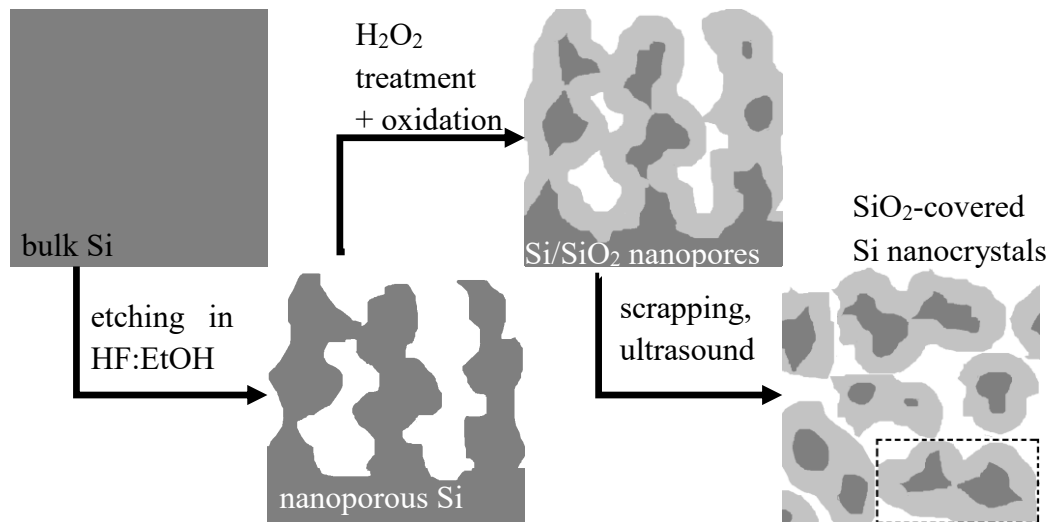
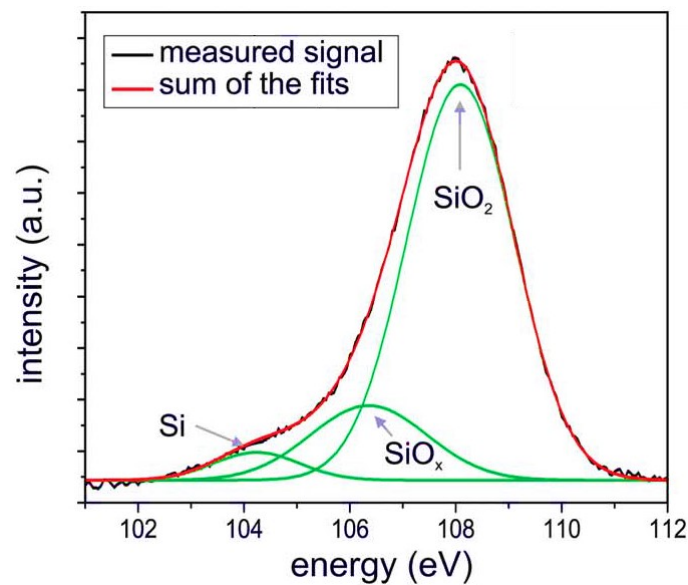


Fig. 6.1 Schematic of the fabrication process of the Si-NC powder. Dashed line indicates a possible particle with multiple Si cores.

6.1.1. Non-THz characterization

These data provide essential information on the composition of the sample that allowed us to discuss our THz data. Fig. 6.2 shows an X-ray photoelectron spectrum (XPS) of the sample powder in the energy range characteristic to transitions of $2p$ electrons in the electron shell of silicon atoms.



(Fig. 1D in [102])

Fig. 6.2 *Black line*: X-ray photoelectron spectrum of the sample powder; *red line*: fit with a sum of 3 Gaussian curves; *green lines*: Gaussian components of the fit.

The XPS spectrum is well fitted by a sum of 3 Gaussian peaks at binding energies of 104, 106 and 108 eV that are attributed to transitions in Si atoms bound into Si lattice or in SiO_x ($x < 1$) and SiO_2 molecules, respectively.

The fit of the XPS data shows that 83% of silicon is completely oxidized into silica shells; 12% of Si formed silicon sub-oxides, probably in the interlayer between the completely oxidized outer shell of the nanoparticles and the unoxidized Si cores; and 5% of silicon atoms remained in the crystalline cores after oxidation. In Table 6.1, we use the atomic masses m_a of crystalline silicon, silicon monoxide and silica glass and their densities ρ to calculate the volume occupied by the respective molecules/atom (3rd column in Table 6.1). In the last column, we recalculate the XPS Si-bond fractions to the volume fractions occupied by the respective phases in the solid part of the sample.

	m_a (m_u)	ρ (kg/m^3)	volume per 1 Si ($\times 10^{-29} \text{m}^3$)	XPS: Si atomic fraction	molecule volume fraction
c-Si	28	2330	1.99	5%	2.3 %
SiO_x	44	2130	3.43	12%	9.6 %
SiO_2 glass	60	2200	4.53	83%	88.0 %

Table 6.1 Properties and fractions of individual Si compounds in the sample powder.

Fig. 6.3(a) shows the distribution of particle diameters obtained by AFM scanning of the surface of a nominally same sample powder specimen that underwent an additional stage of ultrasound treatment in methanol. This procedure breaks larger pieces of the oxidized material that may contain multiple Si cores (schematized by the dashed rectangle in Fig. 6.1).

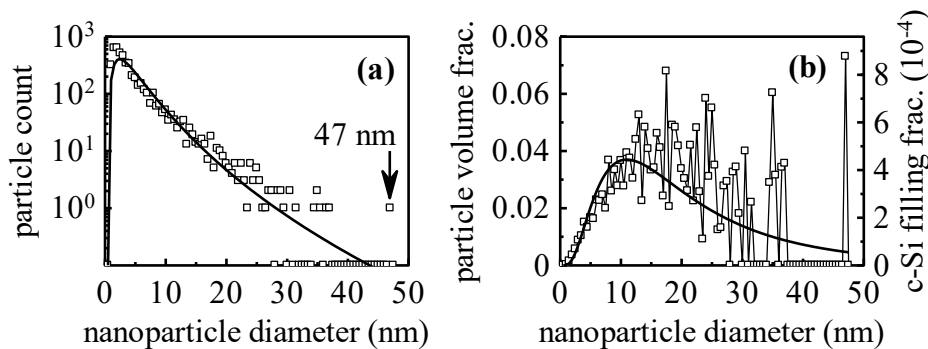
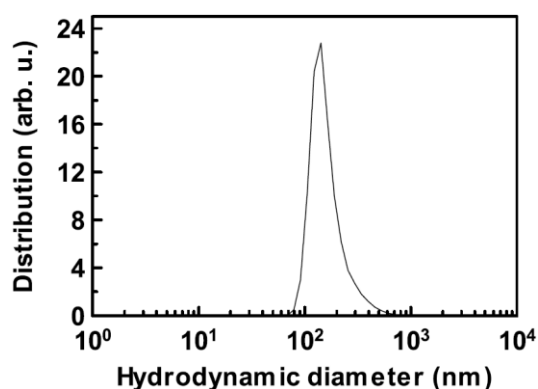


Fig. 6.3 (a) *Points*: Nanoparticle diameter histogram (0.5 nm bin width) obtained from AFM pictures of the sample, *line*: log-norm fit of the histogram. (b) volume filling fractions of variously sized nanoparticles calculated from data in (a); the right-hand axis is renormalized by the volume filling fraction of crystalline Si.

The distribution of sizes of solid particles in this specimen is thus the nearest to the distribution of sizes of crystalline Si cores. During AFM measurement only a few particles larger than 20 nm were observed; however, it has been also shown that even bigger particles can be occasionally present in the sample as e.g. the solitary 47-nm particle reported in Fig. 6.3. The red line shows the log-norm fit as the probable extrapolation of the particle distribution to the large-diameter region if the counting were done on a statistically much larger amount of particles.

The photoluminescence of Si NC samples is proportional to the number of very small NCs which feature quantum confinement. However, the THz conductivity does *not* scale with the number of NCs possessing a given size but rather with the total *volume* that the photoconductive NCs occupy in the sample. For this reason, we recalculate the particle count from Fig. 6.3(a) to volumes occupied by the particles in Fig. 6.3(b). (The left-hand axis in Fig. 6.3(b) gives the volumes occupied by particles of a given diameter among the total volume of all the particles. The right-hand axis is normalized by a factor of 1.2% because crystalline Si occupies 2.4% of the solid particle volume (Table 6.1) and we show later that the sample powder contains about 50% of air.)



(Fig. 1.(c) in [4])

Fig. 6.4 Dynamic Light Scattering data on our sample of nanoporous-Si-derived Si nanocrystals.

The red-line fit from panel (a) was also recalculated and shown in panel (b) to provide an estimate of the volume occupied by the larger particles. We see that in terms of volume, the filling fraction of particles above 10 nm cannot be neglected. Fig. 6.3(b) then appears much more relevant to the analysis of THz conductivity data than Fig. 6.3(a). Note that the role of very large solitary particles in the total photoconductivity signal can be very important. Indeed, Dynamic light scattering (DLS) data in Fig. 6.4 shows that there may be several particles as big as 0.5 μm in the sample. Let us remind that the DLS signal is proportional to d^6 and the light scattering of the small NPs, clearly present in the AFM data, is thus completely hidden by the response of the few large particles in Fig. 6.4. On the other hand, DLS data do not provide any information about the composition and morphology of the particles that it detects; consequently, we cannot affirm with certainty that the

volume of the largest particles contains one percolated c-Si network (without e.g. SiO₂ barriers) or several isolated c-Si cores.

6.1.2. Preparation of samples for THz measurements

The powder specimen for each sample was put into a custom-made cuvette for the purpose of transient THz transmission spectroscopy. The cuvette was composed of two 1-mm-thick fused silica plates serving as input and output windows separated by a 200 μm thick polytetrafluoroethylene (PTFE, Teflon) spacer. A circular hole in the spacer with a diameter of about 5 mm served as the cavity for the specimen. The specimen was put into the cavity by a pipette and slightly pressed between the silica plates before the whole cuvette was glued together. Special attention was paid not to let the glue soak into the central area of the specimen cavity. The cuvette was then attached onto the sample holder (a thin steel plate with a circular 3mm-in-diameter aperture).

Three samples were prepared in total. The sample labelled C was damaged by evacuation of the cryostat sample chamber between individual sets of measurements; the air that was sealed with the sample powder inside the cuvette cavity tore apart the cuvette and subsequently, a substantial amount of the sample powder was virtually vacuum-cleaned away from the cuvette. This sample thus did not provide a complete sets of data necessary for successful analysis. Only a short THz transient kinetics scan is presented. The cuvette and the specimen in the cavity remained visually undamaged and homogeneously opaque in the case of samples A and B and the THz photoconductivity measurements were reproducible. These two undamaged samples were prepared from the very same dose of the sample powder. The powder for sample A was, in addition to the treatment underwent by sample B, left in a high power ultrasonic bath with ethanol (absorbed energy 400 kJ) that was supposed to break large NC clusters into smaller ones.

6.2. THz photoconductivity

Table 6.2 summarizes the steady-state THz and optical properties of the sample that were measured independently on THz photoconductivity spectra to serve as input parameters of the presented THz photoconductivity model. The THz refractive index was obtained from the measured sample thickness and the time delay of the transmitted THz pulse induced by the unexcited sample introduced into the THz beam path.

The total filling fraction of the solid phases (Si+SiO+SiO₂) in 3rd column of Table 6.2 was calculated from the Bruggeman EMT (3.19) for spherical particles under the assumption that the THz refractive index of the solid phase lies between 1.97 and 2.1. This estimate is based on the fact that the solid phase contains 90% of silica (Table 6.1) with a THz refractive index of 1.97 and minor fractions of SiO and Si with higher THz refractive indices. With >50% of the samples occupied by air (Table 6.2), the c-Si occupying 2.4% of volume of the solid phase of the sample (Table 6.1) has a filling fraction <1.2% in the total volume of the samples.

The effective absorption coefficients α of the samples at 400 nm (3.1 eV, see the last two columns of Table 6.2) was assessed by comparing the powers of the incident, reflected and transmitted excitation light as measured with a power meter.

Sample	L (μm)	n_{THz}	filling fraction (Si+SiO ₂ +SiO)	$\alpha_{400 \text{ nm}}$ (cm ⁻¹)	$1/\alpha_{400 \text{ nm}}$ (μm)
A	220	1.45	0.44–0.49	590	17
B	260	1.33	0.34–0.37	500	20

Table 6.2 Summary of the optical and steady-state THz properties of the samples.

Transient THz kinetics

Excitation at 400 nm (3.10 eV) was used for the following THz photoconductivity measurements in a range of fluences between 2×10^{12} and 1×10^{15} photons/cm². Several THz kinetics were measured at the maximum fluence to find the optimal time interval for measuring transient THz photoconductivity spectra. The black line in Fig. 6.5(a) shows the transient kinetics at 20 K for sample C: the transient response of the sample does not decay in the measured time range but features an unexpected oscillation of the transient signal between 0 and 10 ps that was identified as a parasite signal as follows. The blue line in Fig. 6.5(a) shows the net THz field detected by the sensor when the THz probe beam was blocked out. The same parasite signal was also detected with a completely different sample (CdS thin film on silica substrate) while it was never observed in measurements without the cryostat. The parasite signal thus must be emitted by the cryostat sapphire input windows upon excitation by the intense pump pulses (optical rectification).

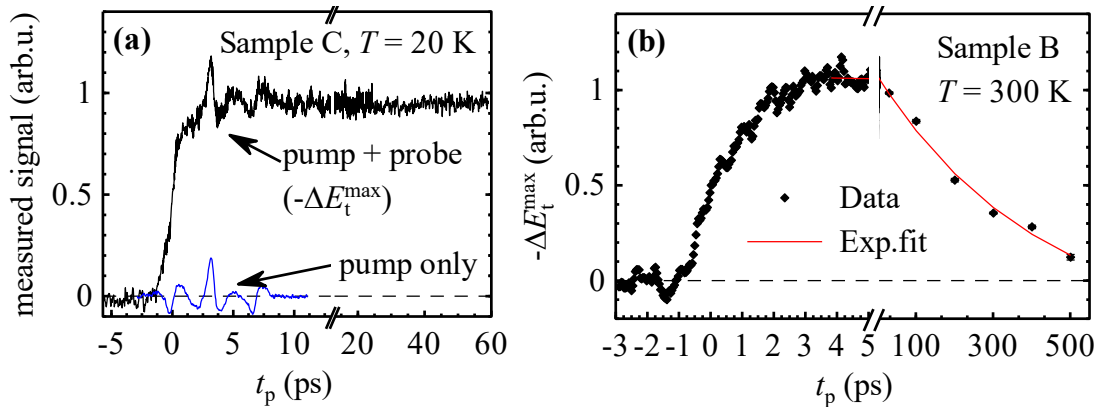


Fig. 6.5 Transient THz kinetics of Si-NC samples B and C.

Fig. 6.5(b) shows the transient kinetics at 300 K for sample B: the signal decays on the time scale of ~ 450 ps; we attribute this decay to the trapping of carriers in the states at nanocrystal boundaries, as the prevailing part of radiative recombination occurs on much longer time scales [101]. THz photoconductivity spectra were measured between 20 and 30 ps after photoexcitation to avoid the parasite signal due to optical rectification in sapphire and still obtain the highest

measurable photoconductivity response. The transient THz spectra were measured at 20, 100, 200 and 300 K. Accumulation of the transient THz spectrum at the lowest excitation density (signal level below 10^{-4} with respect to the steady state transmission) took up to 17 hours.

6.2.1. Measured spectra and fitting model

Experimental spectra of THz photoconductivity of sample A are shown as symbols in Fig. 6.6 at various temperatures and excitation fluences. All the spectra feature a periodic oscillating pattern (~ 0.3 THz wide peaks/minima) due to dephasing and interferences of the transient THz waves in the sample that has an unfavorable combination of thickness, transient THz refractive index and pump light penetration depth with respect to THz wavelengths. The final fitting function (color-matched lines in Fig. 6.6) does take these effects rigorously into account and we comment on them in detail in a separate subsection after we present the principal results of our analysis and fits. First, let us discuss the overall shape of the measured spectra: we leave out of account the periodic pattern and consider the global slope and/or global extreme of the real part and the sign of the imaginary part of the normalized response in Fig. 6.6.

The preparation procedure of the sample virtually excludes the possibility of long-range percolation pathways in the sample. In this case the effective medium analysis in Chapter 4 suggests us to look for a localized plasmon resonance in the spectra. The signature of the resonance in the spectrum is a maximum in the real part of the response and the imaginary part being negative below the resonance frequency and positive above it. The spectra measured at the highest excitation densities (rightmost plots in Fig. 6.6) feature a capacitive type of response at all temperatures — such response corresponds to a resonance located above the accessible frequency range. With decreasing excitation fluence (from right to left at each row), the resonance redshifts as predicted by the EMT analysis (cf. Fig. 4.5 on p. 48). At the same time, the amplitude of the response increases, as indicated in Fig. 4.5.

In Chapter 4 (Section 4.3 in particular), we have shown that with decreasing carrier density, the measured THz photoconductivity can finally enter the linear regime in which the measured spectrum has basically the same shape as the actual spectrum of microscopic carrier conductivity. The lowest excitation density in sample A was achieved at low temperatures (4th row in Fig. 6.6), when the signal is the strongest due to increased carrier mobility in silicon. In the magenta spectrum, the resonance has redshifted below the accessible frequency range and an inductive type of response is observed: the real part of the response is decreasing with frequency and the imaginary part is positive. Such a response, disregarding the periodic oscillations, corresponds to Drude-like conductivity of the material. This unambiguously indicates the presence of carriers that are delocalized on the length scale of at least several carrier mean free paths. [70] We consequently performed the first series of fits as follows.

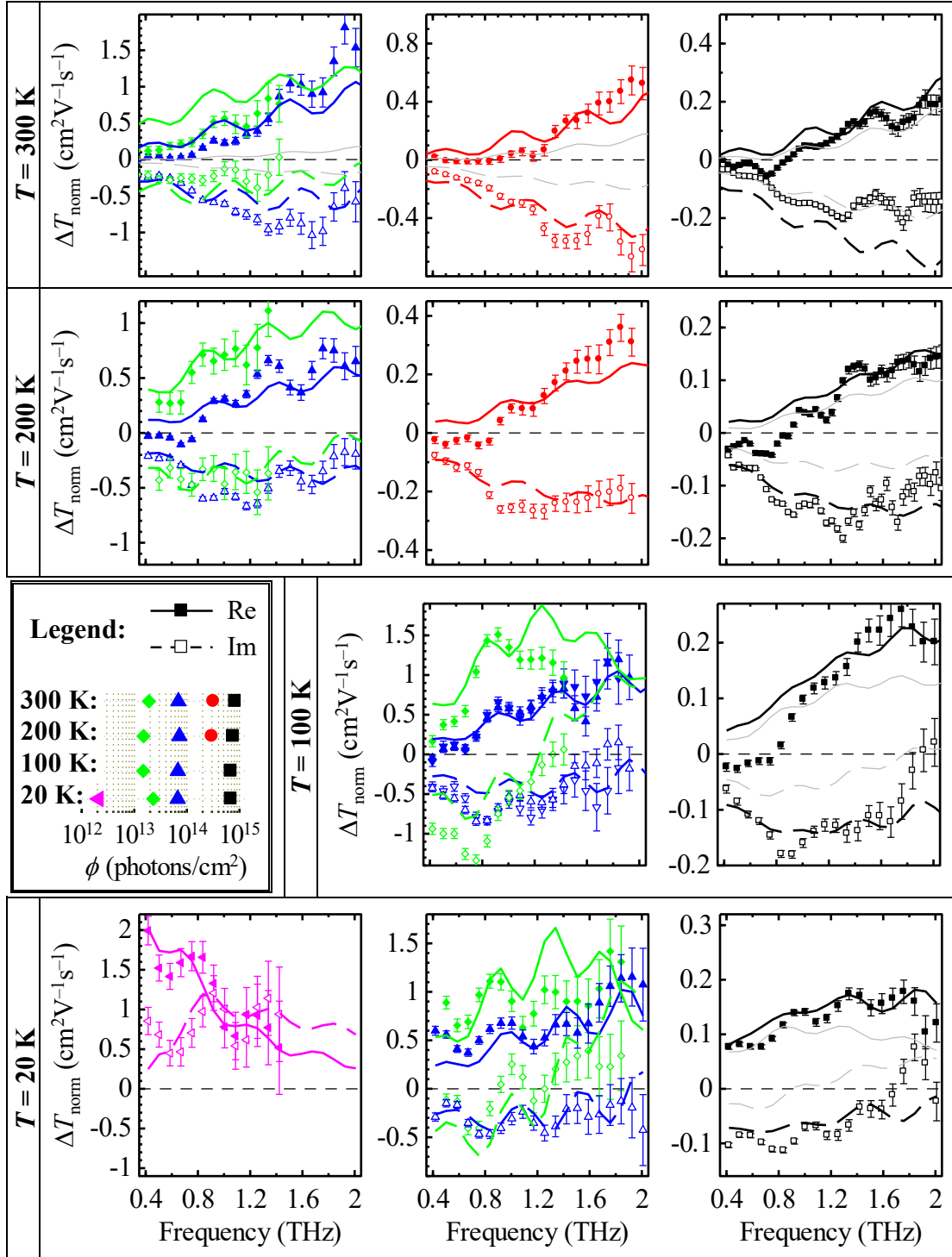


Fig. 6.6 *Symbols*: THz photoconductivity spectra of sample A at various temperatures (rows) measured 20 ps after excitation with 400 nm pulses at various excitation fluences ϕ as indicated in the legend (only 3 fluences were used at 100 K). ϕ increases from left to right at each row, the x -axis is the same for all plots. *Color-matched lines*: fit with (6.3); *gray lines*: linear component of the fit.

Primary fitting model

At each temperature, spectra of the normalized transient transmittance measured at different excitation densities were fitted with the theoretical response function $\Delta T_{\text{norm}}^{\text{non-perc}}(\omega, \phi)$ calculated according to (5.35), i.e. the general response of a sample with non-percolated photoconductive inclusions in the VBD approximation.

The changes of the spectral shape with excitation density is expressed in (5.35) through the dependence of $Z \propto \Delta\sigma^{\text{mic}} \propto \phi$ (5.27). The spectral shift of the resonance is described by the $[\text{Ln}(1+Z(\omega,0))-\text{Ln}(1+Z(\omega,L))]/Z(\omega,0)$ term in (5.35). The terms with the hypergeometric function $F(\kappa, Z)$ in (5.35) describe the periodic oscillations in the spectra. The input for the theoretical response function is the model spectrum of the microscopic conductivity at the photoexcited surface $\Delta\sigma_0^{\text{mic}}(\omega)$.

Due to the observation of the Drude type of effective conductivity at low photocarrier densities, the conductivity spectrum of carriers with Drude type of mobility (3.1) was used:

$$\Delta\sigma_0^{\text{mic}}(\omega) = e N_0^{\text{mic}} \mu_{\text{Drude}}(\omega) = \frac{e^2}{m^*} \alpha^{\text{mic}} \phi \xi \frac{\tau_s}{1 - i\omega\tau_s}, \quad (6.1)$$

with τ_s (bulk scattering time) and ξ (quantum yield of photogeneration) being the fitting parameters of the microscopic response. The carrier effective mass was fixed to that of electrons in bulk silicon $m^* \approx 0.26 m_e$.

The morphology factors B, D in (5.35) were defined by an adjustable value of s (c-Si filling fraction) within the Maxwell Garnett approximation (4.9,4.10). This approximation of the morphology factors is applicable here because the expected value of the filling fraction of crystalline Si (Table 6.1) is rather low and the existence of percolation pathways in our samples is highly improbable: the c-Si NCs are surrounded by insulating oxide shells. The shape factor K in (4.9,4.10) was fixed to 2, which represents particles with an average aspect ratio close to 1. All spectra at one temperature were fitted with a single set of 3 fitting parameters: s, ξ and τ_s .

These fits (not shown) reproduced well the major part of the measured photoconductive response, indicating that the most of the signal indeed originates in non-percolated nanocrystals with Drude microscopic conductivity spectrum. Two remarkable facts lead us to an extension of the fitting function:

1) The filling fraction s converged to values in the order of 2×10^{-4} for all temperatures which is more than an order of magnitude below the expected 1.2% total filling fraction of c-Si. This means that the major, Drude-like, part of the measured response originates in a relatively small subgroup of the nanocrystals in the sample. Fig. 6.3(b) shows at the right-hand axis that c-Si cores in a wide range of larger diameters may just correspond to a filling fraction around 2×10^{-4} . We show later by Monte-Carlo calculations that the Drude-like response originates in bigger nanocrystals.

2) The single-component model fits the photoconductivity well for lower excitation densities (typically left and medium column in Fig. 6.6) but it underestimates the actual measured response at the highest excitation densities. An additional term thus has to be added to fit satisfactorily the data for all measured excitation densities within a single model. As this component comes out only for high pump fluences, it must be described by a ϕ -linear transient transmittance contribution where the signal saturation due to the depolarization fields does not occur. This condition is fulfilled in two cases: either the component is percolated — which is not probable — or it is non-percolated but characterized by such a *low* microscopic mobility and/or *low* morphology D -factor that the macroscopic conductivity still scales linearly with the microscopic one at the present excitation densities (cf. Section 4.3). The normalized transient transmittance function (5.35) of this additional component then reduces to (5.16) with the morphological parameter B at the place of the filling fraction V in (5.16).

Final fitting model

As the nature of the microscopic mobility corresponding to the second component is unclear, we first formally described it using the Drude-Smith shape of the microscopic conductivity spectrum (3.30) that provides an analytical flexibility for both capacitive or inductive type of carrier response in a limited spectral range:

$$B\Delta\sigma_0^{\text{mic}}(\omega) = BeN_0^{\text{mic}}\mu_{\text{Drude-Smith}}(\omega) = B\frac{e^2}{m^*}\alpha^{\text{mic}}\phi\xi\frac{\tau_{\text{DS}}}{1-i\omega\tau_{\text{DS}}}\left[1+\frac{c_1}{1-i\omega\tau_{\text{DS}}}\right]. \quad (6.2)$$

The adjustable parameters of this component are τ_{DS} (characteristic time of the Drude-Smith model), c_1 (Drude-Smith “backscattering” parameter) and the morphologic parameter B (the morphologic parameter). The adjustable quantum yield ξ is common for both the components (6.1,6.2). The actual character of the microscopic transport corresponding to the model Drude-Smith spectrum is evaluated afterwards by using Monte-Carlo calculations of the mobility spectra of carriers confined in nanocrystals of various sizes.

The final fitting was performed using the prescription:

$$\Delta T_{\text{norm}}(\omega, \phi) = \Delta T_{\text{norm}}^{\text{non-perc}}(\omega, \phi) + \Delta T_{\text{norm}}^{\text{linear}}(\omega) \quad (6.3)$$

where $\Delta T_{\text{norm}}^{\text{non-perc}}$ is given by (5.35) with the Drude microscopic conductivity spectrum (6.1) and $\Delta T_{\text{norm}}^{\text{linear}}$ is given by (5.16) with Drude-Smith microscopic conductivity spectrum (6.2) in the place of $V\Delta\sigma_0^{\text{mic}}(\omega)$. We further refer to the non-linear Drude term as to the primary conductivity component and to the linear Drude-Smith component as to the secondary component. The absorption coefficient of Si NCs is significantly modified with respect to its bulk value only in the smallest NCs, which are not expected to contribute significantly to the THz conductivity spectra. Therefore, we assume that the local absorption coefficients in both

photoconductive components are the same: $\alpha^{\text{mic}} = \alpha_{\text{Si}} = 1 \times 10^5 \text{ cm}^{-1}$ at 300 K, decreasing linearly to $7 \times 10^4 \text{ cm}^{-1}$ at 20 K.

The spectra obtained for different excitation densities were weighted by their statistical errors (indicated by the error bars in Fig. 6.6) in the global fit at each temperature. The fitting parameters were s , and τ_S for the primary component B , c_1 and τ_{DS} for the secondary component and ζ for both components. Results of these complex fits are shown as lines in Fig. 6.6. A very good match was achieved for all the spectra.

The secondary contribution $\Delta T_{\text{norm}}^{\text{linear}}$ is also plotted separately as gray lines in Fig. 6.6. For clarity, we plot it only in selected plots at each temperature. We remind that the part of the *normalized* transient transmittance ΔT_{norm} (2.10) related to the linear contribution does not depend on ϕ and thus it makes the same contribution in all spectra at each individual temperature. Consequently, it presents a significant contribution only for the highest excitation densities.

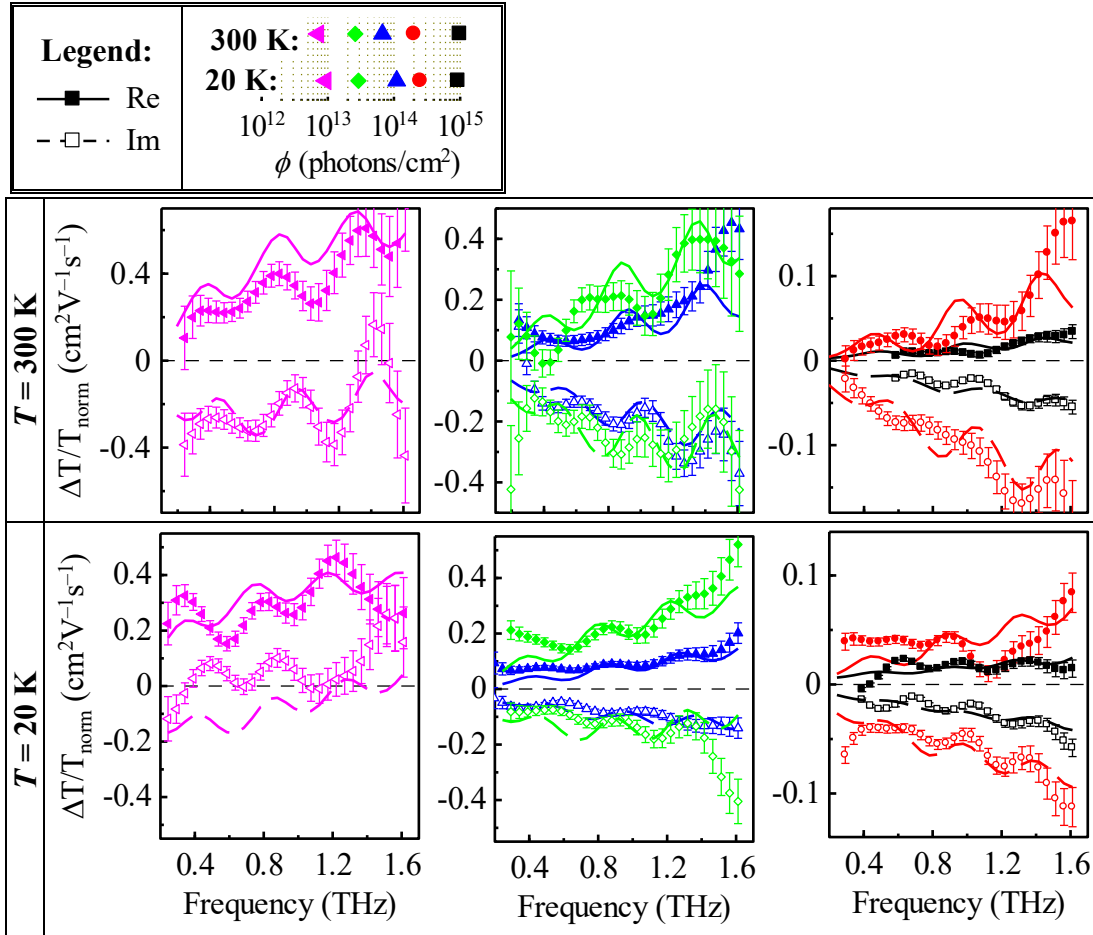


Fig. 6.7 *Symbols*: THz photoconductivity spectra of sample B at 300 and 20 K (rows) measured 30 ps after excitation with 400 nm pulses at various excitation fluences ϕ as indicated in the legend. ϕ increases from left to right at each row, the x -axis is the same for all the plots. *Lines*: fit using (6.3).

Fig. 6.7 shows spectra of the measured THz photoconductivity at 300 and 20 K for sample B. Spectra at 100 and 200 K (not shown) were also measured and successfully fitted. We observe qualitatively the same behavior as with sample A. However, the normalized response of sample B is almost 10 times lower at the highest excitation fluences than that of sample A (compare black symbols in Fig. 6.7 to the same in Fig. 6.6). At the lowest excitation fluences ($<1 \times 10^{13} \text{ cm}^{-2}$, magenta symbols in Fig. 6.7), the response of sample B is still 2 times lower than that of sample A at comparable excitation fluences ($\approx 1 \times 10^{13} \text{ cm}^{-2}$, green symbols in Fig. 6.6). For this reason, it was not possible to reach as low excitation fluences as with sample A. The two-component normalized response model (6.3) was also successfully used to fit the spectra of sample B as shown in color-matched lines in Fig. 6.7.

6.2.2. Spectral oscillations

Our model very well reproduces the interference pattern observed in the measured spectra (Fig. 6.6, Fig. 6.7). The THz probing process can be understood as an emission of the transient THz wave ΔE in the photoexcited sample [40] as it has been already discussed at the end of paragraph 5.3.2. If we keep this language, the emitted THz partial waves inside the sample will have the wave vectors parallel and antiparallel with the probing THz wave; interference of these waves is described by the expression in curly brackets of (5.35) and it is at the origin of the observed spectral modulation of the transient signal. The standard “steady-state” Fabry-Pérot interferences are described by the term a in (5.35). The role of these interferences is demonstrated in Fig. 6.8.

Black lines in Fig. 6.8 show the fit of one *actual* experimental spectrum of sample A (cf. the blue spectrum at 20 K in Fig. 6.6). The dotted red line in Fig. 6.8 shows the hypothetical response of sample A if the steady-state Fabry-Pérot interferences were neglected in the measured transient transmittance: we clearly observe that this effect is only very minor. The blue dash-dotted line in Fig. 6.8 shows the hypothetical spectrum of sample A without the terms containing the hypergeometric function F in (5.35). This approximation corresponds to neglecting partial waves with antiparallel wave vectors to the probing wave as described above and leads to the suppression of the interference of forward and backward emitted transient waves. The resulting spectrum is almost flat.

It is clear from Fig. 6.8 that the oscillations in the experimental spectra are caused dominantly by the dephasing effect in the non-percolated sample while the interferences due to the multiple reflections on the cuvette walls have only a negligible effect on the transient transmittance spectra of our actual samples. This shows the importance of a careful evaluation of non-equilibrium interference phenomena in the spectra in order to avoid misinterpretation of the experimental results.

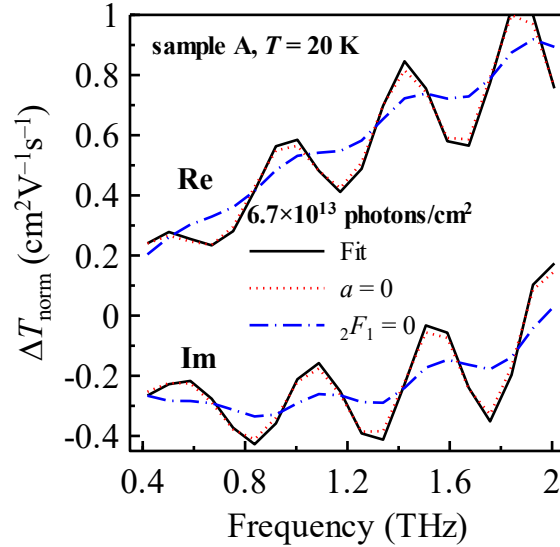


(Fig. 2. in [4])

Fig. 6.8 Theoretical spectra of ΔT_{norm} following (5.35); *black solid line*: fit to the data (sample A, $T = 20$ K, moderate excitation density), *dotted red line*: spectra with the same parameters but with $a = 0$ (equilibrium Fabry-Pérot internal reflections are neglected), *dash-dotted blue line*: spectra with the same parameters but terms with the hypergeometric function (transient interference terms) are neglected.

6.3. Discussion

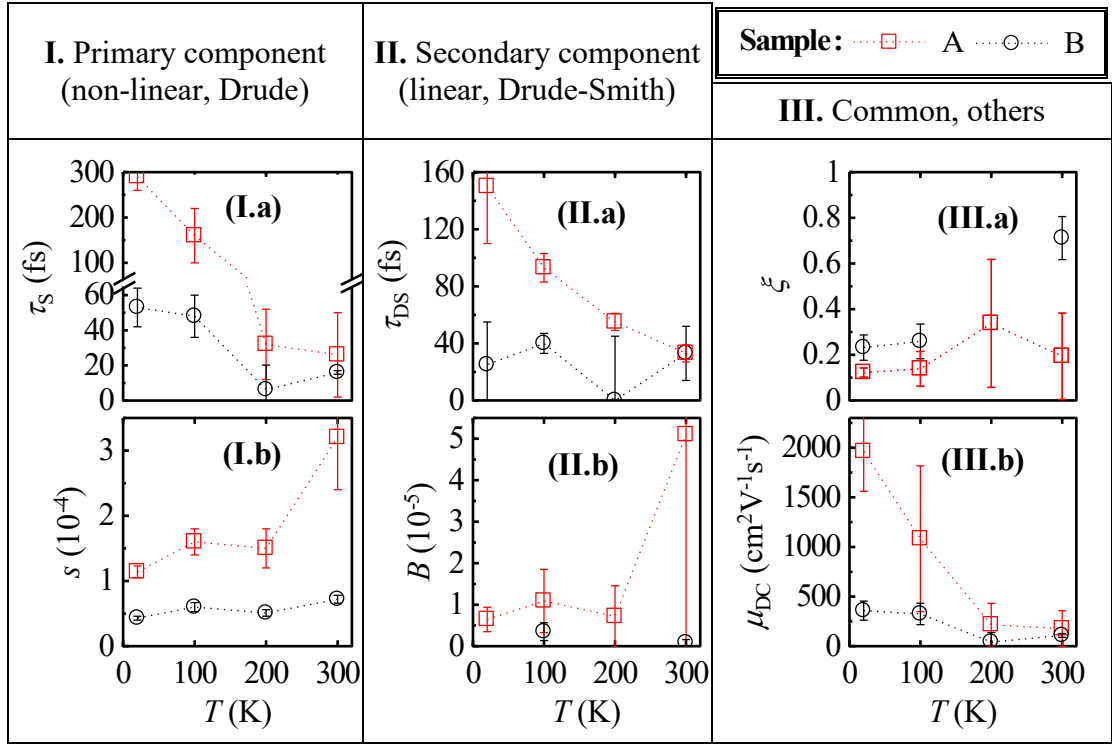
Fig. 6.9 presents the temperature dependences of the converged values of fitting parameters in both samples. Parameters of the two contributions entering (6.3) are arranged separately in panels I. and II. of the figure. The error bars indicate standard uncertainty of the fit. The Smith coefficient c_1 (not plotted) was found in general to be close to -1 with the exception of sample B at 300 K where its value converged to -0.93 ± 0.02 .

We first discuss the values and temperature dependences of the characteristic times of the Drude and Drude-Smith microscopic conductivity models. By a comparison of the fitted microscopic conductivity spectra of the two components to the mobility spectra of carriers confined in NCs calculated using the Monte-Carlo method, we link the two components to different sizes of individual photoconductive NCs. Subsequently, we discuss the quantum yield and filling fraction parameters in relation to the non-THz measurements presented in the introduction of this Chapter.

Drude scattering time and Drude-Smith time

The Drude scattering time τ_S (Fig. 6.9(I.a)) and the Drude-Smith (DS) time τ_{DS} (Fig. 6.9(II.a)) follow a similar temperature dependence (this is observed in both samples). This suggests that τ_{DS} may be of similar origin, i.e. the DS component may also arise from charge carriers with Drude-like motion that are confined inside smaller NCs. This process was described in [70], where the Drude-Smith time fitted

to mobility spectra of free carriers in NCs of various sizes was shown to decrease progressively from the value of the Drude scattering time of the carriers upon a decrease of the NC size: exactly this behavior is observed in Fig. 6.9: τ_{DS} is comparable to or smaller than τ_S . The monotonous decrease of the Drude scattering time with temperature indicates that carriers inside the examined NCs scatter mainly on phonons — this is natural when we consider that the crystalline NC cores originate from a low-defect source Si wafer. A similar behavior is found also with the Drude-Smith time in sample A; in sample B, a possible temperature dependence of τ_{DS} is below the uncertainty of the fit.



(panels τ_S , τ_{DS} were published in Fig. 7. in [4])

Fig. 6.9 Temperature dependence of the fit parameters of individual components of the model (6.3). The quantity in panel (III.b) is calculated from (I.a) as $\mu_{DC} = e \cdot \tau_S / m_{Si}^*$, with $m_{Si}^* = 0.26 m_e$.

Monte-Carlo mobility spectra

In order to find the origin of the Drude and Drude-Smith components, we carried out Monte-Carlo calculations of the THz mobility spectrum of carriers in isolated Si NCs with various sizes. We focus mainly on the sample A at low temperatures where the longest Drude scattering time of 300 fs (cf. Fig. 6.9(I.a)) was observed because this situation provides the best opportunity for correlating the THz spectra with the characteristic sizes of nanocrystals. The results of the simulations are shown in Fig. 6.10. Based on these spectra we can state that the Drude-like response in the available frequency range is characteristic to NCs larger than ~ 60 nm. The shape of the mobility spectrum of such nanoparticles qualitatively corresponds to the

observed microscopic spectrum of the dominant non-percolated contribution (magenta lines in Fig. 6.6). This implies that sample A must contain a certain amount of large (>60 nm) Si NCs whose effective response dominates the THz transmission spectrum at low to medium excitation densities. The additional fluence-independent contribution is described with the Drude-Smith spectral shape with $\tau_{DS} = 160$ fs (cf. Fig. 6.9(II.a)). The blue lines in Fig. 6.10 show the Drude-Smith-type mobility (Eq. (6.2) divided by $e\alpha\phi$) for this case — we see that it corresponds very well to the mobility of free carriers confined in NCs with diameters between 20 and 30 nm.

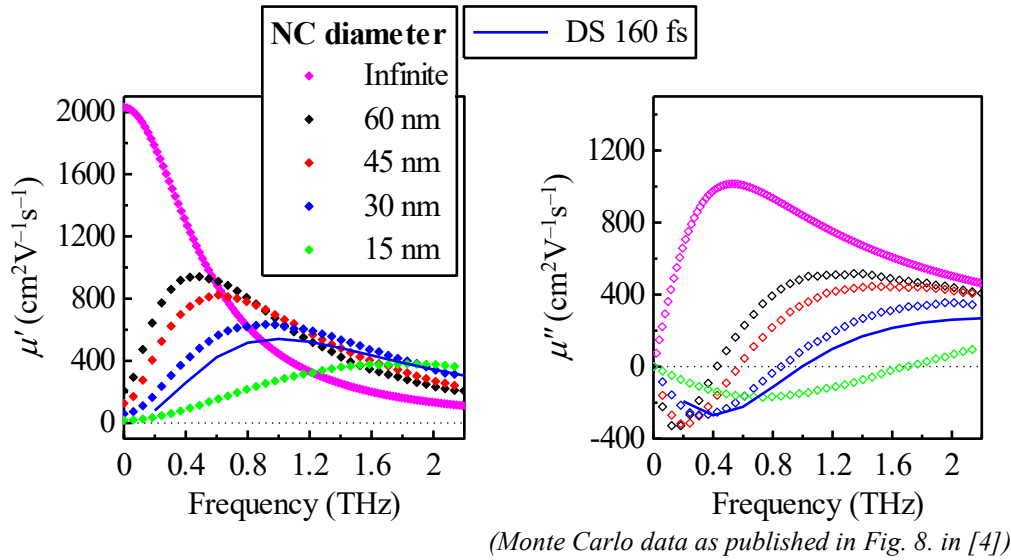


Fig. 6.10 *Symbols*: Spectra of microscopic mobility in Si NCs with various sizes at temperature 20 K ($\tau_S = 300$ fs, $m^* = 0.26 m_e$, $l_{\text{free}} = 10$ nm) calculated by the Monte Carlo method of carrier motion. *Lines*: Drude-Smith type of mobility for $m^* = 0.26 m_e$, $c_1 = -1$ and $\tau_{DS} = 160$ fs (solid blue line) or $\tau_{DS} = 40$ fs (dashed black line).

Note, that the distribution of the NC size in our samples is very broad (cf. Fig. 6.3). The exact photoconductive response is given by a sum of partial contributions over all NC sizes (weighted by their volume). It is not possible to infer such complete information from the experimental data. For this reason, we approximated the real situation by two contributions (each describing a broader distribution of sizes) related to large and medium NCs. The amplitude of the signal due to medium and small NCs is much lower than that due to large NCs (Fig. 6.10) hence the role of depolarization fields should be weaker, in agreement with observations. We were unable to develop a more quantitative model, as the observed Drude-Smith component is rather weak; moreover, phenomena such as carrier-carrier scattering may already come into play for the highest excitation densities.

Quantum yields and filling fractions

The filling fraction s of the primary component, plotted in Fig. 6.9(I.b), converged to approximately 2 times larger values with sample A than with sample B.

At the same time, the primary component in sample B is characterized by a 5 times shorter Drude scattering time (Fig. 6.9(I.a)). This means that sample A contains a significantly larger amount of large NCs than sample B and that the large NCs in sample A are more conductive.

The quantum yield ζ (for both components) and morphology parameter B (for the secondary component) occur as multiplicative factors of τ_S and τ_{DS} in the amplitude of the respective microscopic conductivities (6.1), (6.2). The relaxation times τ_S and τ_{DS} are essentially linked to the shapes of the spectra and thus they represent the primary fitting parameters of the models. The parameters ζ and B are partially anti-correlated to them and we do not plot the values of ζ , B in Fig. 6.9(III.a,II.b), respectively, in the cases when the fitting uncertainty of τ_S , τ_{DS} is larger than its mean value.

We find the quantum yield to be of the order of 10–30%, mostly temperature independent. This indicates that a large fraction of excitation photons creates carriers that are very rapidly (< 500 fs) trapped or that it is absorbed in surface-related defect states, which do not interact with THz radiation. Note that the NCs probably have a spongy structure (due to the etching) characterized by a large surface area which enhances the absorption near the surface. Photonic confinement effects may be also responsible for the decrease in the effective absorption as observed in [96].

Fig. 6.9(II.b) shows that the morphology parameter B of the secondary component is of the order of 10^{-5} in sample A and probably even lower in sample B. The Maxwell Garnett interpretation of the VBD model (4.9) can be used to extract the filling fraction of the secondary component from the fitted value of B . Filling fractions of the order of 10^{-4} (cf. Fig. 6.3(b)) are not contradictory to $B \sim 10^{-5}$. However, we find equation (4.9) to be very sensitive to input parameters (e.g. the permittivity of the “matrix” formed of voids and Si oxides) for such low value of B .

Finally, we stress that the observation of better photoconductive properties in the sample A (as compared to the sample B) is counter-intuitive and rather surprising (cf. Fig. 6.6 and Fig. 6.7). The additional treatment in ultrasonic bath that the sample A had been submitted to, was expected to split large agglomerates (50–100 nm in diameter) of interconnected NCs and, accordingly, to break narrow conductive channels between them. The experiment did not confirm this expectation. Several hypotheses may be put forward to explain it:

- (i) Under strong prolonged sonication, smaller aggregates of Si NCs approximately 20–30 nm in diameter are created, indeed (see Fig. 1), but being subsequently compressed in the measurement cuvette, the Si NCs cores may become connected to each other, giving rise to a higher microscopic conductivity.
- (ii) The oxidized shells of some NCs or aggregates might be damaged and partially removed owing to the sonication. This may favor the formation of Si NC aggregates with good electrical connection among the crystalline cores; such aggregates then behave as effectively larger particles with higher microscopic conductivity.

- (iii) Accidental presence of a few big micrometer grains of bulk Si (as a reminder of the silicon wafer on which the native porous silicon was prepared) can overwhelm the contribution of Si NCs to the overall photoconductivity. In this respect, Si NCs samples with narrower size distribution and free of possible micrometer grains are needed for subsequent study.

6.4. Conclusion

THz photoconductivity spectra of SiO₂-covered Si nanocrystals prepared by electrochemical etching of Si monocrystal were analyzed between 20 and 300 K. The response of investigated samples is dominated by the carrier-density-dependent effective conductivity of large NCs with the Drude type of carrier mobility. The size of such nanocrystals was estimated to be at least 60 nm by comparing the data to Monte Carlo calculations of the carrier mobility in variously sized nanostructures. An additional low-conductivity component appears in the measured THz photoconductivity spectra at high excitation densities when the response of the dominant component is shifted above the accessible frequency range by the effect of depolarization fields in the non-percolated sample. The response of this additional component was identified to be characteristic to the mobility of carriers in NCs in the size range 10–30 nm.

The presence of nanoparticles in the range between 50 and 100 nm was not revealed by more traditional techniques of Atomic force microscopy, Photoluminescence of quantum-confined carriers and Dynamic light scattering. Transient THz spectroscopy thus occurs to be a very valuable complement to these techniques, which is further stressed by the fact that the response of large NCs was unambiguously assessed despite of their low volume filling fraction.

These facts shed light on the long-lasting discrepancy in nanomaterials that feature measurable long-range conductivity and simultaneously exhibit effects of substantial carrier confinement. Such a situation was recently observed e.g. in nanocrystalline CdS [47] where the confinement within ~10 nm sized nanocrystals is observed by a shift of the intra-band absorption edge [103] while the carrier transport at THz frequencies does not seem to be significantly hindered by the nanocrystal boundaries. Long- or mid-range charge transport in such nanomaterials can be mediated by very small fractions of larger nanoelements that are:

1. hardly detectable by experimental techniques that have been tailored for characterizing the physically novel properties of the smallest constituents of the examined nanomaterials and
2. whose presence is not expected in these materials because their fabrication procedure focuses on preparing the highest attainable concentrations of the really small nanoelements.

7. Si-NC superlattices

The study of nanocrystals derived from nanoporous Si in the previous chapter showed that the THz photoconductive response of nanomaterials may be cloaked by the response of low concentrations of large photoconductive particles that form only a tail in the nanoparticle size distribution. Therefore, we aimed to get more control on the nanocrystal size distribution. In this chapter, we examined THz photoconductivity of Si nanocrystals made by thermal decomposition of epitaxial layers of Si-rich silicon oxides, resulting in much narrower NC size distributions.

We first overview the sample growth procedure, the energy-filtered transmission electron microscopy (EFTEM) pictures and NC size distribution analysis that we received from the production laboratory at Freiburg University. THz photoconductivity spectra are analyzed subsequently using the VBD effective medium model with model mobility spectra of carriers confined in NC calculated using the Monte Carlo method.

In brief, superlattices of alternating layers of a defined silicon oxide (SiO_x , $x < 1$) and pure silicon dioxide (SiO_2) were prepared by plasma enhanced chemical vapor deposition. Each sample consisted of 40 $\text{SiO}_x/\text{SiO}_2$ bilayers. One hour of annealing at 1150°C lead to disproportionation of silicon monoxide in the SiO_x layer:



and the precipitates of atomic Si together with the excessive Si formed nanocrystals separated by the remaining silicon dioxide. The SiO_2 interlayers serve as diffusion barriers for Si and the obtained Si NCs are thus retained in single-NC-thick layers. All SiO_x layers in a single sample have the same thickness L_{layer} and stoichiometry parameter x and the samples thus contain NCs with a narrow size distribution. By changing these two parameters (L_{layer} and x), samples with NCs of different sizes are prepared [104,105].

7.1. Sample morphology and optical properties

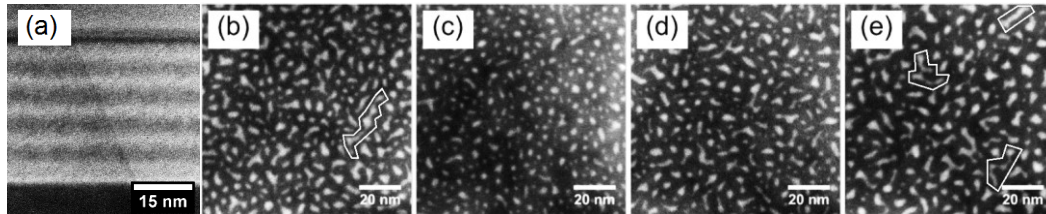
We investigated THz photoconductivity of 5 different samples as listed in Table 7.1. The letters L, M, S in the sample names in the Table stand for Large, Medium and Small and refer to the SiO_x layer thickness provided explicitly in the 2nd column. The number in the sample names refers to the oxygen-to-silicon content ratio x in the original SiO_x layers. The thickness of the SiO_2 interlayers was set to 4 nm for all the samples. We studied samples with 4 different SiO_x stoichiometries and 3 layer thicknesses (Table 7.1)

Sample	SiO _x layer properties		EFTEM				Optical properties	
	L _{layer} (nm)*	x*	S _{area} * (%)	S _d (%)	⟨d⟩* (nm)	⟨d⟩ _{d²} (nm)	Transm. (%)	α (cm ⁻¹)
L93	5.0	0.93	30	20	3.4	4.7	41	41000
M100	3.5	1.00	Data not available				79	11000
M93	3.5	0.93	17.7	11.8	2.6	3.0	70	19000
M85	3.5	0.85	22.3	14.9	3.0	3.6	73	16000
M64	3.5	0.64	24.6	16.4	3.2	4.4	52	41000
S93	2.0	0.93	Data not available				83	12000

*Values are taken from ref. [106] that deals with these very samples.
(Selection from Table I. in [46])

Table 7.1 Properties of investigated Si-NC/SiO₂ superlattices.

Fig. 7.1 shows EFTEM images of single-layer samples with analogous properties (a single annealed SiO_x layer between SiO₂ substrate and SiO₂ overlayer [105]). The observed Si NCs have shape of solidified droplets. At low Si concentration (Fig. 7.1(c)), individual NCs are isolated and relatively round. With increasing Si content (Fig. 7.1(d,e)) the initial droplets are formed nearer to each other and tend to merge together, forming larger and less regularly shaped NCs. Increase of the SiO_x layer thickness (from Fig. 7.1(c) to Fig. 7.1(b)) allows formation of precipitates with larger dimensions that tend to merge already at relatively low Si concentration.



(Selection from: (a) Fig. 3.11 in [107], (b-e) Fig. 4 in [105])

Fig. 7.1 Examples of EFTEM images of samples with nominally the same properties as the samples studied in this work with the following thicknesses and compositions of the SiO_x layer: (a) side view of 5 bilayers of 4 nm SiO₂/3.5 nm SiO_{0.93} ~ M93, (b-e) top view of single-layer samples: (b) 4.5 nm, SiO_{0.93} ~ L93, (c) 3.5 nm, SiO_{0.93} ~ M93, (d) 3.5 nm, SiO_{0.85} ~ M85, (e) 3.5 nm, SiO_{0.64} ~ M64. White lines indicate larger clusters of NCs.

From the EFTEM images, the mean NC diameter ⟨d⟩ and NC areal filling fraction S_{area} were determined. [107] See Fig. 7.2 for examples of NC diameter distributions and the EFTEM section in Table 7.1 for the results. The volume filling fractions were calculated as S_d = 2S_{area}/3, based on the assumption that the NCs are

approximately spherical. The diameter distribution histograms based on the number of NCs with the given lateral size in the EFTEM images (upper panel in Fig. 7.2) were weighted by the square of the diameter to obtain volume distribution of corresponding NC cross-section functions (lower panel in Fig. 7.2). In fact, the vertical size of the nanocrystals is assumed to be imposed by the SiO_x layer thickness for a given sample and does not change the volume distribution histogram.

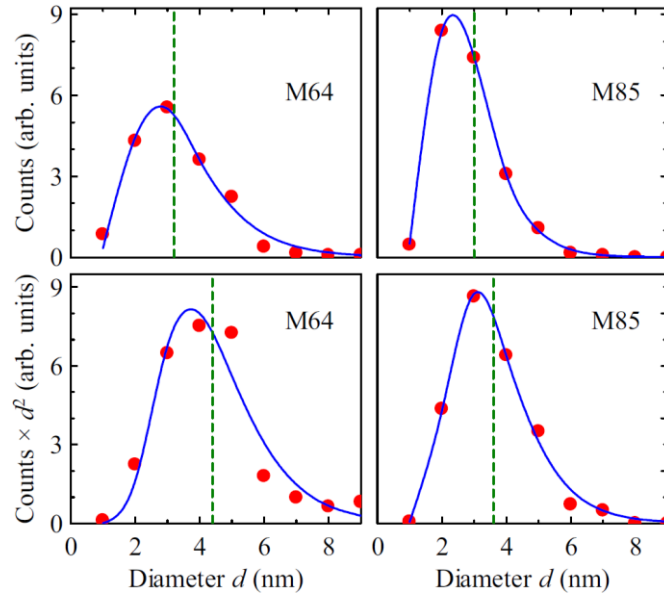


(FIG. 1. in [46])

Fig. 7.2 Examples of distributions of NC sizes. *Points*: distributions determined from EFTEM data, *solid blue lines*: fit with log-normal probability distribution, *dashed green verticals*: mean values $\langle d \rangle$, $\langle d \rangle_{d^2}$.

In order to determine the (photo)carrier concentration in NCs and the resulting depth-profile of the effective conductivity (cf. Fig. 5.1) the effective absorption coefficient of each sample had to be assessed. This was achieved by measuring the power of the pump beam transmitted through each sample (column Transm. in Table 7.1). The absorption coefficient was then simply calculated, taking into account the surface reflectance, which was measured to be ~4% for all samples. The resulting α of several 10^4 cm^{-1} is well below the absorption coefficient of bulk silicon, $\alpha_{\text{Si}} = 7 \times 10^4 \text{ cm}^{-1}$ at 400 nm.

From the point of view of radiation at 400 nm, the sample consisting of nanocrystals with a size of a few nm can be still described by an effective medium model. For this reason we employed the Maxwell Garnett EMT (3.15) to relate the effective absorption coefficient of the sample α to the intrinsic absorption of individual nanocrystals α_{Si} . For this evaluation we use the filling fractions s from Table 7.1, the shape factor $K = 2$ and the permittivities, which enter the Maxwell Garnett formula read:

$$\begin{aligned}
\varepsilon_p &\equiv \varepsilon_{\text{Si}}(400 \text{ nm}) = \left(n_{\text{Si}} + i \frac{\lambda}{4\pi} \alpha_{\text{Si}} \right)^2, \\
\varepsilon_m &\equiv \varepsilon_{\text{SiO}_2}(400 \text{ nm}) = 2.15, \\
\varepsilon &\equiv \varepsilon_{\text{eff}}(400 \text{ nm}) = \left(n + i \frac{\lambda}{4\pi} \alpha \right)^2,
\end{aligned} \tag{7.2}$$

where $n_{\text{Si}} \approx 5$. The Maxwell Garnett formula (3.15) provides α only in the order of 10^3 cm^{-1} . To obtain the 10 times higher measured value of α , the NC intrinsic absorption coefficient of the nanocrystals α^{mic} would have to be $\sim 100 \times \alpha_{\text{Si}}$. As we do not find any justification for such a high value of α^{mic} , we attribute the increased effective absorption coefficient of the sample to other absorption centers that do not produce mobile photocarriers, such as amorphous Si, compounds with residual nitrogen (present in the SiO_x layers from the deposition source reactants) or surface states. In the THz photoconductivity analysis below, we calculate the carrier density in the NCs using $\alpha^{\text{mic}} = \alpha_{\text{Si}}$ and with the quantum yield $\xi = 1$.

7.2. THz photoconductivity

The samples were oriented perpendicular to the THz beam in our setup as usual. The in-plane photoconductivity of the NC layers is thus measured, due to the transversal polarization of the probe THz pulses. The charge transport perpendicular to the superlattices was studied by conventional techniques in [108,109]. We used excitation at 400 nm with fluences between 9.0×10^{12} and 6.3×10^{14} photons/cm² and the samples were kept at room temperature for all the measurements.

Let us first shortly refer to Fig. 7.3, showing in symbols the experimental THz photoconductivity spectra, to provide motivation for the fitting model introduced below. All samples exhibit the capacitive type of response with an increasing real part and a negative imaginary part. The normalized transient transmittance increases with decreasing excitation density which clearly means that depolarization fields alter the response and that an EMT must be implemented in the data evaluation.

The linear regime of the effective response was achieved only in the silicon-richest sample M64. The green symbols plotted in Fig. 7.3(a) correspond to the lowest photoexcitation density and the blue symbols correspond to an about four times higher density. The data show an identical behavior below 1 THz; some deviations in the real part of these two curves are observed; we attribute this seeming decrease of the green spectrum with respect to the blue one to increased experimental errors for such low carrier densities. (Note that the green spectrum corresponds to the measurement taking 15 hours.) The fact that these two spectra are identical within the statistical errors means that they are not affected by depolarization fields, thanks to the achieved low carrier densities. This means that the observed capacitive type of response is also characteristic to the microscopic transport, i.e. charge carriers are

substantially confined inside the nanocrystals. Similar qualitative behavior is expected also in samples with lower Si content.

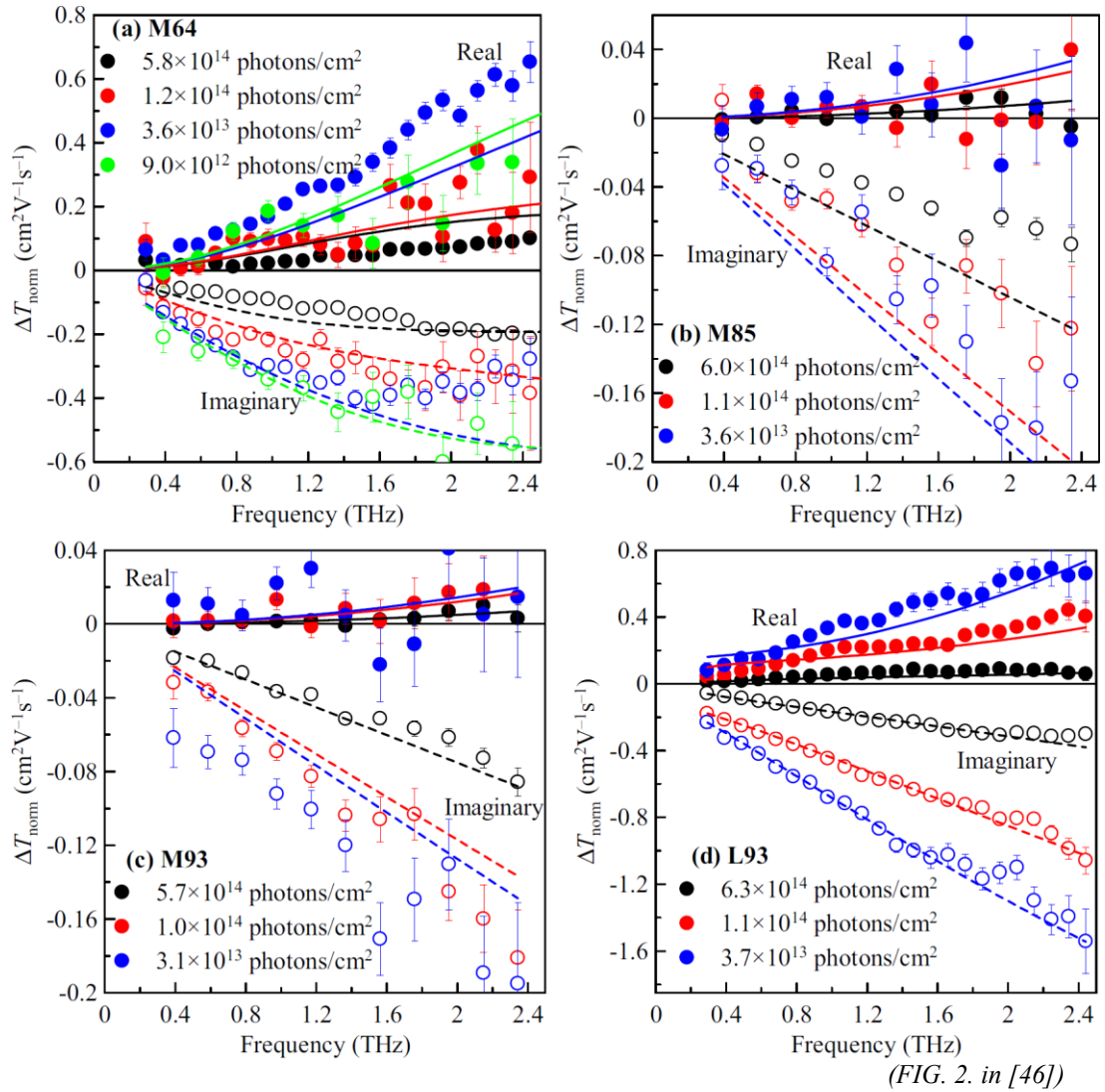


Fig. 7.3 Examples of THz photoconductivity spectra of NC-Si/SiO₂ superlattices, *symbols*: measured 10 ps after photoexcitation with indicated photon fluences at 400 nm, *lines*: calculated according to the fitting model described below.

Lines in Fig. 7.3 show the response calculated with the following fitting model:

1. The Monte Carlo method (Section 3.5) was used to calculate the model spectra of room-temperature microscopic mobility $\mu_d(\omega)$ of carriers confined in spherical NCs with diameter d fixed to the value $\langle d \rangle_d$ as obtained for each sample from the EFTEM distributions (Fig. 7.2 and Table 7.1). The mean value of area-weighted NC diameters $\langle d \rangle_d$ was used instead of the mean value of NC diameters $\langle d \rangle$ because the contribution to

the total photoconductivity of the sample is proportional to the volume of the NCs, rather than to their count. The fitting parameters of the Monte Carlo calculation were the bulk scattering time τ_s and the probability of inter-NC transport $p_{F,d}$.

2. It was already pointed out that in some samples, the NCs tend to merge into clusters of various sizes. In the cases where the presence of such clusters seems justifiable, we approximate their contribution to the total response by the mobility spectrum $\mu_\delta(\omega)$. This mobility is calculated again with the Monte Carlo method for carriers confined in spherical nanocrystals of a diameter $\delta > d$ with a given probability of inter-cluster transport $p_{F,\delta}$. The diameter δ is a fitting parameter, in contrast to d . By adjusting δ to get the best fit of the experimental data, we aim to find the average size of the clusters in the given sample.
3. The theoretical normalized transient transmittance of the thin film sample containing nanocrystals with diameters d and δ , both with a possibly percolated (5.20) and non-percolated (5.38) response contribution, was calculated:

$$\Delta T_{\text{norm}} = \sum_{i=d,\delta} \left[\frac{V_i}{\alpha} + B_i \frac{\text{Ln}(1+Z_i) - \text{Ln}(1+Z_i \exp(-\alpha L))}{Z_i} \right] \Delta \sigma_{0,i}^{\text{mic}}(\omega), \quad (7.3)$$

with

$$\Delta \sigma_{0,i}^{\text{mic}}(\omega) = e \alpha^{\text{mic}} \phi \zeta \mu_i(\omega) \quad (7.4)$$

and

$$Z_i(\omega) \equiv \frac{i D_i \Delta \sigma_{0,i}^{\text{mic}}(\omega)}{\omega \varepsilon_0} \quad (7.5)$$

The morphology factors of non-percolated inclusions B_i , D_i were defined according to the Maxwell Garnett EMT (4.9,4.10) as we assume that the MG approximation that was derived for isolated inclusions does hold also for samples with a very low levels of percolation:

$$B_i = \frac{\varepsilon_{\text{SiO}_2}(1+s_i K) - \varepsilon(1-s_i)}{\varepsilon_{\text{SiO}_2}(s_i + K) + \varepsilon_{\text{Si}}(1-s_i)}, \quad (7.6)$$

$$D_i = \frac{(1-s_i)}{\varepsilon_{\text{SiO}_2}(s_i + K) + \varepsilon_{\text{Si}}(1-s_i)}. \quad (7.7)$$

The steady-state permittivities in the THz range are $\varepsilon_{\text{Si}} = 12$ and $\varepsilon_{\text{SiO}_2} = 4$, the shape factor was fixed to $K = 2$ for spherical particles, the filling fraction of the smaller NCs s_d was fixed to the value obtained from EFTEM measurements (Table 7.1) and s_δ was a fitting parameter of the model.

4. The calculated spectra of ΔT_{norm} were fitted to the experimental ones: all the spectra measured for one sample at various excitation fluences were fitted together with a single set of parameters. The bulk scattering time τ_s was found to be larger than 100 fs in all samples and does not influence at all the response of carriers confined in NCs of given sizes in the THz frequency range. In the samples with low Si content the introduction of the clusters according to point 2 is not justified; also introduction of the clusters is not necessary to reproduce the spectra and their dependence on the photoexcitation density. For these samples (M93, M85, M100, S93) we are left with two fitting parameters: $V_d, p_{F,d}$. For samples with larger Si content or with thicker Si layers (M64, L93) where formation of clusters is more probable, fits with 6 fitting parameters were performed: $V_d, p_{F,d}, \delta, s_\delta, V_\delta$ and $p_{F,\delta}$.

7.3. Results and Discussion

The spectra of samples with lower Si content M85 and M93 (Fig. 7.3(b,c)) show a strongly capacitive type of response with a linear imaginary part and a several times lower real part. Examples of Monte-Carlo calculations of carrier mobility spectra (Fig. 7.4) in NCs of various sizes indicate that this type of spectra originates in nm-sized NCs.

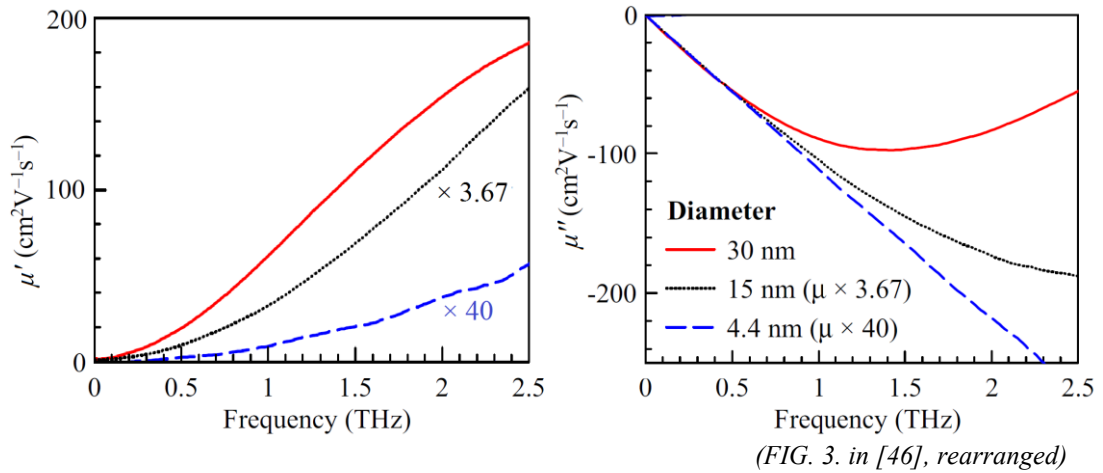


Fig. 7.4 Examples of mobility spectra of isolated Si NCs with different sizes calculated using the Monte-Carlo approach. In order to emphasize the difference in the shape of the real part, the spectra are scaled to a matching initial slope of the imaginary part.

The spectra of Si-poor samples M85 and M93 are indeed best matched by the theoretical model with NC sizes given by the EFTEM measurements, with no percolation and no connectivity among the small nanocrystals ($V_d = 0, p_F = 0$) and without any larger clusters ($s_\delta = 0$). Since there is no other adjustable parameter, we find that the VBD approximation of effective conductivity with the filling fraction s_d

obtained independently from EFTEM measurements and with Monte Carlo calculated microscopic response spectrum provides a theoretical model that agrees well with the experimental response of these samples. In other words, for samples with small nanocrystals, we are able to reproduce quantitatively the experimental spectra by using Monte Carlo and effective medium models where only the nominal parameters of the samples are introduced and none of them needs to be further adjusted by the fitting procedure. Despite the fact that there are no EFTEM data available for the samples with the lowest Si content M100 and the thinnest SiO_x layer S93, we verified by scanning over an interval of filling factors that the nature of the response of these samples is the same: the THz spectra confirm the lack of percolation ($V_d = 0$) and of inter-NC connectivity ($p_{F,d} = 0$) as well as the absence of larger clusters. See Table 7.2 for an overview of the parameters of the fits.

Sample	V_d	$p_{F,d}$	δ (nm)	s_δ/s_d^*	V_δ	$p_{F,\delta}$
L93	0	4	16	30%	0.0015	0
M100	0	0	-	0	-	-
M93	0	0	-	0	-	-
M85	0	0	-	0	-	-
M64	0	0	29	5%*	0.0012	0
S93	0	0	-	0	-	-

**Filling fraction s_δ applies to clusters with an average dimension δ .
(Selection from Table I. in [46])*

Table 7.2 THz fit parameters.

The response of the Si-richest sample M64 and the sample with the thickest SiO_x layers L93 (Fig. 7.3(a,d)) is more complex. In particular, the response is about an order of magnitude stronger than for previously discussed samples, the real part of the conductivity increases quite rapidly with frequency in the accessible spectral range, and the imaginary part is no longer strictly proportional to the frequency. Fig. 7.4 shows that such a spectrum can be explained only by the presence of a non-negligible amount of particles whose size along the polarization of the THz probe pulse is significantly larger (tens of nm). In reality, a broad distribution of shapes and sizes is expected to exist with a significant tail towards larger dimensions, similarly as observed for samples described in the previous Chapter. Indeed, the fitting model converged to non-zero values of the filling fraction s_δ of larger particles.

In fact, the samples M64 and L93 contain a similar amount of Si per layer — L93 has ~50% thicker SiO_x layers than M64, M64 has ~50% more of Si in each layer per unit thickness — and their Si filling fractions are also alike (Table 7.1). However, the experimental spectra and our fits show quite a different character of clustering of the small NCs in these two samples. The spectra of sample M64 are

then best fitted with a low concentration $s_{\delta}/s_d = 5\%$ of relatively long clusters, $\delta \approx 29$ nm. The EFTEM image in Fig. 7.1(e) shows several clusters of such length.

For sample L93 we find, in contrast, that almost 30% of Si is present in the form of relatively smaller clusters with $\delta \approx 16$ nm (Table 7.2). This means that the very long clusters (>30 nm) observed in the thick Si-poor layer in Fig. 7.1(b) are in fact not well conductive from one end to the other; instead, they are just a group of several smaller (~ 16 nm) clusters that are not well connected. Spectra and fit results of samples M64 and L93 further differ in the low-frequency conductivity: in sample L93, it slightly deviates from zero which indicates a certain possibility of long-range inter-NC charge transport — the fit converged to 4% probability of transport between adjacent NCs. This means that some of individual NCs in thick SiO_x layers are no longer perfectly isolated from each other but they form at least pairs separated by finite energy barriers (similar behavior was observed in CdS NCs prepared by chemical bath deposition in [47]).

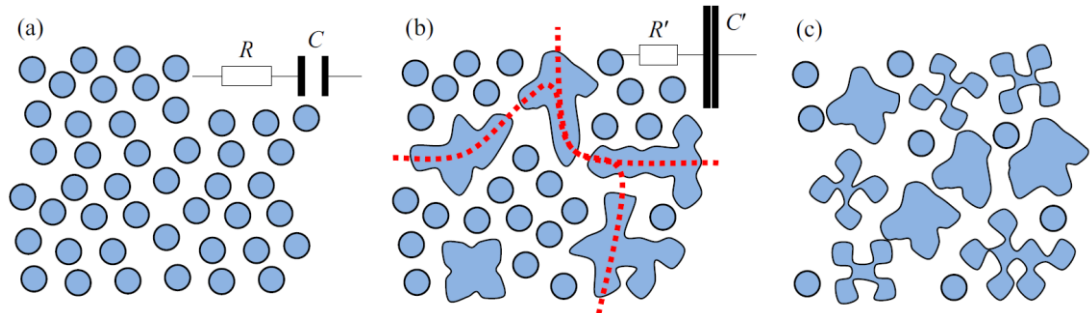


(FIG. 4. in [46])

Fig. 7.5 Scheme of the morphology of investigated samples as deduced from THz photoconductivity measurements. (a) NCs in samples S93, M93, M85, and M100 are well isolated from each other and no tendency to aggregation is observed. (b) NCs in the sample M64 form clusters; some of these clusters may form a percolation network on a medium length scale (the pathways closest to the percolation are illustrated by thick dotted lines). (c) In thick layers (L93), weakly connected NCs may develop. The electron transport among these NCs is limited. Insets: Equivalent electrical circuits of the structures.

The difference between the morphology of the two samples can be explained by different diffusivity of Si. The diffusion coefficients of atoms (Si) in a glass (SiO_2) increases with concentration of the atomic material. In the Si-richer layer (M64), atomic Si diffuses faster, clusters are formed in early stages of annealing and have more time to crystallize into well conductive objects. Si is also able to diffuse further to its target NC, resulting in wide gaps between individual precipitates as observed in Fig. 7.1(e). In a Si-poorer layer, L93, Si atoms diffuse more slowly and NCs merge into clusters in later stages of the annealing. The clusters thus probably have a lower quality (crystallinity, conductivity) of internal connectors. Si atoms also travel shorter distances during annealing and a larger amount of smaller NCs is

predominantly formed with narrower gaps between them, as seen in Fig. 7.1(b), that more probably allow inter-NC transport ($p_F \approx 4\%$). The different clustering regimes are illustrated in Fig. 7.5.

All fitting parameters are summarized in Table 7.2. The fitted percolation strengths of the clusters in both clustered samples is rather small ($V_\delta \sim 10^{-3}$), but a non-zero value is required for reproducing the fluence-independence at the smallest excitation densities when the response of the larger objects dominates. Note that, as already pointed out in [45], the non-vanishing percolation strength does not strictly mean a continuous conductive pathway through the entire sample, but only on a distance substantially longer than the size of the insulating gaps between the NCs. Morphologies with very small gaps between NCs imply a high capacitance between the photoconductive elements, and upon clustering, some of the gaps close, i.e., the capacitance effectively increases (Fig. 7.5). At high (THz) probing frequency, the impedance of the capacitor drops down and the circuit impedance is dominated by the resistance mimicking the percolation.

The microscopic picture of the charge carrier transport in the studied systems is schematically summarized in Fig. 7.5. We stress that the linear polarization of the THz pulse is parallel with the sample surface which means that only in-plane conductivity is probed. The conclusions on the size of aggregates and percolation strength thus apply only to lateral directions. Possible coupling among individual SiO_x layers is not encoded in our signal.

7.4. Kinetics

Spectrally averaged photoconductivity kinetics in Fig. 7.6 show the evolution of photoconductivity in its early stages. On the time scales longer than a few picoseconds, the decay can be described by a single stretched exponential. This is in agreement with the recent report on photo-initiated dynamics of identical samples studied by time-resolved absorption and luminescence [110] where the dynamics was attributed to the non-radiative bimolecular recombination of carriers in the core of Si NCs.

A notable behavior of most of the samples is the presence of a sub-picosecond decay component. This feature is particularly pronounced in samples S93 and L93. There is no pronounced excitation fluence dependence of this component (with the exception of sample S93 where the amplitude decreases with increasing excitation fluence). The decay thus cannot be due to Auger recombination, which is a strongly intensity dependent process. Since the NCs were found to be mostly isolated from each other, charge migration towards energetically favorable isolated particles as observed in [111] should not play an important role here; besides that, the sub-picosecond time scale is too short for such a process to take place. A fast initial decay component in Si NCs prepared by electrochemical etching was recently attributed to the carrier trapping at interface states [112] [37]. Also one cannot exclude the possibility that the charges are initially generated at higher energy levels

in which they are more delocalized; subsequent fast relaxation to more localized states then could manifest itself as a rapid initial drop in the photoconductivity, similarly as it has been observed in CdS NCs [47].

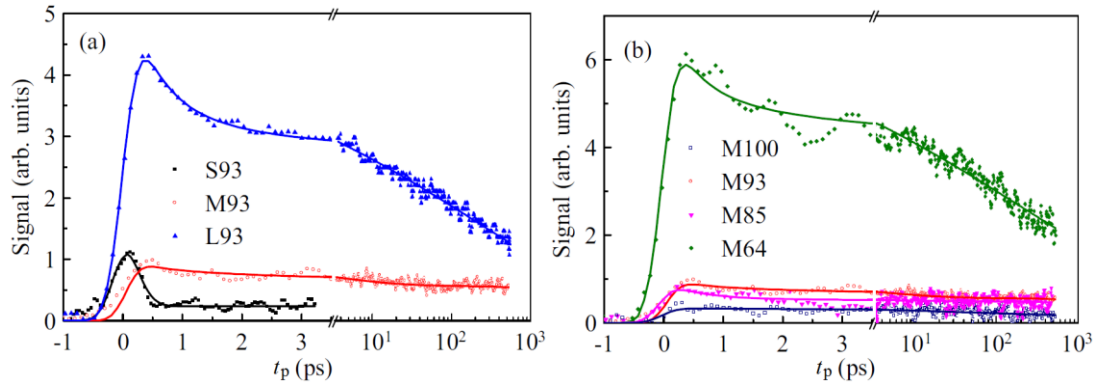


(FIG. 5. in [46])

Fig. 7.6 Transient THz kinetics scans for samples (a) with different SiO_x layer thickness and (b) with different composition x . The pump fluence in all measurements was in the range $3.1\text{--}3.6 \times 10^{13}$ photons/cm². The lines serve as guides to the eye.

7.5. Conclusion

THz photoconductivity spectra of superlattice samples of Si nanocrystals with various narrow size distributions embedded in SiO_2 matrix were measured. Spectra of the samples with small well-isolated NCs are excellently reproduced by the VBD effective medium model that incorporates microscopic carrier mobility spectra calculated by the Monte Carlo method in model NCs of given, independently measured, properties.

In samples with a higher content of Si (M64) and with thicker layers (L93), additional (tens-nm-sized) clusters with larger localization scale were identified by fits of the spectra with Monte Carlo mobility in the VBD effective medium model. These clusters form a short- or medium-range percolation network and do not possess any significant internal structure which could hinder the intracluster transport of charges. In addition, groups of weakly mutually connected nanocrystals develop in SiO_x layers with a larger thickness. A limited probability of short-range inter-NC transport was also observed in the latter sample suggests that these structures may develop at the end of the growth of individual nanocrystals inducing higher concentration of defects at the grain boundaries. The size of the observed clusters (tens of nanometers) is large enough to suppress possible effects of the strong quantum confinement.

8. Dynamics of density-dependent response in bulk rutile

Titanium dioxide is a common mineral that is characterized by a very strong electro-phonon interaction and has a relatively wide band gap of ~ 3 eV that is used e.g. in Grätzel photovoltaic cells. Outside optoelectronics, titania particles are used as one of the most common white pigments in industrial paintings, dyes and colorants thanks to the high refractive index of the material. The band gap at the high-energy edge of the visible spectrum makes it also an effective UV filter that is transparent in the visible range and used in most sun screening lotions together with ZnO.

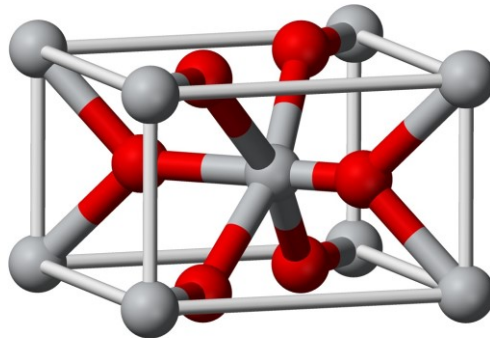


Fig. 8.1 The tetragonal unit cell of rutile. Oxygen atoms are red; titanium atoms are grey. *C*-axis is vertical in the figure. [113]

Rutile (Fig. 8.1) is the most common natural crystallographic form of titanium dioxide. In this Chapter, we investigate THz photoconductivity of a monocrystal rutile slab at temperatures between 10 and 300 K in the first 600 ps after over-the-band-gap excitation with photon fluences changing over 2 orders of magnitude. The main motivation of these measurements was to obtain independent data on carrier transport in bulk rutile as a reference for the previous and further investigations of TiO₂ nanosystems in our group. The following sections present: an in-depth time- and density-resolved study of carrier transport at low temperatures; a short section on the temperature dependence of photocarrier conductivity; the temperature dependence of electron-hole recombination as observed in OTP kinetics scans; and lastly the transient photo-induced change of (multi)THz permittivity of rutile at room temperature. Most of the results were published recently in [114].

Our sample was a 10×6 mm² large, 260 μ m thick, (001)-oriented slab of rutile single crystal provided by Patrick Mounaix and Mario Maglione. Fig. 8.2 shows the dielectric function of our sample at various temperatures that was measured by steady-state THz spectroscopy (cf. Section 2.2) in order to characterize the dispersion of the refractive index needed to calculate correctly the spectra of normalized transient transmittance (2.10). With increasing temperature, we observe a dispersion

and an absorption tail of the lowest-frequency polar phonon at 183 cm^{-1} [115]; the phonon damping progressively decreases as the temperature is lowered.

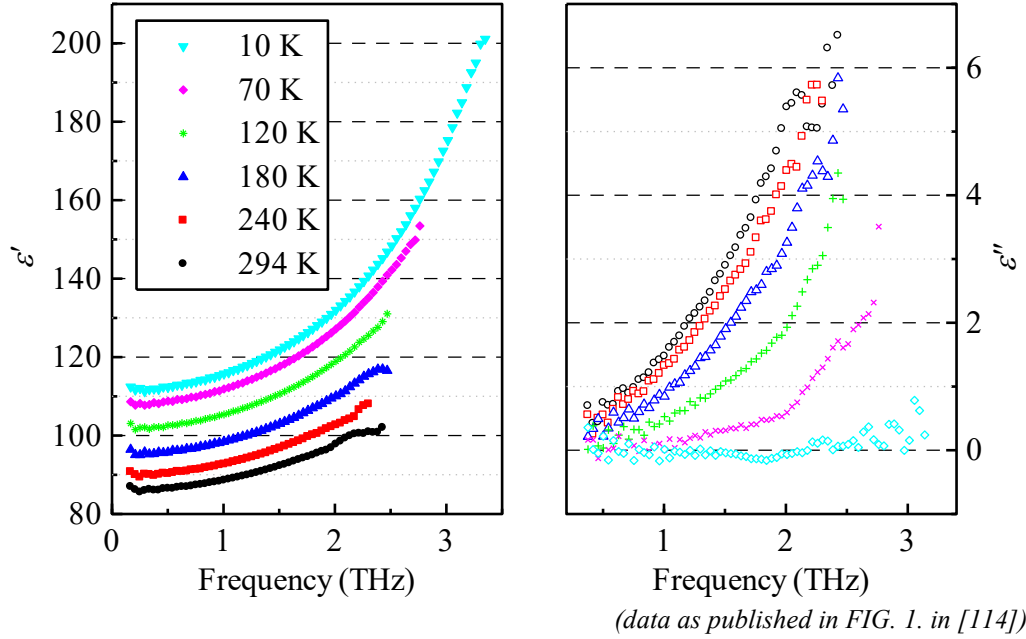


Fig. 8.2 Dielectric function of our sample of rutile ($E \perp c$) at various temperatures.

Property		Value	Reference
Crystallography	unit cell type	body-centered tetragonal	
	lattice constant	$a = b = 4.584 \text{ \AA}$ $c = 2.953 \text{ \AA}$	[116]
Pump light (266 nm, $E \perp c$)	n'	2.5	Fig. 15 in [117]
	n''	1.8	Fig. 16 in [117]
	R	34%	Fig. 13 in [117]
	α	$8.5 \times 10^5 \text{ cm}^{-1}$	$\alpha = 4\pi \cdot n'' / \lambda$
	penetration depth	11.8 nm	$1/\alpha$

Table 8.1 Characteristics of bulk rutile.

8.1. Picosecond dynamics of charge transport at low temperatures

In a previous OPTP work, Hendry et al. [118] reported a decrease of the scattering time of charge carriers in rutile with increasing excitation density, as inferred from fits of THz photoconductivity spectra with the Drude model. The evaluation in [118] neglected the depth-inhomogeneity of excitation that is due to a

high absorption coefficient of the used 266 nm (4.7 eV) excitation light. We reviewed the proposed scattering model in similar experimental conditions on a deeper level by taking into account:

- the exact depth profile of photocarrier density and
- the temporal evolution of the density profile due to carrier diffusion and recombination.

For this purpose, we measured the THz photoconductive response at various pump–probe delays between 10 and 610 ps after photoexcitation with 266 nm light at several excitation fluences between 2×10^{12} and 2.5×10^{14} photons/cm². Then we employed numerical solution of carrier diffusion equations through this time interval. This plasma diffusion model was employed with data measured at 10 and 70 K where effects of the diffusion are most pronounced.

8.1.1. Published scattering model and data comparison

Hendry et al. [118] measured the transient THz photoconductivity of (001)-rutile at a temperature of 30 K, solely at $t_p = 10$ ps, using the same excitation wavelength as we did, with fluences between 4×10^{12} and 6×10^{14} ph/cm². They fitted the transient transmittance spectra with Drude-type conductivity in the form [118]

$$\Delta\sigma^{\text{av}}(\omega) = N^{\text{av}} \frac{e^2 \tau^{\text{av}}}{m^*} \frac{1}{(1 - i\omega\tau^{\text{av}})}, \quad (8.1)$$

where the superscript “av” was used to emphasize that $\Delta\sigma^{\text{av}}(\omega)$ represents an averaged photoconductivity for all photocarriers across the excited region. The average excitation density is $N^{\text{av}} \approx 0.63\alpha\phi$ (cf. footnote 19 in [118]). The fitted value of τ^{av} is characteristic to the shape and amplitude of the measured photoconductivity spectrum, but it is *not* meant as the arithmetic mean of the scattering times of the carriers distributed in the sample with a varying concentration. It is connected the actual distribution of density-dependent carrier scattering times in a complex manner that has not been formulated. We refer to (8.1) as to the single-component model. Fig. 8.3 shows the $\tau^{\text{av}}(N^{\text{av}})$ dependence in empty boxes together with data obtained from our measurements by the same evaluation method (full boxes).

A very good correspondence between our and their results can be seen, indicating that samples of similar quality were used. Hendry et al. fitted the dependence of the single-component-fit carrier scattering rate on the average carrier density N^{av} with the following model:

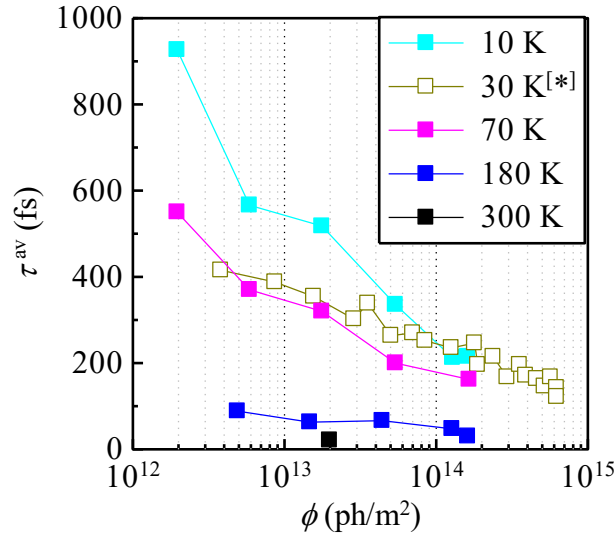
$$\frac{1}{\tau^{\text{av}}(N^{\text{av}})} = \frac{1}{\tau_0} + aN^{\text{av}} + b^3\sqrt{N^{\text{av}}}, \quad (8.2)$$

where τ_0 stands for the scattering time in the low-density limit and a and b are the proportionality constants of the electron–hole scattering and of an enhanced scattering of carriers on acoustic phonons, respectively. The latter effect was reasoned as follows: carrier mean free path between collisions on acoustic phonons is

constant at a given temperature [119] and the velocity of mobile carriers obeys the Fermi distribution $\propto N^{1/3}$ at increased carrier densities due to the band filling. At low densities, the carrier velocity obeys the Maxwell-Boltzmann distribution and the value of b can be estimated from the scattering time of carriers on acoustic phonons in the low density limit τ_A [118],

$$b = \frac{\hbar \sqrt[3]{3\pi^2}}{m^{\text{DOS}} \tau_A \sqrt{3k_B T / m^{\text{DOS}}}} \quad (8.3)$$

where m^{DOS} is the density-of-states mass. In another paper, Hendry et al. have shown that in undoped rutile at low temperatures, scattering on acoustic phonons is the dominant mechanism and τ_A can be in this case identified with τ_0 . [96]



(adaptation of FIG. 4 in [114])

Fig. 8.3 Single-component scattering times in a 260 μm thick rutile ($E \perp c$) sample 10 ps after photoexcitation at 266 nm. [*]30 K data as published by Hendry et al. in [118].

8.1.2. The general plasma-diffusion model

We show in the following that both electrons and holes play an important role in the measured THz photoconductivity spectra at low temperatures. For this reason, we explicitly distinguish between electrons and holes (subscripts e, h, respectively) in the following equations. The depth profile of the carrier density initially follows the absorbed photon density (Lambert-Beer absorption law):

$$N_i(z,0) = \alpha \phi \exp(-\alpha z); \quad i = e, h, \quad (8.4)$$

Since bimolecular (electron-hole) recombination is expected to be the dominant process of mobile carrier loss on the subnanosecond time scale at high carrier densities, we describe the evolution of the carrier density in time and space by using the second Fick's law combined with a bimolecular recombination term

$$\frac{\partial N_i(z, t_p)}{\partial t_p} = D_A(N_i) \frac{\partial^2 N_i(z, t_p)}{\partial z^2} - B N_e(z, t_p) N_h(z, t_p), \quad i = e, h, \quad (8.5)$$

where B is the bimolecular recombination constant and $D_A(N_i)$ is the ambipolar diffusion coefficient

$$D_A = \frac{D_e \mu_h + D_h \mu_e}{\mu_e + \mu_h}, \quad (8.6)$$

which directs diffusion of both electrons and holes at the same rate. This is because the electrostatic attraction between the two carrier types prevents the more mobile one from diffusing away from the less mobile one. Diffusion coefficients $D_{e,h}$ of electrons and holes, respectively, are connected to their DC mobilities $\mu_{e,h}$ at given carrier densities via the Einstein relation

$$D_{e,h} = \frac{\mu_{e,h} k_B T}{e}. \quad (8.7)$$

(Equal temperature of electrons and holes is assumed after the first few picoseconds after photoexcitation when the thermalization is completed.) The ambipolar character of diffusion together with the dominant character of the bimolecular recombination imply that in our case, $t_p \lesssim 600$ ps, we can consider the concentrations of electrons and holes in the sample as identical: $N(z, t_p) \equiv N_e(z, t_p) = N_h(z, t_p)$.

Carrier mobilities in the bulk crystal are expected to be Drude-like and to depend on the carrier density through the scattering time

$$\mu_i(\omega; N) = \frac{e \tau_i(N)}{m_i^*} \frac{1}{1 - i\omega \tau_i(N)}, \quad i = e, h, \quad (8.8)$$

which we assess independently for electrons and holes in contrast to (8.2):

$$\frac{1}{\tau_i(N)} = \frac{1}{\tau_{0i}} + aN + b_i N^{1/3}, \quad i = e, h, \quad (8.9)$$

because electrons and holes are not expected to have the same low-density scattering time τ_{0i} and carrier-phonon scattering rate b_i . The density-dependent ambipolar diffusion coefficient is then:

$$\frac{1}{D_A(N)} = \frac{1}{2k_B T} \left[\left(\frac{m_e^*}{\tau_{0e}} + \frac{m_h^*}{\tau_{0h}} \right) + a(m_e^* + m_h^*)N + (b_e m_e^* + b_h m_h^*)N^{1/3} \right]. \quad (8.10)$$

After solving numerically the diffusion equations (8.5) with density dependent ambipolar diffusion coefficient (8.10), our fitting procedure integrates carrier mobilities (8.8) at given times t_p over the depth (cf. transient sheet conductivity 5.41) and in this manner we obtain the model spectra of normalized transient transmittance:

$$\Delta T_{\text{norm}}(\omega, t_p) = \frac{1}{\alpha \phi} \int_0^L \sum_{i=e,h} \mu_i[\omega, N(z, t_p)] N(z, t_p) dz. \quad (8.11)$$

Here L is the sample thickness and, in our case, $\alpha L \gg \gg 1$. A single set of parameters m_e^* , m_h^* , τ_{0e} , τ_{0h} , a , b_e , b_h , B of the calculated spectra is iterated by the simplex downhill method following the criterion of least squares to obtain the best fit to a set of spectra of ΔT_{norm} measured at different excitation densities and pump–probe delays.

8.1.3. Kinetics and simplified analysis

Fig. 8.4 shows the transient THz kinetics of the response of photocarriers excited with the highest fluence available in cryostat at 10 and 70 K. The time axis of the plot is shifted by 1 ps to include the instant of excitation at $t_p = 0$ ps. Immediately after that, we see an unusually slow 100 ps increase of the transient absorption at 10 K, indicating an increase of the transient conductivity of the photoexcited electron–hole plasma. Our hypothesis is that the dense carrier plasma (initial surface photocarrier density is $1.3 \times 10^{20} \text{ cm}^{-3}$) expands from the 12 nm absorption layer deeper into the sample by diffusion. This leads to a decrease of the carrier density, accompanied by an increase of the scattering time (8.2) and an increase of the amplitude of the average Drude conductivity (8.1). At 70 K this effect is weaker, yet it keeps up the transient signal at a constant level for the first 100 ps.

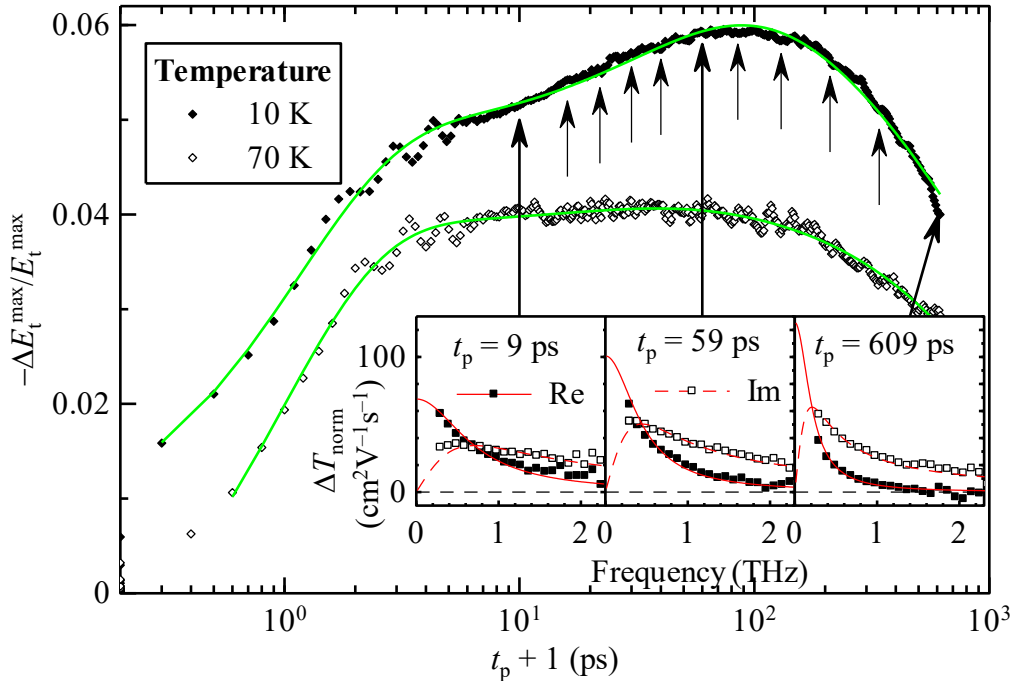


Fig. 8.4 Transient THz kinetics of rutile ($E \perp c$) after excitation with $1.6 \times 10^{14} \text{ photons/cm}^2$ at 266 nm at 10 and 70 K. *Points*: measured data; *line*: guide to the eye. *Arrows*: time delays at which THz photoconductivity spectra was measured. *Inset, boxes*: measured ΔT_{norm} spectra; *lines*: fit with single-component model (8.1).

A slower process of carrier recombination decreases the carrier density, too, but it also reduces the total number of conductive carriers at the same time. This decrease of the conductivity due to the loss of conductive carriers takes over at approximately $t_p \approx 100$ ps and a monotonous decrease of transient absorption is observed thereafter.*

Arrows in Fig. 8.4 indicate time delays at which transient THz waveforms were measured to obtain spectra of normalized transient transmittance. Three selected spectra are shown for 10 K along with their fits by the single-component Drude model in the inset of Fig. 8.4. An increase of the scattering time (narrowing of the resonance at zero frequency) is clearly seen. The amplitude of the fit with the single-component Drude model cannot be analyzed straightforwardly, as it includes the increase of the scattering time and averaging over a decreasing number of recombining carriers. Before presenting quantitative results of our fits with the plasma-diffusion model introduced in the Subsection 8.1.4, we present a simpler model that clearly justifies our interpretation of the observed evolution of the OPTP kinetics and spectra.

Two-component Drude model

Within this model we assume that the photoexcited part of the sample consists of two regions: a high-density plasma region (close to the surface, subscript H) and a low-density plasma region (deeper in the sample, subscript L). The carrier response in both regions is considered Drude-like and the total THz signal equals the sum of these two contributions:

$$\Delta T_{\text{norm}}(\omega, t_p) = \zeta_H(t_p) \frac{e \tau_H(t_p)}{m^*} \frac{1}{1 - i\omega \tau_H(t_p)} + \zeta_L(t_p) \frac{e \tau_0}{m^*} \frac{1}{1 - i\omega \tau_0}, \quad (8.12)$$

with a constant low-density scattering time τ_0 in the low-density region and a time-dependent scattering time τ_H that presents an average (again *not* in the exact meaning of an arithmetic mean) over scattering times of carriers that have not yet reached the low-density region. The process of plasma expansion (diffusion of carriers between the two regions) is taken into account by the fractions ζ_H and ζ_L of carriers in the two regions that are considered as independent quantities evolving in time. In a good quality bulk sample, as this one, we presume unitary quantum yield at the beginning $\zeta_H(0) + \zeta_L(0) = 1$. Eleven experimental spectra measured at 10 K at the highest pump fluence at delays indicated in Fig. 8.4 were fitted with (8.12). The quality of the fits is slightly superior to the fit with the general plasma-diffusion model, which is presented afterwards, but let us remind that here the fitting parameters ζ_H , ζ_L , τ_H are independent for each spectrum and τ_0 is the only global

* A minor oscillation that occurs in the transient kinetics between $t_p = 2$ and 6 ps does not originate in the sample. It was checked that similarly as in the case of nanocrystalline Si (see Fig. 6.6) we observed here a small THz signal generated unintentionally in the sapphire windows of the cryostat by intense pump pulses.

parameter (common for all the spectra). Fig. 8.5 displays the resulting parameters versus the pump–probe delay.

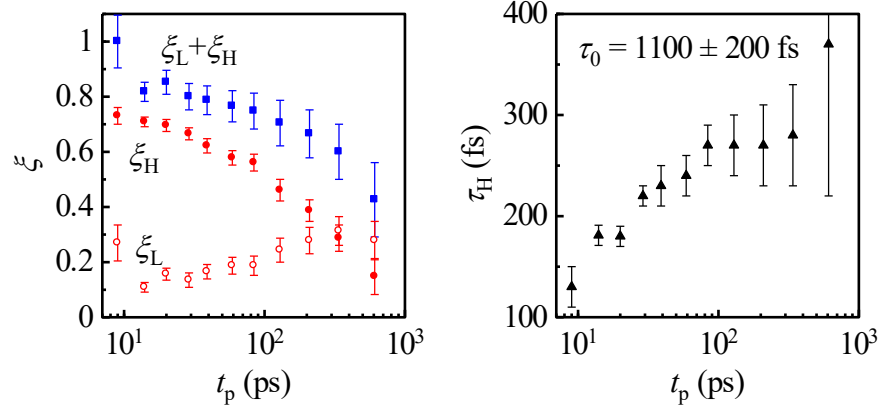


Fig. 8.5 Parameters of a fit by the two-component Drude model (8.12) of ΔT_{norm} spectra of rutile at 10 K at the highest available excitation fluence as a function of the pump–probe delay.

The sum $\zeta_{\text{H}} + \zeta_{\text{L}}$ represents the decay of the total carrier number by recombination while the individual variations of ζ_{L} and ζ_{H} involve the transfer of carriers from the high-density region to the low-density one. The increase of τ_{H} with the pump–probe delay towards τ_0 qualitatively indicates that the average carrier density in the high-density region decreases with time. For longer times, τ_{H} must inevitably approach τ_0 and the response will tend to a single-component one: this effect along with the decrease of ζ_{H} leads to the growing error bars in Fig. 8.5.

Apparently, the carrier recombination is a process occurring on a comparable time scale as the plasma expansion and homogenization. All these findings clearly support our hypothesis of the importance of the competition between the carrier diffusion and recombination for the analysis of our spectra. We thus now proceed to the discussion of the plasma-diffusion model introduced in the theoretical part of this section.

8.1.4. Results and discussion

The general plasma diffusion model was applied to a set of 23 complex THz spectra of normalized transient transmittance at 10 K:

- 11 spectra measured at the maximum fluence of 1.6×10^{14} photons/cm² for approximately logarithmically increasing pump–probe delays between 9 and 600 ps (arrows in Fig. 8.4, evaluated also with the two-component model);
- 8 spectra measured at a decreased fluence of 1.3×10^{14} photons/cm², with slightly longer pump–probe delay steps between 11 and 600 ps;
- 4 spectra at $t = 10$ ps at further decreased fluences of 5.4×10^{13} , 1.8×10^{13} , 5.9×10^{12} and 2.0×10^{12} photons/cm².

A set of 15 spectra was evaluated at 70 K:

- 10 spectra measured at the maximum fluence for approximately logarithmically increasing pump–probe delays between 11 and 600 ps;
- 5 spectra at $t = 10$ ps at decreased fluences of 5.4×10^{13} , 1.7×10^{13} , 5.9×10^{12} and 2.0×10^{12} photons/cm².

A global fit of all spectra at one temperature with a single set of parameters was performed. The fitting procedure optimized the parameters by the downhill simplex method following the criterion of least squares in the frequency interval 0.19–1.9 THz over all spectra. (The experimental data showed the lowest experimental errors in this interval.) The global fit has at most 8 free parameters (m_e^* , m_h^* , τ_{0e} , τ_{0h} , a , b_e , b_h , B). Below we present the results of the fits and discuss additional constraints which we imposed on the parameters.

Polaron effective masses

Up to now, we have not distinguished between electrons and holes in the interpretation of the measured spectra of THz photoconductivity. Our plasma-diffusion model indeed discriminates the two carrier types because it stems from two presumptions that are essentially connected to two carrier type of opposite polarities: (i) diffusion has ambipolar character due to Coulomb attraction and (ii) carrier loss is dominantly due to bimolecular recombination. This excludes the possibility that the sum fit (8.11) modelled two regimes of one charge carriers type e.g. in two different valence or conduction bands or valleys. Moreover, the second lowest conduction band and the second highest valence band are separated from the respective edge band in rutile by more than 0.3 eV. [120]

However, THz spectroscopy cannot tell which model carrier mass and scattering parameters are connected to which carrier polarity because mobility of both electrons and holes is additive in the measured spectra (8.11). The carrier effective mass m^* in the two-component model (8.12) is understood as the reduced electron–hole mass and the obtained scattering times thus also represent an unspecified averaging over the two carrier types. The same can be said about the analysis through the single-component Drude model in Subsection 8.1.1 (Fig. 8.3). The following review of published carrier masses in rutile shows that we cannot unambiguously attribute the lighter carrier mass in the model to electron as usual in most semiconductors.

In rutile the charge carrier mass is increased due to the formation of the polaron [118] and, consequently, in the following text we argue in terms of the electron polaron and hole polaron effective masses. In some older works it has been argued that the effective mass of hole polarons is much smaller than the effective mass of electron polarons ($m_h^* < m_e$, $m_e^* \gg m_e$) [121,122], where m_e is the electron rest mass. Later on, it was shown by transient diffraction grating experiments [123] that the effective mass of the hole polarons in TiO₂ single crystals is $m_h^* > 3 m_e$. The value of effective mass of electron polarons was then frequently reported to be in the

range of $m_e^* \approx (5-13) m_e$ as summarized in [124,125]. It is also interesting to note that the effective electron mass as inferred from experiments seems to be larger than the effective hole mass in the anatase form of TiO_2 [124,125]. Recent first principle calculations within the local density approximation [126] and taking into account various corrections [120] determine the band structure of rutile and predict the band mass of electrons and holes and their anisotropy. The Fröhlich electron–phonon coupling theory then provides the electron and hole polaron effective masses in the ab -plane of $2.4 m_e$ and $8 m_e$, respectively [120], i.e. the hole polaron being heavier. Previously, Glassford and Chelikowsky [127] found very similar band masses of the charge carriers in rutile; however, a follow-up study, carried out by Hendry et al. [128] within the Feynman polaron theory, determines the electron polaron mass in the ab -plane to be as high as $15 m_e$. As one can see, distinguishing between the electron and the hole based on their effective conduction (polaron) masses according to the literature also does not provide an unambiguous answer. For this reason, we refer in the following discussion to the “lighter” polaron (index Lt) and the “heavier” polaron (index Hv) instead of hole and electron polarons, wherever we refer to them separately, and we keep in mind that these two polarons are related to opposite charges.

Three variants of the general plasma-diffusion model were tested out with the data at 10 K to check the necessity of distinguishing between the two carrier types: (i) the approximation of one polaron type being much lighter than the other ($m_{\text{Hv}}^* \gg m_{\text{Lt}}^*$), (ii) the approximation of electrons and holes having the same masses and scattering properties ($\mu_e = \mu_h$). (iii) Finally, the general case of independent masses and scattering times of electrons and holes was modelled both with data measured at 10 and at 70 K.

Assumption of one light and mobile polaron type

First, we examined the assumption that one carrier type has a considerably lower effective mass than the other, $m_{\text{Hv}}^* \gg m_{\text{Lt}}^*$, which is a usual assumption in many classic semiconductors with electron being the considerably lighter charge carrier. Assuming that the scattering time of both carrier types are controlled essentially by the electron–hole scattering at the present carrier densities, one also deduces that $\mu_{\text{Lt}} \gg \mu_{\text{Hv}}$ (8.8). This interpretation was also followed in [118,128]. The ΔT_{norm} spectra (8.11) then present mostly the response of the lighter polaron type while their evolution in time is determined by the heavier one. It is because the ambipolar diffusion coefficient (8.6, 8.7) in this approximation tends to:

$$D_A \approx \frac{2\mu_{\text{Hv}}k_B T}{e} = 2D_{\text{Hv}}. \quad (8.13)$$

The set of fitting parameters is then: m_{Lt}^* , $\tau_{0\text{Lt}}$, a , b_{Lt} , B and μ_{Hv} . Various combinations of the proposed scattering mechanisms were examined by fixing one of the parameters a , b_{Lt} to zero value. In some fits μ_{Hv} was considered constant and in some fits a possible dependence of μ_{Hv} on the carrier density (8.8, 8.9) was tested.

However, the heavy polaron mobility that provided the best fitting ambipolar diffusion coefficient always converged to values that were one order of magnitude higher than the mobility of the lighter polaron in the low-density regime ($e\tau_{0L}/m_{Ll}^*$). This is a contradiction with the $\mu_{Ll} \gg \mu_{Hv}$ assumption and we conclude that this approximation cannot be fulfilled consistently within the considered scattering and diffusion model.

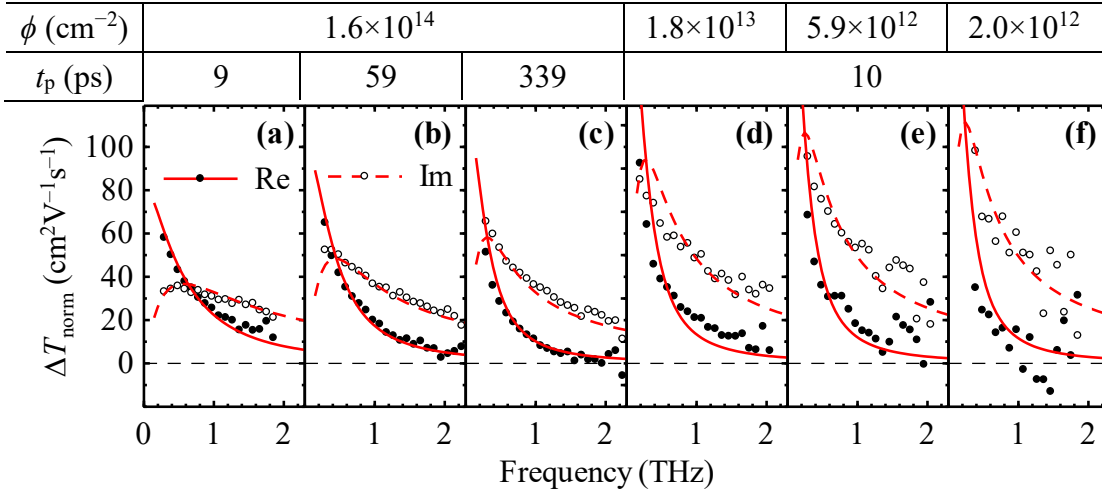


Fig. 8.6 THz photoconductivity spectra of rutile ($E \perp c$) at 10 K at selected excitation fluences and pump–probe delays (indicated above the graphs). *Symbols*: experimental data. *Lines*: global fit with plasma diffusion model in the $\mu_e = \mu_h$ approximation

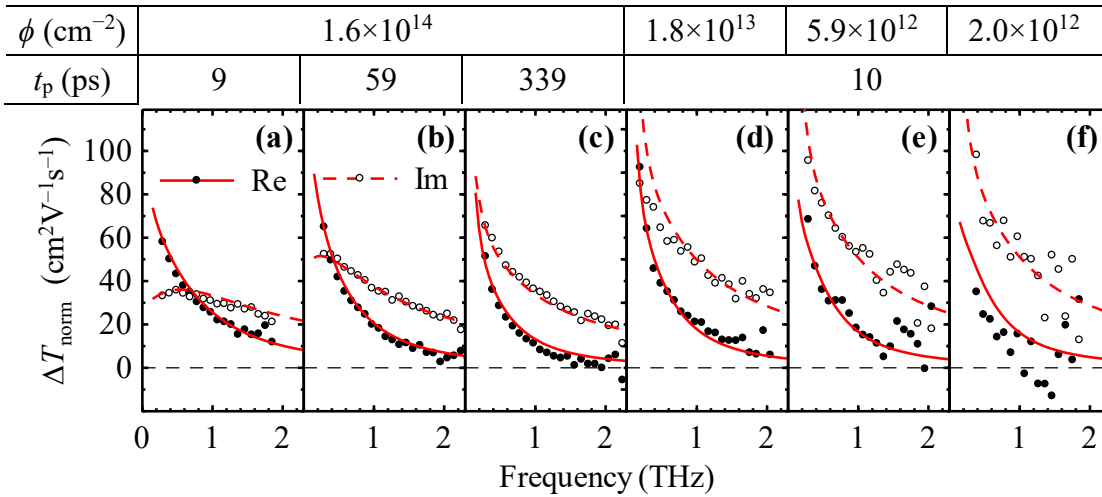


Fig. 8.7 THz photoconductivity spectra of rutile ($E \perp c$) at 10 K at selected excitation fluences and pump–probe delays (indicated above the graphs). *Symbols*: experimental data. *Lines*: global fit with the general $\mu_e \neq \mu_h$ plasma diffusion model.

Comparably mobile electrons and holes

Second, in order to reflect the encountered inconsistency of the $\mu_{\text{Lt}} \gg \mu_{\text{Hv}}$ hypothesis and keep the number of fitting parameters as low as possible, we reduced the problem to electrons and holes having the same masses and the same dependence of their scattering times on the carrier density. ΔT_{norm} then consists of two identical summands and the ambipolar diffusion coefficient is equal to $D_e = D_h$. The 5 fitting parameters are $m_e^* = m_h^*$, $\tau_{0e} = \tau_{0h}$, a , $b_e = b_h$ and B . Fig. 8.6 shows the evolution of experimental spectra and their fit with this model at selected time delays (panels a,b,c) and excitation densities (panels a,d,e,f). One can see that the model follows the time and density dependences of the normalized transient transmittance quite well. The shapes of individual spectra are not reproduced exactly, though. Parameter values retrieved from this fit are presented in the first row of Table 8.2 and discussed together with the results of the most general fits.

General electron–hole plasma model

Finally, we enabled independent fitting of all 8 available parameters: $m_{\text{Lt,Hv}}^*$, $\tau_{0\text{Lt,Hv}}$, a , $b_{\text{Lt,Hv}}$ and B . This fit yielded a 34% lower sum of least squares at 10 K than the simplified $\mu_e = \mu_h$ model above (compare lines in Fig. 8.7 and Fig. 8.6, note fit–data matching e.g. in the low-frequency section of the imaginary part in most panels) and thus confirmed the need to consider both electron and hole polarons separately in the observed response.

The converged values of parameters of the general plasma-diffusion model at 10 and 70 K are given in the “ $\mu_e \neq \mu_h$ ” rows of Table 8.2. One can see that the masses of electron and hole polarons exhibit a low ratio of ~ 1.6 (as expected after a contradiction with the $m_{\text{Hv}}^* \gg m_{\text{Lt}}^*$ hypothesis was found).

T (K)	model	m_{Lt}^* (m_e)	m_{Hv}^* (m_e)	$\tau_{0\text{Lt}}$ (fs)	$\tau_{0\text{Hv}}$ (fs)	a (10^{-20} cm^3/ps)	$b_{e,h}$ (10^3 m/s)	B (10^{-23} cm^3/ps)
10	$\mu_e = \mu_h$	10.8±0.1		690±20		6.1±0.3	0±0.01	6.1±0.4
10	$\mu_e \neq \mu_h$	7.5±0.5	12±1	280±20	≥ 10 ps	6.7±0.2	0±2	6.3±0.3
30	[118]	6		~ 600		0–2.3	$b_e = 4–8$	–
70	$\mu_e \neq \mu_h$	5.6±0.8	9.2±0.3	37±8	540±30	8.1±0.5	–	7.7±0.8

Table 8.2 Coefficients of carrier transport and decay in rutile ($E \perp c$) as obtained from THz photoconductivity. Indices Lt and Hv denote respectively the lighter and heavier of the electron and hole polarons. In [118] electrons were considered as the much more mobile carrier type. The error values are standard deviations provided by the fit.

The lighter polaron tends to have about one order of magnitude shorter scattering time than the heavier one. With comparable masses, this means that the DC conductivity ($e\tau/m^*$) is carried rather by the heavier polarons. This is evident also in the low-frequency contributions of the two polaron types to the real part of

the response in Fig. 8.8. (We have checked that the longer low-density scattering time cannot be attributed to the carrier type with lower effective mass in the model.) The low-density scattering times in Table 8.2 show an almost order of magnitude decrease from 10 to 70 K. The spectrum of the lighter polaron type indeed becomes flat at 70 K, due to high scattering frequency, and the heavier polaron governs the spectral shape of the total response. The slight increase of the electron–hole scattering and recombination coefficients and the decrease of polaron masses from 10 to 70 K is near the indicated fitting uncertainty of our model (Table 8.2). We provide an inspection of the dependences of some of the transport parameters in a wider temperature range in the following two sections.

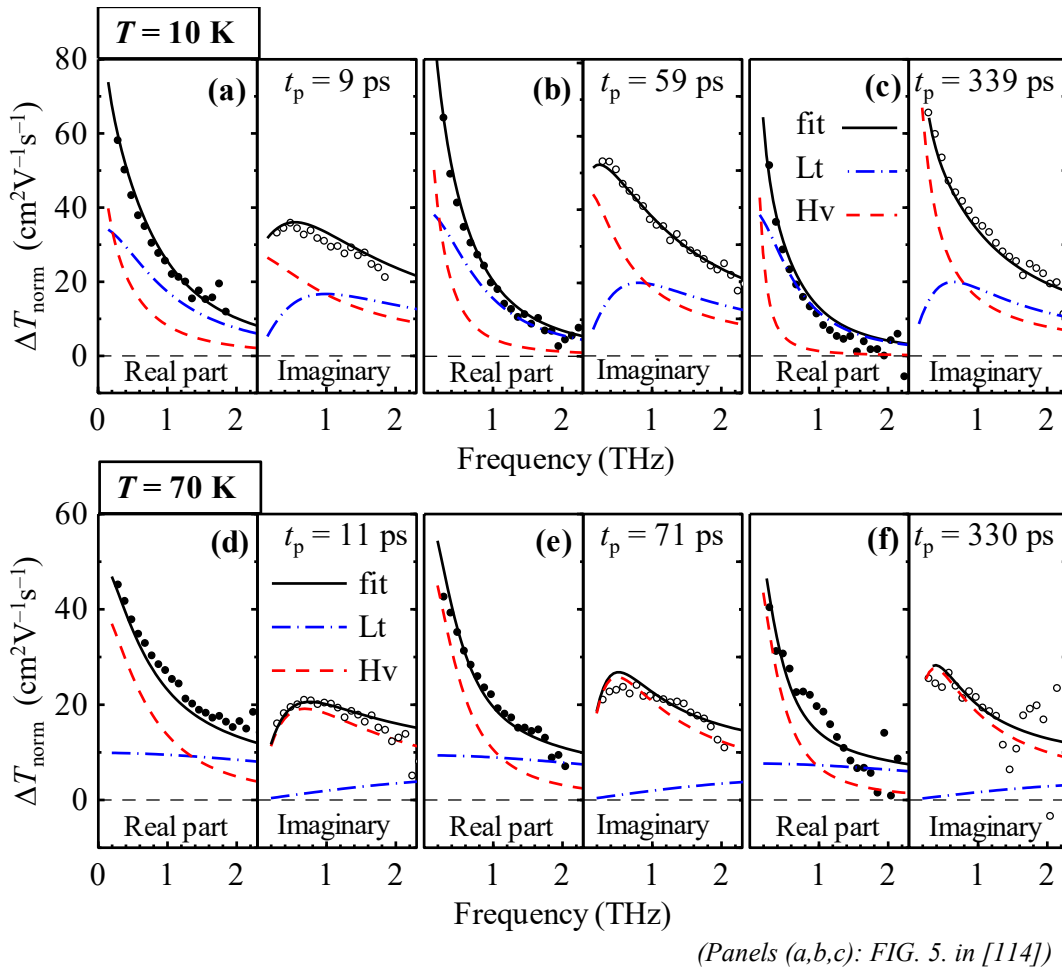


Fig. 8.8 THz photoconductivity spectra of rutile ($E \perp c$) at 10 and 70 K at selected pump–probe delays (indicated) at the highest fluence $\phi = 1.6 \times 10^{14}$ photons/cm². *Symbols*: experimental data. *Full black lines*: global fit with the general “ $\mu_e \neq \mu_h$ ” plasma diffusion model at each temperature. Contributions of electron and hole polarons are shown: *blue dash-and-dot lines* — lighter polaron type; *red dashed lines* — heavier polaron type.

The low-density mobility of the lighter polaron at 10 K is estimated to be 60–120 $\text{cm}^2\text{V}^{-1}\text{s}^{-1}$ and $\sim 10 \text{ cm}^2\text{V}^{-1}\text{s}^{-1}$ at 70 K. However, this last conclusion must be taken with caution as the fit probably underestimates the low-density scattering rate of the heavier polaron (the fit is insensitive to the value of $\tau_{0\text{HV}}$ when it rises above several picoseconds). A comparison of rows 1 and 2 in Table 8.2 shows that the values of carrier mass and low-density scattering time in the undifferentiated “ $\mu_e = \mu_h$ ” model lies between the respective values of the general model. Further, they show a good correspondence to the results of Hendry et al. [118], regarding the single-component low-density scattering time and effective mass (let us remind that Hendry et al. attributed the whole response to a single carrier type with effective mass $6 m_e$; our $\mu_e = \mu_h$ model described the same response by *two* carrier types with approximately twofold mass, accordingly).

As for the density-dependent scattering of carriers, Hendry et al. have found that the carrier–phonon scattering $b \cdot N^{1/3}$ term is rather more important than the electron–hole scattering $a \cdot N$ term (cf. Table 8.2) when fitting the $\tau^{\text{av}}(N^{\text{av}})$ dependence (8.2) at 30 K. [118] Our analysis shows that the linear electron–hole scattering mechanism sufficiently describes the measured dependences at 10 and 70 K when it is taken into account explicitly by integration (8.11) over the inhomogeneously excited region without averaging the carrier response. The scattering of carriers on acoustic phonons due to their increased Fermi velocity in filled bands is then found less likely in undoped rutile at examined carrier densities at low temperatures.

Fig. 8.9 further shows two spectra measured at the same intensity at 11 and 400 ps at 180 K. We do not have enough data at this temperature to perform a fit with the plasma diffusion model. However, single-component Drude fits (lines in Fig. 8.9) show that the (average) carrier scattering time again increases with the pump–probe delay, indicating that e–h scattering or another density-dependent scattering process is still in play at these higher temperatures.

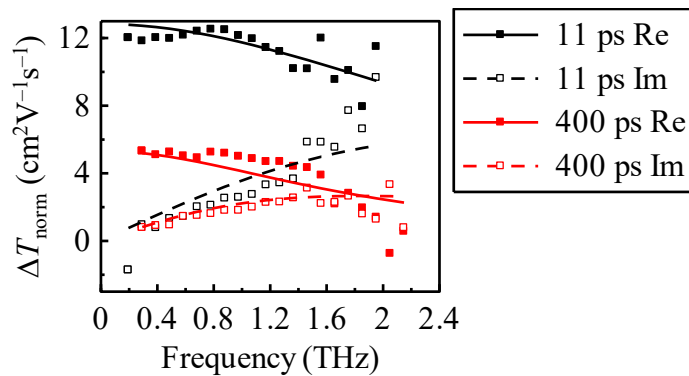
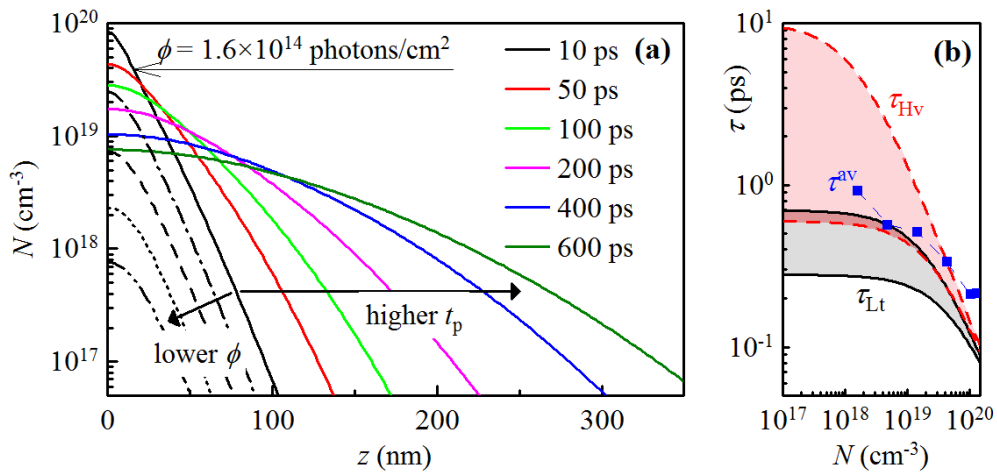


Fig. 8.9 THz photoconductivity spectra of rutile ($E \perp c$) excited with $\phi = 1.2 \times 10^{14}$ photons/cm² at 266 nm at two pump–probe delays at 180 K. *Boxes*: experimental data, *lines*: Fit with the single-component Drude model (8.1) with $\tau^{\text{av}} = 49 \pm 4$ fs at 11 ps and 86 ± 9 fs at 400 ps.

Fig. 8.10(a) shows the calculated density profiles corresponding to the delays and fluences of our experimental spectra at 10 K. An order of magnitude decrease of the carrier density during the first 500 ps is clearly seen, as well as the broadening of the carrier plasma depth profile. Panel (b) shows the calculated scattering times of the two polaron types, including the fitting uncertainty. When the carrier density drops below $\sim 10^{19} \text{ cm}^{-3}$, the scattering time of the lighter polaron ceases to depend strongly on the carrier density. The scattering time of the heavier polaron either does the same (the lower red borderline), or it rises so high that the corresponding Drude mobility peak at zero frequency is very narrow and cannot be observed in our experimental frequency range (cf. contributions of individual polaron types in Fig. 8.8(c)). Panel (a) of Fig. 8.10 shows that this regime is reached about 200 ps after photoexcitation (carrier density drops below $1.8 \times 10^{19} \text{ cm}^{-3}$ then).



(FIG. 6. in [114], panel (b) is supplemented with τ^{av})

Fig. 8.10 (a) Calculated carrier density profiles inside the rutile sample for selected pump–probe delays and fluences at 10 K; *colored lines*: excitation fluence of $1.6 \times 10^{14} \text{ photons/cm}^2$, the pump–probe delay is increased along the arrow (values are provided in the legend); *black lines*: pump–probe delay 10 ps, the excitation fluence is decreased along the arrow (values: 5.4×10^{13} , 1.8×10^{13} , 5.9×10^{12} , $2.0 \times 10^{12} \text{ photons/cm}^2$). (b) $\tau_{Hv,Lt}$: carrier density dependence of the momentum scattering time estimated from (8.9) by using values in the “ $\mu_e \neq \mu_h$, 10 K” row in Table 8.2; τ^{av} : scattering time obtained by single-component Drude fits of measured spectra.

Note also the blue data line in Fig. 8.10(b) which shows the scattering time values obtained by single-component Drude fits (8.1) of the spectra measured at 10 ps as presented by the cyan data line in Fig. 8.3. The characteristic time of the single-component fit τ^{av} is in general nearer to the longer of scattering times of the two polaron types and at high carrier densities, it follows a less steep dependence than $\tau_{Hv,Lt}$ (like $\sim N^{-1/3}$ as found by Hendry et al. [118]). This is clearly because of the averaging character of τ^{av} — the sum spectrum characterized by τ^{av} of the ensemble

of photoexcited carriers always contains a substantial contribution from the high-mobility carriers in the low-density region, which have long scattering times.

8.2. Temperature dependence of average mobility

We have also measured THz photoconductivity spectra of the sample at various temperatures with a constant pump–probe delay of 10 ps. Fig. 8.11 shows in symbols the spectra measured 10 ps after excitation with an intermediate photon fluence $\phi \approx 6.4 \times 10^{13}$ ph/cm². The data are fitted with the single-component Drude model of conductivity (8.1). The normalized transient transmittance (i.e. averaged mobility (8.11)) shows two orders of magnitude decrease from 10 to 300 K.

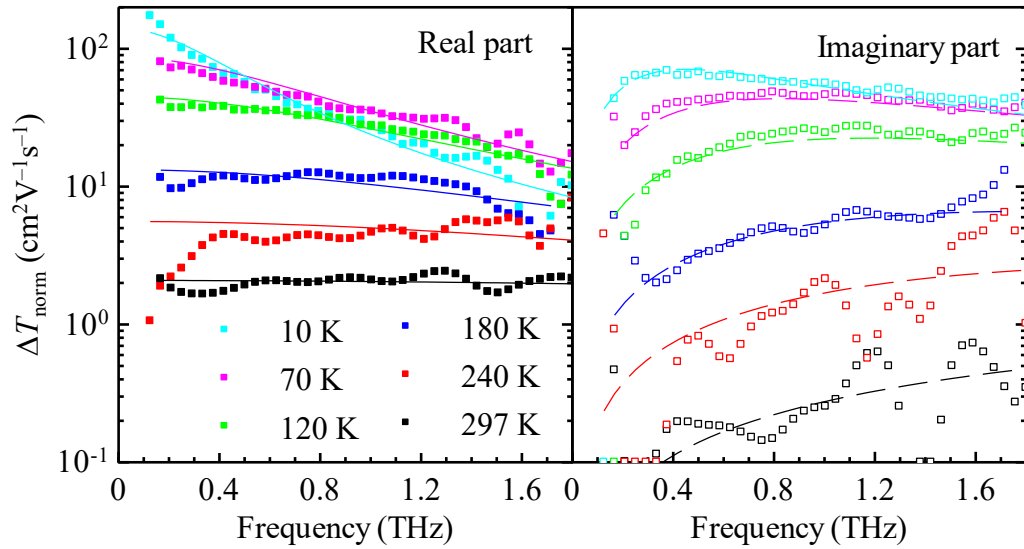


Fig. 8.11 THz photoconductivity spectra of a bulk rutile ($E \perp c$), measured $t_p = 10$ ps after excitation with $\phi \approx 6.4 \times 10^{13}$ ph/cm² at 266 nm at various temperatures. *Boxes*: experimental data, *lines*: single-component Drude (8.1) fits of individual complex spectra.

A 30-fold decrease of the single-component-fit scattering time with increasing temperature is clearly seen in Fig. 8.11 and plotted for three excitation fluences in Fig. 8.12. The latter Figure shows a qualitative agreement with data obtained in a previous work of Hendry et al. [128] with more homogeneous excitation (photons at 400 nm excite rutile at the very edge of the band gap with $\alpha = 900$ cm⁻¹, $1/\alpha = 11$ μ m [129]; intense pulses at 800 nm provide a very weak and homogeneous excitation by two-photon absorption throughout the thickness of the sample). Our low-density (magenta) data in Fig. 8.12 precisely copy the low-density data of Hendry (black and red), except for room temperature.

The single-component scattering time shows less than a 2-fold decrease from 10 to 70 K at individual excitation densities. This is much less than the 10-fold decrease of low-density scattering times of individual polaron types between these two temperatures as inferred from the general plasma diffusion model (cf. Table 8.2). This again documents the averaging character of τ^{av} . For this reason, it is not possible

to determine reliably any other quantity describing the transport, such as the carrier effective mass, from these data.

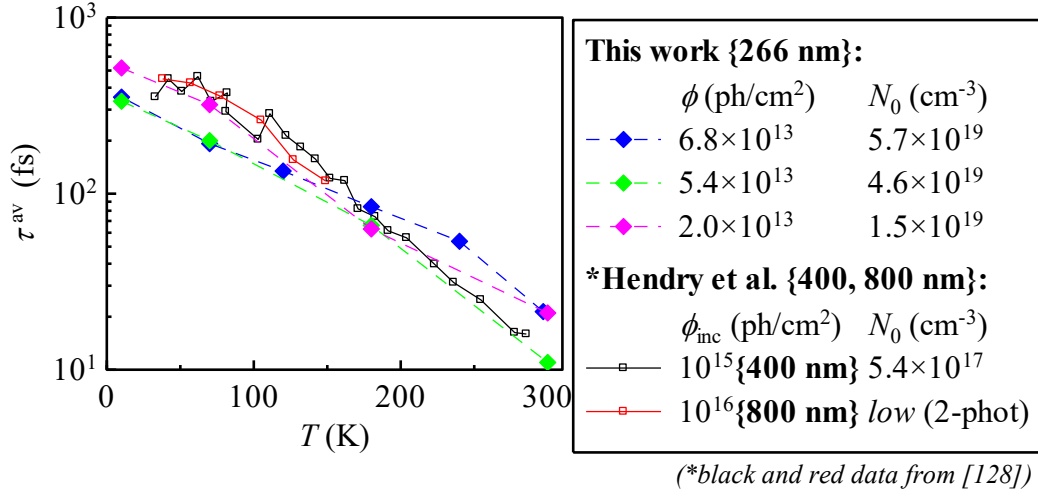


Fig. 8.12 Temperature dependence of the scattering time obtained by single-component Drude fits of THz photoconductivity spectra of rutile ($E \perp c$) at various excitation wavelengths (in curly brackets) and fluences, N_0 denotes initial surface carrier densities. ϕ_{inc} denotes incident photon fluence (not corrected by reflection).

8.3. Temperature dependent electron–hole recombination

The transient THz kinetics were measured (without spectral resolution) at temperatures between 10 and 300 K. We first derive a theory which allows us to quantify the electron–hole recombination from the measurable transient kinetics and then we present and discuss the obtained data.

8.3.1. Theory

The above discussed time evolution of the spectra of depth-integrated photoconductive response in our sample is very complex (cf. Section 8.1, namely Eqs. (8.11) and previous). A transient THz kinetics scan which reflects the overall, spectrally averaged, photoconductivity of the sample then presents rather a qualitative picture of the underlying processes. However, after a certain time after photoexcitation the carrier density decreases (due to the diffusion and recombination) to such an extent that the mobility of individual carriers is mostly density and time independent. Let us formally introduce the time t_d after which the carrier response spectrum does not change its shape. In this regime, the expression (8.11) for the normalized transient transmittance expression can be factorized in terms of the frequency-dependent mobility and the time-dependent carrier:

$$\Delta T_{\text{norm}}(\omega, t_p > t_d) \approx \frac{1}{\alpha \phi} \sum_{i=e,h} \mu_i(\omega) \int_0^L N(z, t_p) dz. \quad (8.14)$$

The THz kinetics (i.e. the maximum $\Delta E_t^{\max}(t_p)$ of the transmitted transient THz waveform) then evolves in time only due to the change of the total number of mobile carriers. The integral in (8.14) defines the sheet density of carriers $N_s(t_p)$. The kinetics of this quantity is determined by the diffusion equation (8.5). After integration of (8.5) over the thickness of the sample, we obtain

$$\int_0^L \frac{\partial N(t_p, z)}{\partial t_p} dz = -B \cdot \int_0^L N^2(t_p, z) dz; \quad (8.15)$$

where the diffusion term rigorously cancelled out after integration per partes because it affects only the depth-profile of the carrier density and not the integrated sheet density. Let us make the following approximation at the right-hand side of (8.14):

$$\int_0^L N^2(t_p, z) dz \approx \frac{1}{d} \left[\int_0^L N(t_p, z) dz \right]^2, \quad (8.16)$$

where d is the characteristic thickness of the carrier plasma cloud. This approximation is justified for a flat depth-profile of density. We check the validity of the approximation in our case later. We then find a simple differential equation for the sheet density:

$$\frac{\partial N_s(t_p)}{\partial t_p} \approx -\frac{B}{d} \cdot [N_s(t_p)]^2 \quad (8.17)$$

which leads to a hyperbolic decay of N_s with a characteristic recombination half-life t_B during which the sheet density decreases by a factor of two:

$$N_s(t_p) = \frac{N_s(0)}{1 + t_p/t_B}; \quad t_B = \frac{d}{BN_s(0)}. \quad (8.18)$$

If the regime of time-independent carrier mobility is reached before other processes (such as carrier trapping) occur, one may observe the process of bimolecular recombination in transient kinetics separately.

8.3.2. Discussion

Fig. 8.13 shows transient THz kinetics in rutile at the highest available excitation densities at various temperatures. The data are cut from the left to the point where the signal reaches $\sim 1/2$ of the maximum after photoexcitation and individual data lines are slightly shifted horizontally not to overlap. On the vertical axis, the plot shows the actual transient kinetics amplitudes without scaling (except 300 K that is 10 times up scaled): the decrease of the kinetics amplitude with increasing temperature corresponds to the decrease of the response (average mobility) of individual carriers (Fig. 8.11). The oscillations occurring between 2 and 6 ps were explained in the footnote on p. 98.

The measured kinetics were fitted with a sum of two exponential increases and a hyperbolic decay:

$$-\frac{\Delta E_{\max}(t_p)}{E_{\max}} = -A_1 \exp\left(-\frac{t_p}{t_1}\right) - A_2 \exp\left(-\frac{t_p}{t_2}\right) + \frac{A_B}{1+t_p/t_B}, \quad (8.19)$$

where the two exponential functions were chosen for purely practical reasons and we do not discuss them quantitatively — we are aware that the evolution of the spectrally averaged kinetics due to the carrier plasma diffusion is very complex and probably cannot be parametrized with a simple analytical formula.

The first exponential term in (8.19) fits the instrumental function of the signal rise and the fastest phase of the diffusion. The second term is qualitatively ascribed to a slower (tens of ps, cf. Fig. 8.14(a)) increase of the transient conductivity due to diffusion of carriers in the lower-density region deeper in the sample at low temperatures.

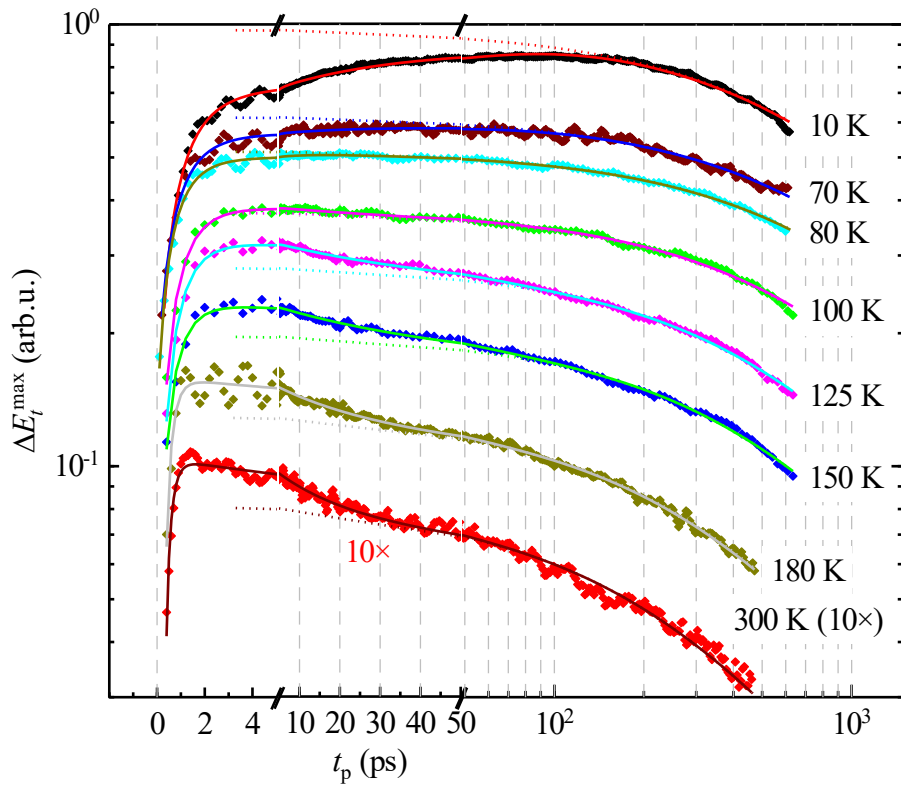


Fig. 8.13 *Points*: Transient THz kinetics of rutile ($E \perp c$) excited with $\sim 1.6 \times 10^{14}$ photons/cm² at 266 nm at various temperatures; *full lines*: fit with (8.19), *dotted lines*: hyperbolic part of the fit. (The kinetics at 300 was measured with 2.6×10^{14} photons/cm² and is scaled up 10 times in the plot.)

Above 100 K, a new competing process occurs at the early stages of the kinetics: an exponential *decrease* of transient kinetics. The process is clearly observable in Fig. 8.13 and it was captured by the parameters of the second exponential term of the fit with a negative sign of A_2 in Fig. 8.14(b). We attribute this decrease to the trapping of carriers in surface states or to the carrier recombination

through the surface states. Such effects are indeed expected to manifest themselves at elevated temperatures: due to increased thermal velocity, carriers from a larger distance from the sample front face interact with the surface states than at low temperatures.

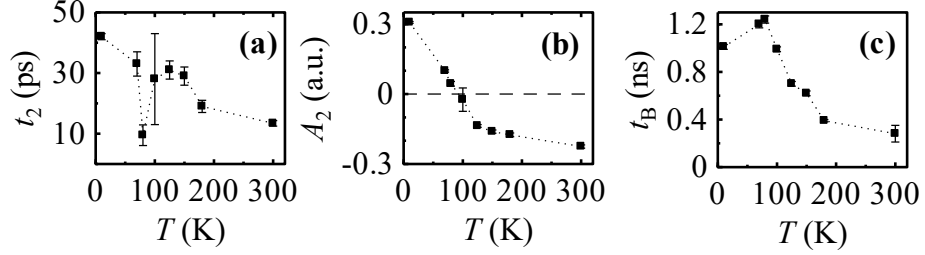


Fig. 8.14 Temperature dependences of the fitting parameters of the fitting function (8.19) of the transient kinetics in rutile ($E \perp c$).

Dotted lines in Fig. 8.13 show the contributions of the hyperbolic term to the fits at individual temperatures. Note that after about 100 ps, this contribution is dominant in all kinetics (full lines coincide with the dotted ones for $t_p > 100$ ps). Fig. 8.14(c) shows the temperature dependence of the recombination half-life t_B – it is clear here as well as in the kinetics (Fig. 8.13) that the recombination runs faster with increasing temperature. To obtain the recombination coefficient B from t_B (8.18), one needs to know the characteristic thickness of the carrier plasma sheet d . We assume that this quantity is proportional to the diffusion length of carriers during the recombination half-life $d \approx l_{\text{diff}}$. Lacking specific values of l_{diff} for electron and hole polarons, we make use of the temperature dependence of the single-component scattering time presented in Section 8.2.

In Fig. 8.15(a) we plot the temperature dependence of the diffusion coefficient calculated from the scattering times shown in Fig. 8.12 using the Einstein relation (8.7) and the Drude mobility amplitude (3.1):

$$D^{\text{av}} = \frac{k_B T}{e} \frac{e\tau^{\text{av}}}{m^*} \quad (8.20)$$

for an approximate, temperature-independent, average polaron mass $m^* \approx 10 m_e$ (cf. Table 8.2). This plot is nearest to reality in the red and black data lines from Hendry et al. [128], which were measured at the most homogeneous and low-density excitation — we observe a maximum of carrier diffusivity around 100 K and a decrease back to the 10-K value at room temperature. The carrier diffusion length related to the half-life of recombination is then $l_{\text{diff}}(t_B) = \sqrt{D^{\text{av}} \cdot t_B}$. Fig. 8.15(b) shows the temperature dependence of the bimolecular recombination constant (8.18) calculated from D^{av} (Fig. 8.15(a)) and t_B (Fig. 8.14(c)) as follows:

$$B = \sqrt{\frac{D^{\text{av}}}{t_B}} \frac{1}{N_S(0)}, \quad (8.21)$$

where the initial carrier sheet density is given by the excitation fluence $N_s(0) = \phi = 1.6 \times 10^{14} \text{ cm}^{-2}$. The values of $t_B(T)$ are linearly interpolated where missing. The calculated $B(T)$ dependence yields values of B from 4 to $12 \times 10^{-23} \text{ cm}^3/\text{ps}$ between 10 and 70 K which is consistent with the values yielded by the general plasma diffusion model (cf. Table 8.2). A several-fold increase of B towards room temperature is indicated.

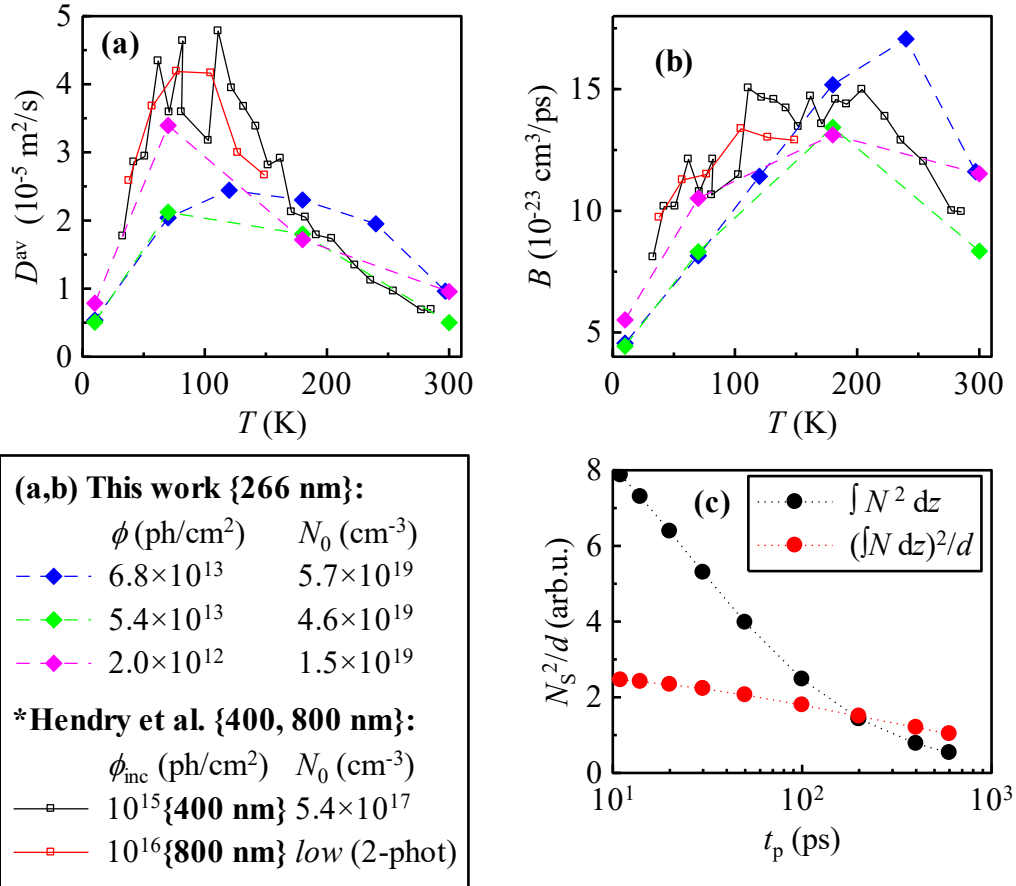


Fig. 8.15 Temperature dependences, in rutile ($E \perp c$), of: (a) “average” diffusion coefficient calculated from Fig. 8.12 using (8.20); (b) bimolecular recombination coefficient calculated from (a) and Fig. 8.14(c) using (8.21). *Data from [128]. (c) Time dependence of integrated quadratic carrier density calculated from Fig. 8.10(a) and its sheet density approximation (8.16) for $d = 90 \text{ nm}$ at 10 K.

The analysis above stemmed from the quadratic approximation (8.16). Fig. 8.15(c) shows that $(\int N dz)^2/d$ makes a reasonable order-of-magnitude estimate of $\int N^2 dz$ for 90 nm (Eq. (8.21) yields $l_{\text{diff}} \approx 90 \text{ nm}$ at 10 K) in the time interval $100 \text{ ps} < t_p < 600 \text{ ps}$.

8.4. Transient permittivity contribution at room temperature

At room temperature the normalized transient transmittance drops to $2 \text{ cm}^2\text{V}^{-1}\text{s}^{-1}$ as can be seen in Fig. 8.16. Such a weak response made it impossible to decrease the excitation fluence as low as in measurements at cryogenic temperatures (accumulation of spectrum (a) in Fig. 8.16 took about 15 hours). On the other hand, the absence of the cryostat enabled to reach slightly higher excitation fluences.

We observe that upon increasing the excitation density (Fig. 8.16(a,b,c)), the real part of ΔT_{norm} exhibits a small decrease. This can be again explained by density dependent electron–hole scattering. However, the slope of the imaginary part of $\Delta T_{\text{norm}}(\omega)$ flips gradually from positive to negative values. The increased scattering rate of free carriers by itself (8.9) may only lead to a decrease of the imaginary part of the normalized transmittance (8.11) to lower positive values. This indicates that on top of the carrier conductivity, an additional response emerges due to some other kind of bound polar excitations, which are sensitive to the pump fluence.

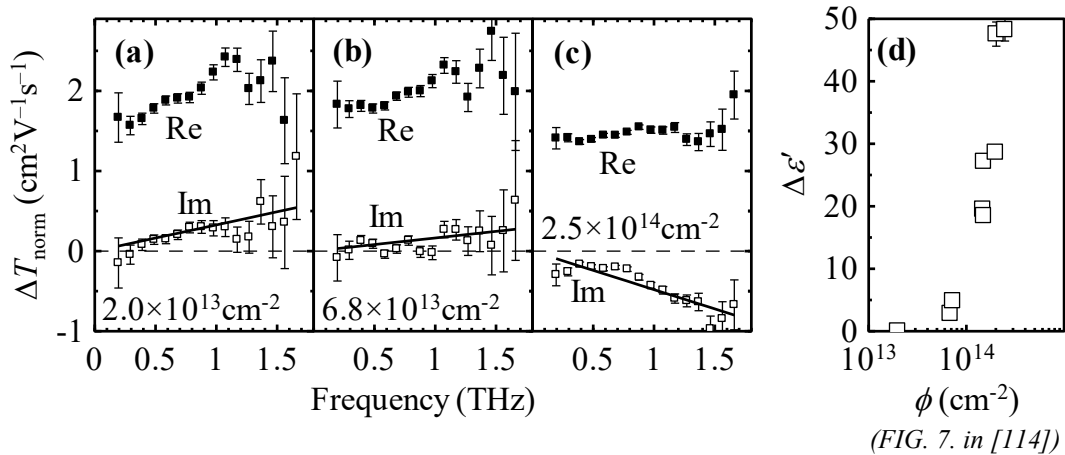


Fig. 8.16 Spectra of THz photoconductivity in rutile ($E \perp c$) at (a) low, (b) medium and (c) maximum excitation fluences (indicated in the plots) at 266 nm, measured 10 ps after photoexcitation. *Symbols*: data, *solid lines*: linear fit of the imaginary part with (8.22). (d) Positive transient contribution to the real permittivity related to the change of slope of the imaginary mobility versus excitation fluence.

The observed approximately linear slope of the imaginary part of $\Delta T_{\text{norm}}(\omega)$ corresponds to a constant contribution to the transient *real* permittivity $\Delta \epsilon'$ that was determined by a linear fit (solid lines in Fig. 8.16(a,b,c))

$$\text{Im}[\Delta T_{\text{norm}}(\omega)] = -\epsilon_0 (\Delta \epsilon'_{\text{Drude}} + \Delta \epsilon') \frac{\omega}{e \alpha \phi} \quad (8.22)$$

of spectra measured at 9 excitation fluences. We assume that at the lowest available charge carrier density, any additional localized response can be neglected ($\Delta\varepsilon' = 0$) and the initial positive slope of $\sim 0.3 \text{ cm}^2\text{V}^{-1}\text{s}^{-1}$ per 1 THz (Fig. 8.16(a)) corresponds solely to the Drude response of mobile polarons with a scattering time of about 20–30 fs ($\Delta\varepsilon'_{\text{Drude}} \approx -1.6$). We observe in Fig. 8.16(d) that $\Delta\varepsilon'$ makes a substantial contribution of 50 to the equilibrium value of 90 (cf. Fig. 8.2) at high photocarrier densities. Note, however, that this strong dielectric contribution concerns only the very thin (12 nm) strongly photoexcited layer close to the surface of the sample. Below we propose several phenomena that we find relevant to the observed dependence.

Non-equilibrium phonon states

The pump photon energy of 4.7 eV exceeds the carrier band gap by 1.5 eV; this excess energy of photocarriers is rapidly transferred to the lattice, i.e., a non-equilibrium population of optical and acoustic phonons is generated in the excited layer of the sample. The equilibrium parameters (eigenfrequency ω_0 and oscillator strength) of certain phonon modes can be altered under these conditions due to their anharmonic character. Pashkin et al. [130] directly observed characteristic spectral signatures of hot polar phonon population induced by optical pumping of a high-temperature superconductor in the frequency range above 8 THz. Here we are probing at much lower frequencies, which means that we sense a transient change of the *static* permittivity of some high-frequency phonon modes. The related spectral changes in the THz permittivity (or imaginary conductivity) are predominantly due to the change of the phonon eigenfrequency $\Delta\varepsilon \propto -\Delta\omega_0(\phi)$ while changes in the losses (real part of the conductivity) are expected to be much smaller. A quantitative interpretation is complicated by the fact that rutile exhibits incipient ferroelectric trends [131] accompanied by softening upon cooling of A_{2u} (172 cm^{-1} at room temperature) and E_u (189 cm^{-1} at room temperature) polar phonons [132] and such phenomena may bring strong anharmonic effects.

Density-dependent polaron ionization

The quantitative assessment of the observed transient permittivity contribution is also complicated by the polaronic character of charge carriers in rutile. The slow itinerant polaron motion is characterized by the Drude-like response at THz frequencies as observed in our experiments. Internal degrees of freedom of medium or large polarons, i.e., the hydrogen-like spectrum reflecting the quasi-particle excitation or ionization, appear in the mid- or near-infrared spectral range [133]. The tails of the latter characteristic signatures may extend down to the THz region and provide another correction to the spectrum.

Recently, an absorption peak in rutile has been observed at 115 meV and assigned to the intrinsic absorption in polaron trap states [134]. Using DFT calculations, these authors determined the ionization energy and the Bohr radius of the hydrogen-like potential in which the electron moves ($E_{\text{ion}} = 0.38 \text{ eV}$, $a_{\text{B}} \approx 4 -$

5 Å). For an order-of-magnitude estimation of the strength of the polaron ionization response at THz frequencies, we consider only the lowest ($1s \rightarrow 2p$) hydrogen-like transition which provides a dominant contribution to the permittivity. The corresponding polaronic dielectric strength is calculated using the Fermi's golden rule:

$$\varepsilon_{\text{pol}}(\omega) = \frac{1}{\varepsilon_0} \frac{4Ne^2}{E_{2p} - E_{1s} - \hbar\omega - i\gamma} \left| \langle 1s | z | 2p \rangle \right|^2 \approx \frac{\alpha\phi e^2}{\varepsilon_0 E_{\text{ion}}} 2.2a_{\text{B}}^2. \quad (8.23)$$

The order-of-magnitude estimate for the lowest excitation fluence (2×10^{17} photons/cm²) from this formula is $\varepsilon_{\text{pol}} \approx 0.4$; this contribution is added to the steady-state permittivity of the material ε formally defined as a low-frequency permittivity with the polaronic effect subtracted. Following (8.23), an increase of the photon excitation fluence ϕ leads to an increase of ε_{pol} . However, at high carrier densities, this increase of the material permittivity induces a polaron softening (decrease of the ionization energy and of the energy of polaronic transitions) and an increase of its transition dipole moment. Indeed, in the hydrogen-atom model, the energies of the intra-polaronic transitions are inversely proportional to the square of the surrounding permittivity: $E_{\text{ion}} \propto (\varepsilon + \varepsilon_{\text{pol}})^{-2}$, and the Bohr radius scales with this permittivity: $a_{\text{B}} \propto (\varepsilon + \varepsilon_{\text{pol}})$. In other words, polarons “feel” each other through their contribution to the permittivity of the lattice. Eq. (8.23) then represents a nonlinear equation for ε_{pol} due to the polaron–polaron interaction and the effect of the high carrier density can become very significant. For example, solution of this nonlinear equation yields $\varepsilon_{\text{pol}} \approx 20$ at the excitation fluence of 5×10^{18} photons/cm². This is, of course, a very crude reasoning; however, it shows that the sign and the order of magnitude of the expected effect is the one that we have experimentally observed.

Time evolution of the transient permittivity component

We measured also transient transmittance spectra at various delays up to 430 ps at the highest excitation density, see Fig. 8.17(a) (we plot the raw data ΔT , not ΔT_{norm} , because the excitation fluence and refractive index do not play any role in the discussed time evolution). We have found that the shape of the spectrum does not change: The ratio between the slopes of the real and imaginary part of transient transmittance is constant as seen in Fig. 8.17(b). This indicates that the transient permittivity contribution decays hand in hand with the decay of the carrier number. The observation of Fig. 8.17 speaks strongly to any phenomenon that is linked to the carrier concentration such as the density-dependent screening of polaron ionization.

Based on the current experimental results we are unable to draw more quantitative conclusions. It would be extremely useful to perform a similar pump–probe study using a probing pulse in the multi-THz frequency range, where the transient contributions of the phonon modes can be directly spectrally resolved and the origin of the transient permittivity could be assigned.

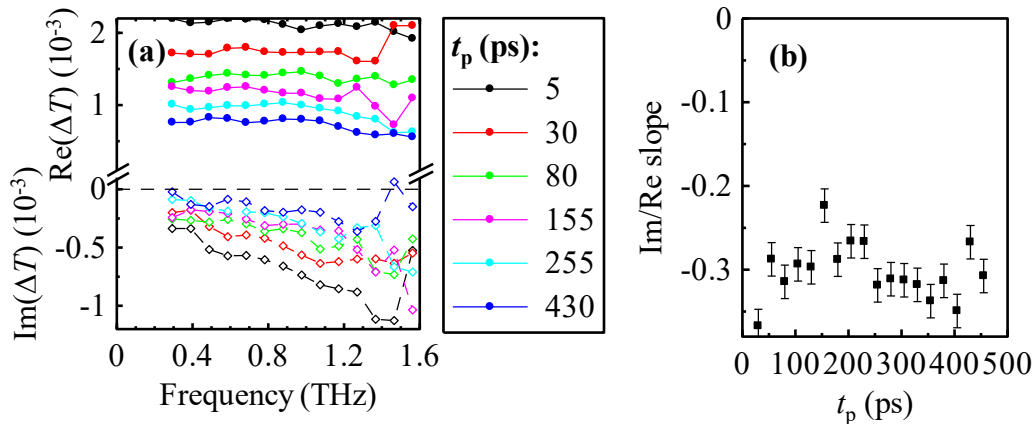


Fig. 8.17 (a) Evolution of transient THz transmittance ΔT of rutile ($E \perp c$) at 300 K, (b) the ratio of linear slopes of real and imaginary part of ΔT .

8.5. Conclusion

We investigated charge carrier transport in (001)-oriented rutile using time-resolved THz spectroscopy at temperatures between 10 and 300 K in detail. Photoexcitation by femtosecond pulses at 266 nm leads to a highly inhomogeneous photocarrier density distribution in the depth of the sample. Drude like conductivity response is observed at low excitation fluences (both at low and at high temperatures). However, experiments at higher fluences reveal very complex underlying phenomena.

Namely, electron–hole scattering decreases the carrier mobility by an order of magnitude at the strongly photoexcited surface as compared to the weakly excited bulk of the crystal. Moreover, the carrier concentration close to the surface decreases on a tens of picoseconds time scale due to ambipolar diffusion of carriers towards the bulk and, in turn, the mobility averaged over the carrier population increases on the 100 ps time scale at 10 K.

We developed a general plasma diffusion model that relates all these phenomena to the evolution of measured THz photoconductivity spectra during the first nanosecond. This allowed us to quantify the scattering, recombination, and ambipolar diffusion of carriers at low temperatures, to assess the role of the electron–hole scattering and to deduce that the mobility of both electrons *and holes* is substantial in the THz charge transport in rutile at low temperatures. The DC mobilities of the two carrier types differ significantly due to notably different scattering times; rather than owing to polaron masses which differ by a factor of less than 2.

Finally, at room temperature we observed a competition between the Drude-like contribution of the itinerant motion of polarons and a positive transient contribution to the real part of permittivity due to hot phonon states and/or polaron internal degrees of freedom. Indeed, a tail of the mid-infrared polaron excitations should appear in the THz photoconductivity spectra. We report the sum mobility of electron and hole polarons of $2 \text{ cm}^2\text{V}^{-1}\text{s}^{-1}$ in our crystal at room temperature. The

measured transient modulation of the permittivity due to the non-equilibrium phonon and polaron population is very strong (up to $\Delta\varepsilon = 50$). Time resolved measurements of the THz photoconductivity indicate that the modulation has a lifetime comparable to that of mobile polarons. Experiments at multi-THz frequencies would be very useful to elucidate which of the proposed hypotheses is correct and to quantify its properties. The motivation is even stronger if we consider the incipient ferroelectric character of TiO_2 and that our results show the possibility to observe the tuning of the dielectric constant by means of optical excitation and carrier–phonon coupling.

9. Morphological interpretation of probabilistic parameters in Monte Carlo calculations of carrier mobility in nanomaterials

Section 3.5 introduced our Monte Carlo simulations that provide the mobility spectra of a band carrier moving in a nanoparticle system with explicitly given nanoscopic properties (particle size, bulk scattering time, system temperature etc.). In this Chapter we compare the carrier mobility spectra calculated in two different spatial regimes. The first — *probabilistic* — regime has been introduced in [70]; it determines the result of interaction of a charge carrier with nanoparticle boundary (tunneling, backward or forward scattering) based on a set of pre-defined probabilities regardless of the position of the point of interaction. The second — *morphological* — regime replaces the probabilistic parameters of the first regime by geometrical properties of the nanosystem and it was newly developed within this thesis.

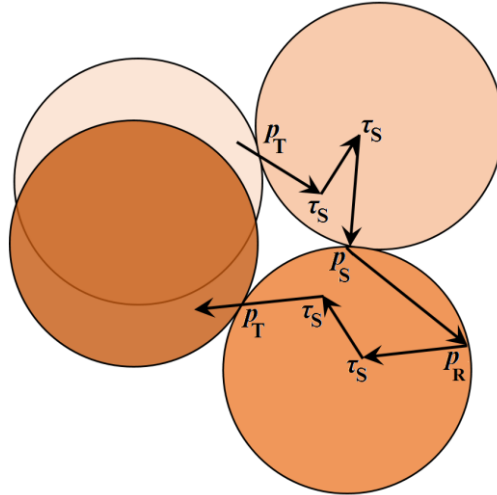


Fig. 9.1 Schematics of the trajectory of a carrier in spherical nanoparticles in our Monte Carlo simulations. Note that the 4th and the 1st sphere overlap. Labeled events: τ_S = bulk (isotropic) scattering; p_T = tunneling (transmission) through the boundary without scattering; p_S = isotropic scattering on a boundary; p_R = backscattering on a nanoparticle boundary.

In the *probabilistic* regime, the carrier moves thermally in a single perfectly spherical particle. When the carrier meets the wall of the sphere, it is allowed to pass through the nanoparticle boundary into a neighboring nanoparticle with a certain probability. The position of the target sphere is defined *ad hoc*, touching with the current sphere at the point where the carrier passed through the wall and the position of the previous sphere is not stored. During the next boundary scattering event, the third sphere can happen to be placed over the first one (Fig. 9.1). This procedure mimics in a certain way a random arrangement of touching particles in disordered

nanosystems. The problem of superposed nanoparticles in the probabilistic regime is avoided only when tightly-spaced nanocubes are used instead of spheres or ellipsoids.

In the *morphological* regime, the carrier moves thermally in a system of nanospheres with diameter D whose position in the space is *a priori* fixed e.g. in a cubic arrangement with a lattice constant a (Fig. 9.2 shows four qualitatively different structures resulting from different ratios between a and D).

We have developed the latter model in order to investigate whether the perfect spatial arrangement of the nanospheres cannot bring new spectral features to the calculated mobility spectra, compared to the “disordered” probabilistic regime. Below, we provide the description of the simulations in the two regimes, we discuss in detail the data obtained in the morphological regime and finally we compare the mobility spectra calculated in both regimes.

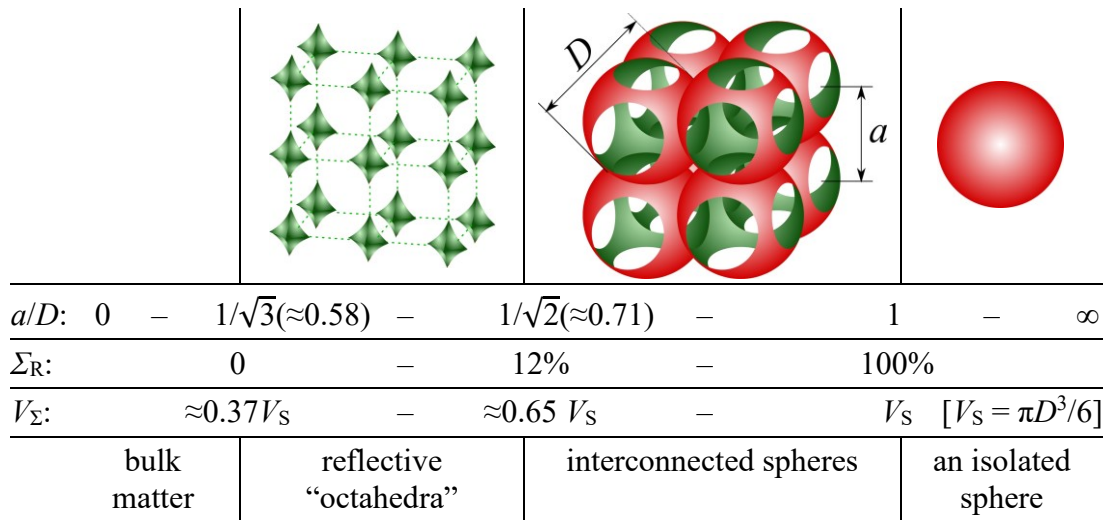


Fig. 9.2 Structures defined by cubic arrangement of spherical particles with different ratios of diameter D and lattice constant a . Dotted lines between spherical “octahedra” in the second column are plotted as guides to the eye in the planar 3D projection. Σ_R : reflective portion of the surface of the unit cell, V_Σ : volume of the unit cell in ratio to the volume V_S of a sphere with the same diameter.

We simulate the thermal motion of the charge carrier in the volume of a nanoparticle identically in both regimes. The charge carrier starts with a random velocity (within a suitable statistical distribution as described below) at a random point inside the nanoparticle; after a certain time, it chooses a new random velocity to simulate scattering at a point defect. The new velocity has a random direction and a magnitude chosen randomly from the Fermi–Dirac or Boltzmann (as pre-selected) distribution at a given temperature. The interval between these “bulk” scattering events is chosen randomly within an exponential distribution with a fixed average time τ_s and does not depend on the carrier position. The discussed simulation

regimes differ by the behavior of the charge carriers when they hit the nanoparticle boundary.

In the probabilistic regime, three factors p_T , p_S and p_R determine the subsequent motion of the charge carrier (see Fig. 9.1).

- p_T — carrier passes the boundary without changing its velocity magnitude or direction — emulating either an ideal (crystalline) conductive path to the neighboring particle or *tunneling* through possible potential barriers at the boundary between the two particles;
- p_S — carrier scatters at the boundary with a random change of speed and direction as in the case of the bulk scattering. This case simulates that the carrier is *scattered* at a surface state at the boundary.
- p_R — carrier is randomly *reflected off* the boundary and remains in the original nanoparticle with the ongoing direction randomly chosen from the half-space belonging to the original nanoparticle.
- The three probabilities are naturally normalized: $p_T + p_S + p_R = 1$.
- In many cases, it is useful to evaluate the results of the probabilistic simulations in terms of the total probability of backward scattering $p_B = p_R + p_S/2$ and forward scattering $p_F = p_T + p_S/2$.

In the morphological regime, the carrier behavior at the nanoparticle boundary is determined by its position, instead of the probabilistic quantities. In our model the nanoparticle is represented by an intersection of a sphere with diameter D and a cube with edge a which have a common center. Two types of boundaries can be distinguished: the cube walls do not feature any additional interface scattering ($p_T = 1.0$, $p_S = 0$) and the two adjacent nanoparticles are considered as continuous bulk material at this place, while the remaining spherical surfaces (green areas in Fig. 9.2) are defined as completely reflective ($p_R = 1.0$). We characterize the unit cells with the ratio Σ_R of the reflective (green) area of the boundary of the unit cell versus the total surface of the unit cell.

Carrier mobility spectra in the morphological regime were calculated for different ratios of the carrier bulk mean free path l_{free} and the diameter D and for different degrees of the nanoparticle connectivity (different a/D ratios). These spectra were compared to the mobility spectra of carriers with the same l_{free} calculated in the probabilistic regime in spheres with the same D and with variable probabilities p_R of the reflection on the sphere boundary (the interface scattering was also neglected, $p_S = 0$, $p_T = 1 - p_R$). For each combination of a , D and l_{free} , the best fitting p_R was found by comparing the carrier spectra in the two regimes in the frequency interval 0.01–100 THz.

9.1. Carrier mobility in the morphological regime

We performed simulations of the motion of a charge carrier in a non-degenerate semiconductor (with Maxwell-Boltzmann velocity distribution) with

the conduction band effective mass equal to $1 m_e$, and with the bulk scattering time $\tau_s = 86$ fs at room temperature. The carrier mean free path in the bulk is thus $l_{\text{free}} = 5.8$ nm. The carrier motion was studied in nanoparticles with the diameters $D = k \cdot l_{\text{free}}$ (with $k = 0.81, 2.5, 8.1, 25$) and the lattice constants a ranging between D and $\sqrt{3}D$. The choice of carrier properties and nanoparticle sizes was motivated by a previous study by Mics et al. [47] of THz photoconductivity in CdS nanocrystals.

Fig. 9.3 shows the calculated mobility spectra in the morphological regime with several lattice constants for three nanoparticle diameters. For $a/D < 1/\sqrt{3}$ the structure represents the bulk matter (cf. Fig. 9.2) and the simulations provide the Drude mobility as expected (black lines in Fig. 9.3(a,b,c)). For nanoparticles with a diameter much *larger* than l_{free} (Fig. 9.3(a)), the impact on the THz part of the mobility spectrum (shaded regions in Fig. 9.3) is rather low. The reflective parts of their walls constitute long- or mid-range barriers, which slow down the carrier transport mostly at low frequencies. Even with isolated spheres (cyan curve in Fig. 9.3(a)) the mobility spectrum can be fitted relatively well with the Drude model in the THz region (Fig. 9.4(a)). This is because the carrier meets much more often a bulk scattering center than the nanosphere wall.

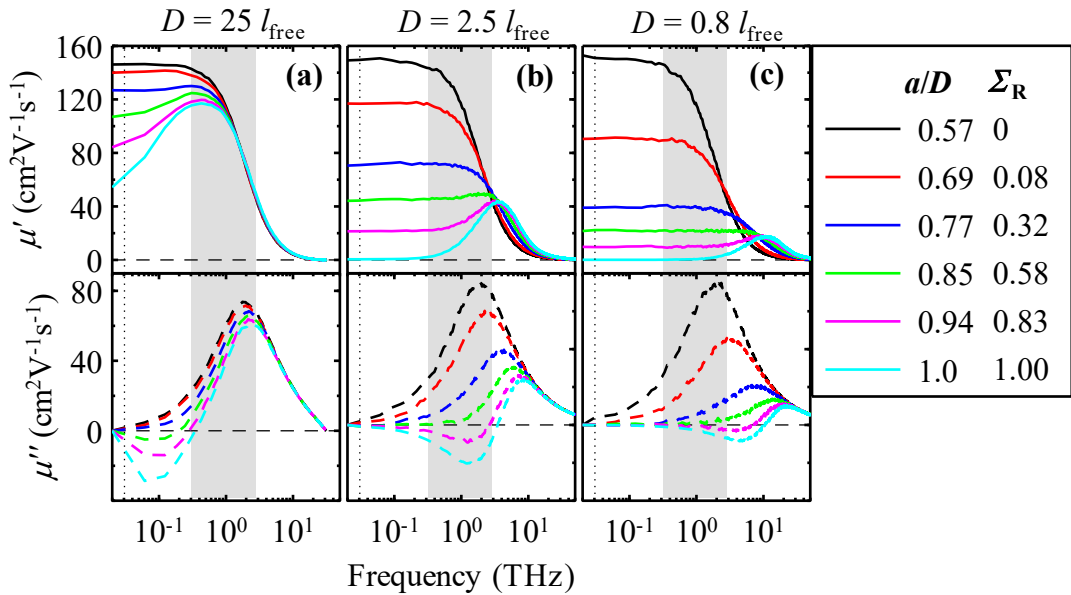


Fig. 9.3 Carrier mobility spectra calculated in the morphological regime of Monte Carlo simulations with $l_{\text{free}} = 5.8$ nm, D : (a) 142 nm, (b) 14.2 nm and (c) 4.7 nm at various a/D ratios. Shaded regions delimit the spectral region 0.3–3 THz which is typically accessible in OPTP experiments. The vertical dotted lines indicate 30 GHz; the mobility value for this frequency is plotted in Fig. 9.4(b).

On the other hand, nanoparticles with a diameter comparable to l_{free} (Fig. 9.3(b,c)) suppress both real and imaginary part of the carrier mobility in a wide

frequency range. Surprisingly, an enhancement of the real mobility occurs above the bulk scattering frequency, $1/(2\pi\tau_s) = 1.86$ THz. With more than $\sim 70\%$ of the nanoparticle surface being reflective (magenta and cyan curves in Fig. 9.3(b,c)), clear signs of the short-range carrier confinement in the THz frequency range are apparent (μ' is increasing with frequency and μ'' is negative). The resonance frequency (where μ' reaches its maximum and $\mu'' = 0$) is connected to the carrier round-trip time in the (almost) isolated nanoparticle. [70]

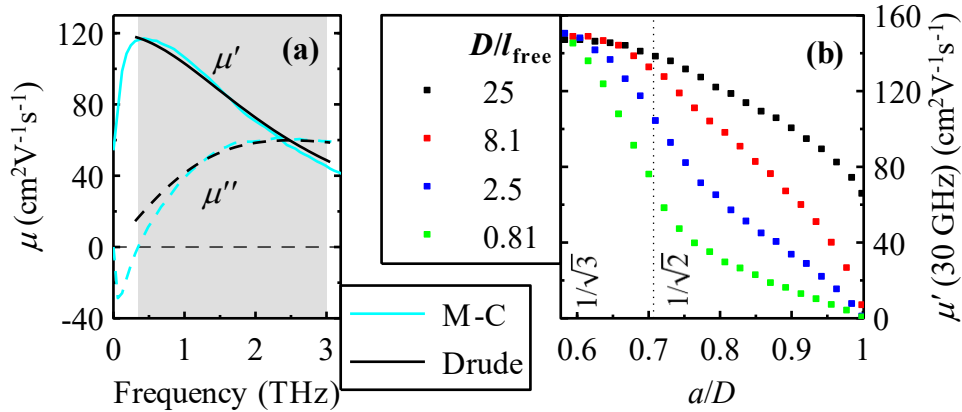


Fig. 9.4 (a) *cyan*: Carrier mobility spectrum calculated in the morphological regime of Monte Carlo simulations with $l_{\text{free}} = 5.8$ nm, $D = 142$ nm, $a = D$ (same as cyan curve in Fig. 9.3(a)); and *black*: its Drude fit between 0.3-3 THz. (b) Carrier mobility at 30 GHz for various D/l_{free} ratios versus a/D for $l_{\text{free}} = 5.8$ nm.

In Fig. 9.4(b), we plot the low frequency carrier mobility versus the a/D ratio. The carrier mobility decreases with the growing area of reflective parts of the nanoparticle boundary, as one would expect. In the largest particles (black symbols), the carrier mobility even does not drop to zero at $a/D = 1$. (Note that we cannot plot here the DC mobility as the Kubo formula (3.28) cannot provide the mobility at zero frequency from the velocity recorded over a finite time.) In systems with the particle diameter comparable to l_{free} (blue and green symbols in Fig. 9.4(b)), the carrier mobility decreases much faster with increasing lattice constant than in $D \gg l_{\text{free}}$ systems (black symbols).

In the limit $a/D \rightarrow 1/\sqrt{3}$, the green octahedra in Fig. 9.2 collapse into point defects with a volume density of a^3 . With increasing a/D ratio, the cross-section of these octahedra rapidly increases. The volume density of the defects in the “bulk” of nanoparticles is $\approx l_{\text{free}}^3$. In systems with $D \gg l_{\text{free}}$, the carrier encounters a bulk defect much more often than the particle boundary; its mobility spectrum remains almost Drude-like in a broad spectral range with the low-frequency value significantly decreased for high a/D only, i.e. when the carrier becomes effectively confined in a unit cell. In $D \approx l_{\text{free}}$ systems, the carrier scatters comparably often on bulk and boundary scatterers — when the cross-section of the boundary increases (a/D increases), the carrier mobility rapidly drops in the whole spectral range.

9.2. Comparison of morphological and probabilistic regime

For each spectrum calculated in the morphology regime, we found a single value of p_R that yielded a practically identical mobility spectrum in the probabilistic regime. Fig. 9.5(a) gives an example of a good coincidence of the spectra obtained in the two regimes. We see that the carrier mobility spectrum in a cubically cut sphere with $\Sigma_R = 70.4\%$ of reflective walls is mimicked by the carrier mobility in spheres of the same diameter with a boundary reflection probability $p_R = 0.761$. We discuss here the relation of the best fitting values of p_R in the probabilistic regime to the values of the reflective surface portion Σ_R in the morphological regime. Let us remind that the two simulation regimes were calculated for different volumes of the unit cell. The probabilistic regime uses a sphere of a given diameter D with independent p_R whereas in the morphological regime, the reflective surface portion Σ_R of the unit cell is connected to the ratio of the diameter D and the lattice constant a (cf. Fig. 9.2). The volume of the morphological unit cell with a given a/D ratio was calculated numerically.

Fig. 9.5(b) shows the ratio of: (i) the reflective surface portion Σ_R of the unit cell normalized to the unit cell volume V_Σ in the morphological regime and (ii) the best fitting reflection probability normalized to the sphere volume $V_S = \pi D^3/6$. (We do not plot error bars of p_R in Fig. 9.5(b) for clarity; they are comparable to the scatter of adjacent points of each data line. We cut the data where the relative uncertainty of p_R exceeds 100%.)

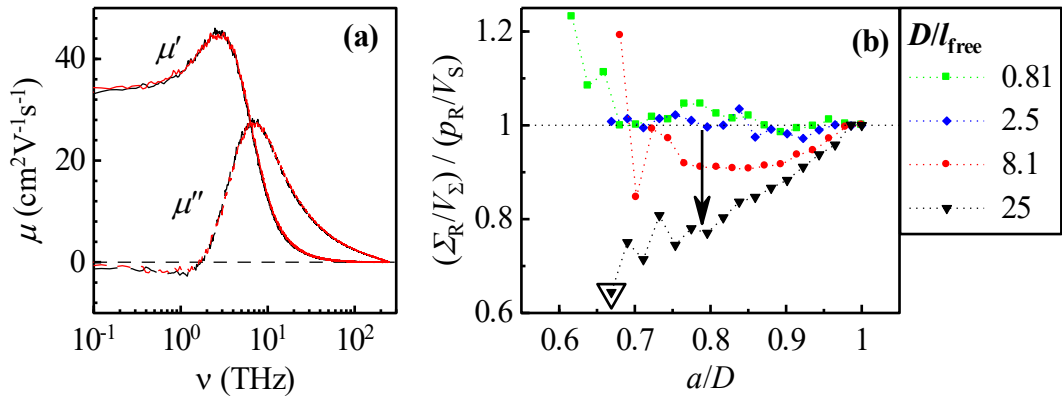


Fig. 9.5 (a) Carrier mobility spectra in spheres with $D = 14.2$ nm calculated in the morphological regime ($a = 12.8$ nm, $\Sigma_R = 0.704$, black line) and in the probabilistic regime ($p_R = 0.761$, red line). (b) Symbols: the ratio of reflective surface fraction of the unit cell per its volume to the boundary reflection probability of the sphere per its volume.

The ratio naturally tends to 1 at $a/D = 1$ for all D/l_{free} ratios because isolated spheres have the same properties and sizes in both regimes. In *small* nanoparticles ($D \approx l_{\text{free}}$, green and blue data), the ratio remains unitary within errors in the whole range. This means that the probability of reflection p_R in the probabilistic regime can

be interpreted as the ratio of the reflective and the total surface of nanoparticles for $D \approx l_{\text{free}}$. However, the plotted ratio decreases with increasing particle size (along the arrow). This means that *large* morphological unit cells with a certain reflective surface portion Σ_R produce the same mobility spectra as probabilistic spheres with a notably *larger* value of boundary reflection probability $p_R > \Sigma_R$. The difference between p_R and Σ_R is small for high a/D ratio (almost completely reflective nanoparticles) and increases with decreasing a/D . We illustrate this at the point in triangle in Fig. 9.5(b): The carrier mobility in a unit cell with a diameter of $25 l_{\text{free}}$ and 6.0 % of surface being reflective ($V_\Sigma = 0.56 V_S$) is reproduced with the mobility of a carrier in a sphere with $p_R = 16.5$ % ($[\Sigma_R/V_\Sigma]/[p_R/V_S] = 0.64$ in the graph).

The nanoparticle boundary in the probabilistic regime can be understood as a spherical wall consisting of infinitesimally small surface elements — a portion p_R of the surface elements is reflective and the other are permeable for the carrier, but the local distribution of the reflective and permeable surface elements on the wall is random. From the morphological point of view, the probabilistic boundary is equivalent to a more or less dense sieve — in contrast to solid reflective surfaces (green areas in Fig. 9.2) in the morphological unit cell. On the short range, the spatial non/arrangement of the reflective boundaries does not play a role for the resulting carrier mobility spectrum. On the *long* range ($D \gg l_{\text{free}}$), a carrier is more effectively localized with a compact piece of a reflective interface of a certain cross-section than with a semi-permeable boundary with a corresponding reflection probability. The smaller is cross-section of the reflector, the higher is its relative reflection effectivity.

Physically, the morphological approach can rather describe structures made of compact building blocks (nanocrystals, nanowires etc.) which are either in a good conductive contact or separated by well-insulating matrix or voids; the probabilistic approach can be more useful when describing nanoparticles separated by poorly conducting interfaces, e.g. amorphous matter between nanograins in a polycrystalline material.

9.3. Conclusion

We have found that the probabilistic regime of our Monte Carlo simulations provides mobility spectra that are essentially equivalent to the spectra in the morphological regime. The probabilistic regime thus remains a very useful and computationally more efficient tool for modelling of the carrier mobility in semiconductor nanosystems. We have found in Fig. 9.5(b) that for small nanoparticles (with size comparable to l_{free}), the boundary reflection probability can be interpreted as the morphological ratio of reflective and conductive boundaries between individual nanoparticles. For large nanoparticles, the equivalent boundary reflection probability is systematically higher than the reflective surface portion of a morphological unit cell and the difference increases with increasing connectivity between adjacent nanoparticles. In such cases, more attention must be paid to the morphological interpretation of the fitted value of boundary reflection probability.

10. Conclusion

The THz frequency range offers spectral features that are related to the transport of electric charge on a nanometer length scale. In the introductory chapters we have reviewed the current state of Optical pump–THz probe spectroscopy in the field of semiconducting nanomaterials from both the experimental and theoretical point of view. In the original part of the work we have answered two important questions, which significantly help the understanding of the THz photoconductivity of nanostructures on a microscopic level:

1. A deeper insight into the effective medium theory able to describe systematically the THz response of semiconductor nanostructures was missing. In our attempts we focused on nanomaterials containing a general combination of percolation pathways and isolated inclusions with the aim to develop a viable general description based on a minimum number of morphological parameters. The resulting VBD model is described and discussed in this thesis. We provide methodological instructions that profit from the understanding of the model in terms of the equivalent electric circuit and in terms of the Bergman approach to the effective medium. We realized that, for a thorough understanding of the experimental spectra, it is crucial to solve the wave equation for the propagation of THz wave in a nanostructured inhomogeneously optically excited semiconductor within the effective medium approximation. Analytical solutions of the wave equation in the context of the VBD model were then found and helped us to define a convenient methodology of Optical pump–THz probe experiments. The measurements with variable optical excitation fluence (preferentially by a few orders of magnitude) and their analysis within our theory are the key element for us in understanding of the microscopic nature of the response.
2. Semiconducting nanomaterials often exhibit contradictory properties when investigated by different methods, e.g. optical manifestation of quantum confinement of charge carriers vs. long-range electrical conductivity. It is important to understand the morphology of the sample — without neglecting the tails of the size distribution of semiconducting elements — because the diverse properties of a nanomaterial may originate in nanoelements of very different sizes and of vastly different number. We observed bulk-like THz conductivity in a sample of Si nanocrystals whose great majority exhibited photoluminescence due to quantum confinement. On the one hand, the numerous luminescent nanocrystals exhibited a negligible THz photoconductivity compared to the dominating response of several large highly photoconductive nanocrystals that were not eliminated during the fabrication of the sample. On the other hand, these large conductive nanocrystals do not manifest themselves in the photoluminescence analysis. We expect that this type of behavior will be

found quite often in semiconducting nanomaterials — i.e. that the response in optical methods will be dominated by nanoelements from a different part of their size distribution than the THz photoconductivity response. Monte Carlo calculations of nanoscopic charge transport are a great help in comprehending the impact of the size of a nanoelement on its photoconductive response.

THz photoconductivity spectra of nanoporous-Si-derived luminescent Si nanocrystals with a peak size of 2.8 nm were measured between 20 and 300 K. The spectra were interpreted within the VBD theory and the Monte Carlo calculation of carrier mobilities. This analysis revealed that the samples contain large (>60 nm) nanocrystals that are not detectable by the methods usually employed with nanomaterials partly due to their low concentration and partly due to their size — their dimensions are so large that they exhibit no quantum confinement. Nevertheless, these sparse large nanocrystals enable so high carrier mobilities that their photoconductive response completely dominates the THz photoconductive response at low carrier densities. The depolarization fields, which are usually seen as a complication in the response of composite materials, constituted a useful part of the experiment with variable excitation fluence — thanks to the coherent application of the VBD model — the response of the large nanocrystals was shifted above the investigated frequency range at increased excitation fluences and the conductivity spectrum of medium (~30 nm) nanocrystals was observed almost separately.

We measured also room-temperature THz photoconductivity of superlattices of isolated Si nanocrystals with a significantly narrower size distribution than in the previous case. The experimental spectra were found to be in an excellent agreement with the theoretical spectra given by the VBD effective medium theory and Monte Carlo calculations of carrier mobility with input parameters provided by (non-THz) microscopic imaging methods. Two types of clusters of connected nanocrystals occurred in two samples with higher amounts of Si per layer. Additional fitting of the response of these samples with the same method yielded the characteristic cluster sizes and the probability of inter-NC transport.

An in-depth analysis of the spatial and temporal behavior of carriers in heavily excited rutile monocrystal was performed and the general plasma diffusion model of interacting electrons and holes was formulated. Sets of THz photoconductivity spectra measured over a wide range of excitation fluences and pump–probe delays were successfully fitted with the global plasma diffusion model at low temperatures. It was found that electron–hole scattering plays an important role in charge transport at carrier densities above $\sim 10^{19} \text{ cm}^{-3}$. The values of the coefficients for electron–hole scattering and recombination as well as the low-density scattering times and masses of the two polaron types were found at low temperatures. We have namely found that hole polarons play a role comparable to that of electron polarons in THz conductivity in high quality rutile. The heavier ($12 m_e$) of the two polaron types exhibits scattering times of several ps and thus dominates the DC

transport as opposed to the lighter polaron ($7 m_e$) that has scattering time of several hundreds of fs at low temperatures.

At room temperature, we report a huge photoinduced transient contribution to the permittivity of 50 in a thin (~ 10 nm) photoexcited layer. This contribution is visible in the measured THz photoconductivity spectra of bulk rutile thanks to the fact that the carrier (polaron) mobility is decreased to $2 \text{ cm}^2\text{V}^{-1}\text{s}^{-1}$ at room temperature. This transient permittivity is probably related to a change of the polaron internal degrees of freedom (ionization and intra-polaronic transitions) due to the screening of the lattice permittivity in a high density polaron plasma.

By fitting of Monte Carlo carrier mobility spectra calculated in the probabilistic regime to spectra calculated in the morphological regime, we have found that the isotropic probability of inter-nanoparticle transport can be interpreted as the ratio of the carrier-permeable part of the surface of the nanoparticle to its total surface. However, this equality holds exactly only when the nanoparticle diameter is comparable to the mean free path of the carrier. Low values of the inter-nanoparticle transport probability in the case of large nanoparticles must be interpreted with caution.

11. Bibliography

- [1] M. A. Green, K. Emery, Y. Hishikawa, W. Warta, and E. D. Dunlop, *Prog. Photovolt. Res. Appl.* **23**, 1 (2015).
- [2] I. Pelant and J. Valenta, *Luminescence Spectroscopy of Semiconductors* (Oxford University Press, 2012).
- [3] H. Němec, P. Kužel, and V. Sundström, *J. Photochem. Photobiol. Chem.* **215**, 123 (2010).
- [4] V. Zajac, H. Němec, C. Kadlec, K. Kůsová, I. Pelant, and P. Kužel, *New J. Phys.* **16**, 093013 (2014).
- [5] S. A. Jensen, K.-J. Tielrooij, E. Hendry, M. Bonn, I. Rychetský, and H. Němec, *J. Phys. Chem. C* **118**, 1191 (2014).
- [6] C. Canali, F. Nava, and L. Reggiani, in *Hot-Electron Transp. Semicond.* (Springer Science & Business Media, 1985), pp. 87–111.
- [7] A. J. Macfaden, J. L. Reno, I. Brener, and O. Mitrofanov, *Appl. Phys. Lett.* **104**, 011110 (2014).
- [8] A. J. Huber, F. Keilmann, J. Wittborn, J. Aizpurua, and R. Hillenbrand, *Nano Lett.* **8**, 3766 (2008).
- [9] P. U. Jepsen, D. G. Cooke, and M. Koch, *Laser Photonics Rev.* **5**, 124 (2011).
- [10] W. Snodgrass, W. Hafez, N. Harff, and M. Feng, in *Electron Devices Meet. 2006 IEDM 06 Int.* (2006), pp. 1–4.
- [11] E. R. Mueller, *Coherent-DEOS Prod. Note 1* (2001).
- [12] J. Braine and D. H. Hughes, *Astron. Astrophys.* **344**, 779 (1999).
- [13] C. Sirtori, *Nature* **417**, 132 (2002).
- [14] J. S. Byrnes, editor, *Unexploded Ordnance Detection and Mitigation* (Springer, Dordrecht, 2009).
- [15] D. M. Pozar, *Microwave Engineering*, 1st Edition edition (Addison-Wesley, Reading, MA, 1990).
- [16] R. Sorrentino and G. Bianchi, *Microwave and RF Engineering* (John Wiley & Sons, Singapore, 2010).
- [17] D. H. Auston and K. P. Cheung, *J. Opt. Soc. Am. B* **2**, 606 (1985).
- [18] J. Hebling, G. Almasi, I. Kozma, and J. Kuhl, *Opt. Express* **10**, 1161 (2002).
- [19] H. Hirori, A. Doi, F. Blanchard, and K. Tanaka, *Appl. Phys. Lett.* **98**, 091106 (2011).
- [20] X.-C. Zhang, in *Laser Photonic Syst. Des. Integr.* (CRC Press, Taylor & Francis Group, LLC, n.d.), pp. 141–164.
- [21] J. Dai, J. Liu, and X.-C. Zhang, *Sel. Top. Quantum Electron. IEEE J. Of* **17**, 183 (2011).
- [22] F. Sizov, *Opto-Electron. Rev.* **18**, 10 (2010).
- [23] S. Kimura and H. Okamura, *J. Phys. Soc. Jpn.* **82**, 021004 (2012).
- [24] A. Pimenov, A. A. Mukhin, V. Y. Ivanov, V. D. Travkin, A. M. Balbashov, and A. Loidl, *Nat. Phys.* **2**, 97 (2006).
- [25] P. Kužel and F. Kadlec, *Comptes Rendus Phys.* **9**, 197 (2008).

- [26] P. Kužel and H. Němec, in *Terahertz Spectrosc. Imaging*, edited by K.-E. Peiponen, A. Zeitler, and M. Kuwata-Gonokami (Springer Berlin Heidelberg, 2012), pp. 569–610.
- [27] I. B. Vendik, O. G. Vendik, M. A. Odit, D. V. Kholodnyak, S. P. Zubko, M. F. Sitnikova, P. A. Turalchuk, K. N. Zemlyakov, I. V. Munina, D. S. Kozlov, V. M. Turgaliev, A. B. Ustinov, Y. Park, J. Kihm, and C. W. Lee, *IEEE Trans. Terahertz Sci. Technol.* **2**, 538 (2012).
- [28] B.-Y. Ung, B. M. Fischer, B.-H. Ng, and D. Abbott, in *Microelectron. MEMS Nanotechnol.* (International Society for Optics and Photonics, 2007), p. 67991E–67991E.
- [29] F. Rutz, M. Koch, S. Khare, M. Moneke, H. Richter, and U. Ewert, *Int. J. Infrared Millim. Waves* **27**, 547 (2006).
- [30] G. C. Trichopoulos and K. Sertel, *J. Infrared Millim. Terahertz Waves* **1** (2015).
- [31] R. M. Woodward, B. E. Cole, V. P. Wallace, R. J. Pye, D. D. Arnone, E. H. Linfield, and M. Pepper, *Phys. Med. Biol.* **47**, 3853 (2002).
- [32] K. Fukunaga and M. Picollo, *Appl. Phys. A* **100**, 591 (2010).
- [33] M. Tonouchi, *Nat. Photonics* **1**, 97 (2007).
- [34] B. Ferguson and X.-C. Zhang, *Nat. Mater.* **1**, 26 (2002).
- [35] A. Nahata, D. H. Auston, T. F. Heinz, and C. Wu, *Appl. Phys. Lett.* **68**, 150 (1996).
- [36] Q. Wu, M. Litz, and X.-C. Zhang, *Appl. Phys. Lett.* **68**, 2924 (1996).
- [37] Z. Mics, *Dynamics of Delocalized States in Molecular Systems Studied by Time-Resolved THz Spectroscopy*, Dissertation, Charles University in Prague, 2012.
- [38] P. Kužel and J. Petzelt, *Ferroelectrics* **239**, 79 (2000).
- [39] L. Duvillaret, F. Garet, and J.-L. Coutaz, *Sel. Top. Quantum Electron. IEEE J. Of* **2**, 739 (1996).
- [40] H. Němec, *Time-Resolved Terahertz Spectroscopy Applied to the Investigation of Magnetic Materials and Photonic Structures*, Dissertation, Charles University in Prague, 2006.
- [41] A. Pashkin, M. Kempa, H. Němec, F. Kadlec, and P. Kužel, *Rev. Sci. Instrum.* **74**, 4711 (2003).
- [42] P. Kužel, F. Kadlec, and H. Němec, *J. Chem. Phys.* **127**, 024506 (2007).
- [43] L. Fekete, P. Kužel, H. Němec, F. Kadlec, A. Dejneka, J. Stuchlík, and A. Fejfar, *Phys. Rev. B* **79**, 115306 (2009).
- [44] H. Němec, H.-K. Nienhuys, E. Perzon, F. Zhang, O. Inganäs, P. Kužel, and V. Sundström, *Phys. Rev. B* **79**, 245326 (2009).
- [45] P. Kužel and H. Němec, *J. Phys. Appl. Phys.* **47**, 374005 (2014).
- [46] H. Němec, V. Zajac, P. Kužel, P. Malý, S. Gutsch, D. Hiller, and M. Zacharias, *Phys. Rev. B* **91**, 195443 (2015).
- [47] Z. Mics, H. Němec, I. Rychetský, P. Kužel, P. Formánek, P. Malý, and P. Němec, *Phys. Rev. B* **83**, 155326 (2011).
- [48] H. Němec, J. Rochford, O. Taratula, E. Galoppini, P. Kužel, T. Polívka, A. Yartsev, and V. Sundström, *Phys. Rev. Lett.* **104**, 197401 (2010).

- [49] G. Gallot, J. Zhang, R. W. McGowan, T.-I. Jeon, and D. Grischkowsky, *Appl. Phys. Lett.* **74**, 3450 (1999).
- [50] J. Lloyd-Hughes and T.-I. Jeon, *J. Infrared Millim. Terahertz Waves* **33**, 871 (2012).
- [51] R. Ulbricht, E. Hendry, J. Shan, T. F. Heinz, and M. Bonn, *Rev. Mod. Phys.* **83**, 543 (2011).
- [52] H.-K. Nienhuys and V. Sundström, *Appl. Phys. Lett.* **87**, 012101 (2005).
- [53] P. Parkinson, J. Lloyd-Hughes, Q. Gao, H. H. Tan, C. Jagadish, M. B. Johnston, and L. M. Herz, *Nano Lett.* **7**, 2162 (2007).
- [54] J. Lloyd-Hughes, *Appl. Phys. Lett.* **100**, 122103 (2012).
- [55] T.-I. Jeon and D. Grischkowsky, *Appl. Phys. Lett.* **72**, 2259 (1998).
- [56] T.-I. Jeon and D. Grischkowsky, *Phys. Rev. Lett.* **78**, 1106 (1997).
- [57] M. C. Beard, G. M. Turner, and C. A. Schmuttenmaer, *Phys. Rev. B* **62**, 15764 (2000).
- [58] J. C. Dyre, *J. Appl. Phys.* **64**, 2456 (1988).
- [59] J. M. Pitarke, V. M. Silkin, E. V. Chulkov, and P. M. Echenique, *Rep. Prog. Phys.* **70**, 1 (2007).
- [60] J. C. M. Garnett, *Philos. Trans. R. Soc. Lond. Math. Phys. Eng. Sci.* **203**, 385 (1904).
- [61] J. C. M. Garnett, *Philos. Trans. R. Soc. Lond. Ser. Contain. Pap. Math. Phys. Character* **205**, 237 (1906).
- [62] J. E. Spanier and I. P. Herman, *Phys. Rev. B* **61**, 10437 (2000).
- [63] D. a. G. Bruggeman, *Ann. Phys.* **416**, 665 (1935).
- [64] D. J. Bergman, *Phys. Rep.* **43**, 377 (1978).
- [65] K. Ghosh and R. Fuchs, *Phys. Rev. B* **38**, 5222 (1988).
- [66] C. Pecharromán and F. J. Gordillo-Vázquez, *Phys. Rev. B* **74**, 035120 (2006).
- [67] I. Rychetský and J. Petzelt, *Ferroelectrics* **303**, 137 (2004).
- [68] D. J. Bergman, *Ann. Phys.* **138**, 78 (1982).
- [69] D. J. Bergman and D. Stroud, in *Solid State Phys.*, edited by H. E. and D. TURNBULL (Academic Press, 1992), pp. 147–269.
- [70] H. Němec, P. Kužel, and V. Sundström, *Phys. Rev. B* **79**, 115309 (2009).
- [71] R. Kubo, *J. Phys. Soc. Jpn.* **12**, 570 (1957).
- [72] J. Mrozek and H. Němec, *Phys. Rev. B* **86**, 075308 (2012).
- [73] N. V. Smith, *Phys. Lett. A* **26**, 126 (1968).
- [74] N. V. Smith, *Phys. Rev. B* **64**, 155106 (2001).
- [75] D. G. Cooke, A. N. MacDonald, A. Hryciw, J. Wang, Q. Li, A. Meldrum, and F. A. Hegmann, *Phys. Rev. B* **73**, 193311 (2006).
- [76] L. V. Titova, T. L. Cocker, D. G. Cooke, X. Wang, A. Meldrum, and F. A. Hegmann, *Phys. Rev. B* **83**, 085403 (2011).
- [77] E. Hendry, M. Koeberg, F. Wang, H. Zhang, C. de Mello Donegá, D. Vanmaekelbergh, and M. Bonn, *Phys. Rev. Lett.* **96**, 057408 (2006).
- [78] F. Wang, J. Shan, M. A. Islam, I. P. Herman, M. Bonn, and T. F. Heinz, *Nat. Mater.* **5**, 861 (2006).
- [79] J. A. Reedijk, L. J. Adriaanse, H. B. Brom, L. J. de Jongh, and G. Schmid, *Phys. Rev. B* **57**, R15116 (1998).

- [80] T.-I. Jeon, D. Grischkowsky, A. K. Mukherjee, and R. Menon, *Synth. Met.* **135–136**, 451 (2003).
- [81] G. M. Turner, M. C. Beard, and C. A. Schmittenmaer, *J. Phys. Chem. B* **106**, 11716 (2002).
- [82] E. Hendry, M. Koeberg, B. O'Regan, and M. Bonn, *Nano Lett.* **6**, 755 (2006).
- [83] H. Němec, P. Kužel, F. Kadlec, D. Fattakhova-Rohlfing, J. Szeifert, T. Bein, V. Kalousek, and J. Rathouský, *Appl. Phys. Lett.* **96**, 062103 (2010).
- [84] P. Tiwana, P. Parkinson, M. B. Johnston, H. J. Snaith, and L. M. Herz, *J. Phys. Chem. C* **114**, 1365 (2010).
- [85] P. Tiwana, P. Docampo, M. B. Johnston, H. J. Snaith, and L. M. Herz, *ACS Nano* **5**, 5158 (2011).
- [86] M. C. Beard, G. M. Turner, J. E. Murphy, O. I. Micic, M. C. Hanna, A. J. Nozik, and C. A. Schmittenmaer, *Nano Lett.* **3**, 1695 (2003).
- [87] M. C. Beard, G. M. Turner, and C. A. Schmittenmaer, *Nano Lett.* **2**, 983 (2002).
- [88] S. K. E. Merchant, J. Lloyd-Hughes, L. Sirbu, I. M. Tiginyanu, P. Parkinson, L. M. Herz, and M. B. Johnston, *Nanotechnology* **19**, 395704 (2008).
- [89] T. L. Cocker, L. V. Titova, S. Fourmaux, H.-C. Bandulet, D. Brassard, J.-C. Kieffer, M. A. E. Khakani, and F. A. Hegmann, *Appl. Phys. Lett.* **97**, 221905 (2010).
- [90] P. Parkinson, H. J. Joyce, Q. Gao, H. H. Tan, X. Zhang, J. Zou, C. Jagadish, L. M. Herz, and M. B. Johnston, *Nano Lett.* **9**, 3349 (2009).
- [91] H. J. Joyce, C. J. Docherty, Q. Gao, H. H. Tan, C. Jagadish, J. Lloyd-Hughes, L. M. Herz, and M. B. Johnston, *Nanotechnology* **24**, 214006 (2013).
- [92] H. J. Joyce, J. Wong-Leung, C.-K. Yong, C. J. Docherty, S. Paiman, Q. Gao, H. H. Tan, C. Jagadish, J. Lloyd-Hughes, L. M. Herz, and M. B. Johnston, *Nano Lett.* **12**, 5325 (2012).
- [93] P. Parkinson, C. Dodson, H. J. Joyce, K. A. Bertness, N. A. Sanford, L. M. Herz, and M. B. Johnston, *Nano Lett.* **12**, 4600 (2012).
- [94] D. G. Cooke, F. A. Hegmann, Y. I. Mazur, W. Q. Ma, X. Wang, Z. M. Wang, G. J. Salamo, M. Xiao, T. D. Mishima, and M. B. Johnson, *Appl. Phys. Lett.* **85**, 3839 (2004).
- [95] D. G. Cooke, F. A. Hegmann, Y. I. Mazur, Z. M. Wang, W. Black, H. Wen, G. J. Salamo, T. D. Mishima, G. D. Lian, and M. B. Johnson, *J. Appl. Phys.* **103**, 023710 (2008).
- [96] C. S. Ponseca Jr, H. Němec, J. Wallentin, N. Anttu, J. P. Beech, A. Iqbal, M. Borgström, M.-E. Pistol, L. Samuelson, and A. Yartsev, *Phys. Rev. B* **90**, 085405 (2014).
- [97] H. Nemeč, V. Zajac, I. Rychetsky, D. Fattakhova-Rohlfing, B. Mandlmeier, T. Bein, Z. Mics, and P. Kuzel, *IEEE Trans. Terahertz Sci. Technol.* **3**, 302 (2013).
- [98] I. Rychetský and A. Klíč, *Ferroelectrics* **427**, 143 (2012).
- [99] H. Němec, F. Kadlec, and P. Kužel, *J. Chem. Phys.* **117**, 8454 (2002).
- [100] M. Abramowitz and I. A. Stegun, *Handbook of Mathematical Functions: With Formulas, Graphs, and Mathematical Tables*, 10th edn (Dover Publications, inc., New York, 1964).

- [101] K. Dohnalová, L. Ondič, K. Kůsová, I. Pelant, J. L. Rehspringer, and R.-R. Mafouana, *J. Appl. Phys.* **107**, 053102 (2010).
- [102] L. Ondič, K. Kůsová, M. Ziegler, L. Fekete, V. Gärtnerová, V. Cháb, V. Holý, O. Cibulka, K. Herynková, M. Gallart, P. Gilliot, B. Hönerlage, and I. Pelant, *Nanoscale* **6**, 3837 (2014).
- [103] P. Němec, I. Němec, P. Nahálková, Y. Němcová, F. Trojánek, and P. Malý, *Thin Solid Films* **403–404**, 9 (2002).
- [104] M. Zacharias, J. Heitmann, R. Scholz, U. Kahler, M. Schmidt, and J. Bläsing, *Appl. Phys. Lett.* **80**, 661 (2002).
- [105] S. Gutsch, D. Hiller, J. Laube, M. Zacharias, and C. Kübel, *Beilstein J. Nanotechnol.* **6**, 964 (2015).
- [106] M. Jivanescu, D. Hiller, M. Zacharias, and A. Stesmans, *EPL Europhys. Lett.* **96**, 27003 (2011).
- [107] S. Gutsch, *Electronic Transport in Ordered Silicon Nanocrystal Networks*, Dissertation, Albert-Ludwigs-Universität Freiburg im Breisgau, 2014.
- [108] S. Gutsch, J. Laube, A. M. Hartel, D. Hiller, N. Zakharov, P. Werner, and M. Zacharias, *J. Appl. Phys.* **113**, 133703 (2013).
- [109] J. López-Vidrier, Y. Berencén, S. Hernández, O. Blázquez, S. Gutsch, J. Laube, D. Hiller, P. Löper, M. Schnabel, S. Janz, M. Zacharias, and B. Garrido, *J. Appl. Phys.* **114**, 163701 (2013).
- [110] M. Kořínek, M. Kozák, F. Trojánek, D. Hiller, A. Hartel, S. Gutsch, M. Zacharias, and P. Malý, *Phys. E Low-Dimens. Syst. Nanostructures* **56**, 177 (2014).
- [111] D. G. Cooke, A. Meldrum, and P. U. Jepsen, *Appl. Phys. Lett.* **101**, 211107 (2012).
- [112] K. Židek, F. Trojánek, P. Malý, L. Ondič, I. Pelant, K. Dohnalová, L. Šiller, R. Little, and B. R. Horrocks, *Opt. Express* **18**, 25241 (2010).
- [113] B. Mills, *Ball-and-Stick Model of Part of the Crystal Structure of Rutile, One of the Mineral Forms of Titanium Dioxide, TiO₂*. (2007).
- [114] V. Zajac, H. Němec, and P. Kužel, *Phys. Rev. B* **94**, 115206 (2016).
- [115] W. G. Spitzer, R. C. Miller, D. A. Kleinman, and L. E. Howarth, *Phys. Rev.* **126**, 1710 (1962).
- [116] W. H. Baur, *Acta Crystallogr.* **9**, 515 (1956).
- [117] M. Cardona and G. Harbeke, *Phys. Rev.* **137**, A1467 (1965).
- [118] E. Hendry, M. Koeberg, J. Pijpers, and M. Bonn, *Phys. Rev. B* **75**, 233202 (2007).
- [119] C. Jacoboni, *Theory of Electron Transport in Semiconductors: A Pathway from Elementary Physics to Nonequilibrium Green Functions* (Springer Science & Business Media, 2010).
- [120] M. Dou and C. Persson, *J. Appl. Phys.* **113**, 083703 (2013).
- [121] J. Yahia, *Phys. Rev.* **130**, 1711 (1963).
- [122] D. S. Boudreaux, F. Williams, and A. J. Nozik, *J. Appl. Phys.* **51**, 2158 (1980).
- [123] J. J. Kasinski, L. A. Gomez-Jahn, K. J. Faran, S. M. Gracewski, and R. J. D. Miller, *J. Chem. Phys.* **90**, 1253 (1989).
- [124] C. Kormann, D. W. Bahnemann, and M. R. Hoffmann, *J. Phys. Chem.* **92**, 5196 (1988).

- [125] B. Enright and D. Fitzmaurice, *J. Phys. Chem.* **100**, 1027 (1996).
- [126] C. Persson and A. Ferreira da Silva, *Appl. Phys. Lett.* **86**, 231912 (2005).
- [127] K. M. Glassford and J. R. Chelikowsky, *Phys. Rev. B* **46**, 1284 (1992).
- [128] E. Hendry, F. Wang, J. Shan, T. F. Heinz, and M. Bonn, *Phys. Rev.-Ser. B-* **69**, 081101 (2004).
- [129] J. Pascual, J. Camassel, and H. Mathieu, *Phys. Rev. B* **18**, 5606 (1978).
- [130] A. Pashkin, M. Porer, M. Beyer, K. W. Kim, A. Dubroka, C. Bernhard, X. Yao, Y. Dagan, R. Hackl, A. Erb, J. Demsar, R. Huber, and A. Leitenstorfer, *Phys. Rev. Lett.* **105**, 067001 (2010).
- [131] A. Grünebohm, P. Entel, and C. Ederer, *Phys. Rev. B* **87**, 054110 (2013).
- [132] F. Gervais and B. Piriou, *Phys. Rev. B* **10**, 1642 (1974).
- [133] D. Emin, *Phys. Rev. B* **48**, 13691 (1993).
- [134] H. Sezen, M. Buchholz, A. Nefedov, C. Natzeck, S. Heissler, C. Di Valentin, and C. Wöll, *Sci. Rep.* **4**, (2014).

12. List of Tables

Table 2.1	Borders of THz frequency range overlapping with common optical and electronic ranges of electromagnetic radiation.....	5
Table 2.2	Characteristics of the OPTP experimental setup. *The excitation density at the edge of the aperture is at least 67% of that in its center.	17
Table 6.1	Properties and fractions of individual Si compounds in the sample powder.	66
Table 6.2	Summary of the optical and steady-state THz properties of the samples.	69
Table 7.1	Properties of investigated Si-NC/SiO ₂ superlattices.	82
Table 7.2	THz fit parameters.....	88
Table 8.1	Characteristics of bulk rutile.	93
Table 8.2	Coefficients of carrier transport and decay in rutile ($E \perp c$) as obtained from THz photoconductivity. Indices Lt and Hv denote respectively the lighter and heavier of the electron and hole polarons. In [118] electrons were considered as the much more mobile carrier type. The error values are standard deviations provided by the fit.	103

13. List of Abbreviations

Real and imaginary components of complex quantities are standardly denoted with single and double primes, respectively: $X = X' + iX''$. The sign convention $E(t) \propto e^{-i\omega t}$, $\varepsilon = \varepsilon' + i\varepsilon'' = +i\sigma/(\omega\varepsilon_0)$ is used.

13.1. Multi-letter abbreviations

AFM	atomic force microscope/y
BBO	β -barium borate
CC	Cole-Cole <i>conductivity model</i> (Section 3.1)
CD	Cole-Davidson <i>conductivity model</i> (Section 3.1)
cw	continuous-wave
c-Si	crystalline silicon
DC	direct current
DS	Drude-Smith <i>conductivity model</i> (Section 3.7)
EFTEM	energy-filtered transmission electron microscopy
EMT	effective medium theory
FIR	far-infrared
Ln	the principal value of the complex logarithm function
LP	localized plasmon <i>conductivity model</i> (3.5)
MBE	molecular-beam epitaxy
MG	Maxwell Garnett <i>EMT</i>
NC	nanocrystal
NP	nanoparticle
NW	nanowire
OPTP	optical pump–THz probe <i>spectroscopy, spectrum, method</i> (Section 2.3)
OR	optical rectification (p. 17)
PM	power meter
QCL	quantum cascade laser (p. 6)
QD	quantum dot
TEM	transmission electron microscopy
TDS	time-domain spectroscopy (Section 2.2)
XPS	X-ray photoelectron <i>spectroscopy, spectrum</i>

13.2. Roman symbols and their derivatives

The prefix “ Δ ” of transient quantities is disregarded in the alphabetical ordering of the list. Parentheses point to the introduction or definition of the symbol.

a	<i>in</i> Chapter 8 — proportionality constant of electron–hole scattering rate (8.2)
	<i>in</i> Chapter 9 — lattice constant of a periodical arrangement of nanospheres
	<i>elsewhere</i> — sum of Fabry-Pérot reflections of the probe pulse field in the sample (5.3)
a_B	Bohr radius of electron in the hydrogen-like potential of a polaron (8.4)

- $A_{1,2}$ coefficients of the homogeneous solution of the wave equation (5.5)
 b proportionality constant of carrier–phonon scattering rate (8.2, 8.3)
 $b_{e,h}$ b specifically for electrons, holes (8.9)
 $b_{Hv,Lt}$ b for the heavier, lighter polaron type (Subsection 8.1.4)
 B in Chapter 8 — bimolecular recombination rate
elsewhere — morphological parameter of the VBD effective medium model
 c speed of light in vacuum, 2.997925×10^8 m/s
 c_p carrier velocity persistence parameter in the DS approach (Section 3.7)
 C_p percolation factor of the photoconductive component in Bergman EMT
 d in Chapter 8 — characteristic thickness of carrier plasma
elsewhere — (nano)particle diameter
 $\langle d \rangle_{a^2}$ mean value of area-weighted NC diameters (Chapter 7)
 D in Chapter 9 — nanoparticle diameter
elsewhere — morphological parameter of the VBD effective medium model
 $D_{A,e,h}$ ambipolar, electron, hole, diffusion coefficient, respectively (8.6,8.7)
 D_{Hv} diffusion coefficient of the heavier polaron type (8.13)
 (THz) electric field:
 E — in the sample, averaged in the xy plane, $E = E_{\text{probe}} + \Delta E$
 ΔE — transient contribution to E induced by photoexcitation
 E_{inc} — of the probe pulse incident on the sample (5.2)
 E_{loc} — local electric field inside a polarizable inclusion (3.12)
 E_{probe} — of the probe pulse inside the sample
 E_t — of the probe pulse transmitted through sample
 ΔE_t — transient part of E_t induced by photoexcitation
 ΔE_t^{max} — maximum of the THz waveform in the time domain
 E_t^{ref} — electric field transmitted through a reference sample (2.1)
 ΔE_r — transient part of THz probe field reflected from the sample due to photoexcitation (5.7)
 Energy of electron in hydrogen-like potential of a polaron in rutile (Section 8.4):
 E_{1s} on level $1s$
 E_{2p} on level $2p$
 E_{ion} ionization energy
 e elementary charge, 1.60219×10^{-19} C
 F in Section 3.3 — oscillator strength
elsewhere — 2-argument version of ${}_2F_1$ (5.30)
 ${}_2F_1$ Gaussian hypergeometric function [100]
 F_n residuum in the discrete representation of the Bergman EMT (3.26)
 f_{EMT} EMT function or functional (3.8)
 f_{rep} repetition rate of the pump (source) laser
 g, g_{ext} alternative expressions for the Bergman spectral distribution
 $G(z)$ particular solution of the wave equation (5.5)
 ΔH transient part of THz magnetic field in the sample induced by photoexcitation

h, \hbar	Planck constant 6.6262×10^{-34} J·s, reduced Planck constant $\hbar/2\pi$
j	general summation index
Δj	transient current
K	shape factor of the photoconductive component of a composite
K_{box}	the fraction of measured pump power that is incident on the probed area of the sample (Section 2.4)
k	wavenumber of the wave in a medium
k_0	wavenumber of the wave in vacuum
k_B	Boltzmann constant
L	sample thickness
L_{layer}	thickness of the SiO _x layer in a superlattice
l_{diff}	carrier diffusion length
l_{free}	carrier mean free path between collision in the bulk
m_a	atomic mass of a chemical compound
m_e	electron rest mass
m^*	carrier effective conductivity mass
$m_{e,h}^*$	electron, hole polaron effective mass (8.8)
$m_{\text{Hv,Lt}}^*$	effective mass of the heavier, lighter polaron type (Subsection 8.1.4)
m^{DOS}	carrier density-of-states mass (8.3)
N	(photo)carrier density
N_0	N at the photoexcited surface
N_0^{mic}	N in semiconducting particles at the photoexcited surface
N^{av}	average excitation density $\approx 0.63\alpha\phi$ (footnote 19 in [118])
$N_{e,h}$	density of electrons, holes (Chapter 8)
N_S	carrier <i>sheet</i> density (Subsection 8.3.1)

Complex refractive index:

n	— of the sample (with or without photoexcitation)
n_1	— of the medium in front of the photoexcited layer
n_2	— of the medium behind the photoexcited layer
n_{group}	group refractive index of an optical pulse in a non-linear medium
P	polarization of a medium (3.12, 3.13)
P_{inc}	pump light power incident on the probed area of the sample (Section 2.4)
P_{meas}	pump light power measured by a power meter before the vacuum box (Section 2.4)
p	order number of carrier collisions in the DS approach (Section 3.7)

Probability of the result of a charge carrier hitting the NP boundary in Monte Carlo simulations:

p_B	— carrier backscattering off the NP boundary
$p_{F,d}, p_{F,\delta}$	— carrier transport between adjacent NCs with diameter d, δ
p_R	— carrier reflection from the NP boundary
p_S	— isotropic scattering carrier at the boundary
p_T	— scatterless carrier transport to adjacent NP (tunneling)

R	power reflectivity of the sample front face for the pump light
r	radius of the sample holder aperture
$r_{1,2}$	amplitude reflection coefficient at the sample front, back surface (5.4)
s	volume filling fraction of the photoconductive component of a composite
s_{area}	areal filling fraction of Si precipitates in an annealed layer (Chapter 7)
s_d	volume filling fraction of smaller nanocrystals (Chapter 7)
s_δ	volume filling fraction of larger clusters (Chapter 7)
t	time delay between the peak of the probe pulse and the sampling pulse
t'	time from the start of the motion of a carrier in a Monte Carlo simulation (3.28)
t_B	characteristic time of bimolecular recombination (8.18)
t_p	time delay between the pump pulse and the peak of the probe pulse
Complex amplitude transmission coefficient:	
t_1	— at the front surface of the sample (5.4)
t_2	— at the back surface of the sample (5.4)
t_{sample}	— of the sample without photoexcitation (2.1)
t_{ref}	— of the reference (2.1)
T (<i>without argument</i>) — thermodynamic temperature	
Complex field transmittance:	
$T(\omega)$	— of the sample (without photoexcitation, (2.1))
ΔT	— transient part of $T(\omega)$ induced by photoexcitation (2.5)
ΔT_{norm}	— normalized transient transmittance, i.e. $\Delta T(\omega)$ per single absorbed photon per elementary charge (2.10)
$\Delta T_{\text{norm}}^{\text{perc}}$	— ΔT_{norm} of a percolated sample (5.16)
$\Delta T_{\text{norm}}^{\text{non-perc}}$	— ΔT_{norm} of a non-percolated sample (5.35)
$\Delta T_{\text{norm}}^{\text{linear}}$	— ΔT_{norm} of a non-percolated component in the linear (low-conductivity) regime (6.3)
U	source function of ΔE in the wave equation (2.3, 2.4)
v_i	velocity vector coordinates (3.28)
v	amplitude of the representative contribution to the Bergman spectral distribution in the VBD approximation (4.12)
$v(l)$	Bergman spectral distribution
V, V_p	percolation strength of the photoconductive component in the Bergman and in the VBD effective medium theory
$V_{d,\delta}$	percolation strength of NCs with diameter d, δ (Chapter 7)
V_m	percolation strength of the dielectric matrix in the Bergman EMT
V_S	volume of a sphere
V_Σ	unit cell volume in Monte Carlo simulations (Chapter 9)
x	oxygen-to-silicon content ratio in SiO_x oxides

Z	capacitive impedance spectrum of the non-percolated component in the VBD approximation (5.27)
Z_0	vacuum wave impedance = $1/(\epsilon_0 \cdot c)$
z	Cartesian coordinate along the probe pulse propagation, \perp to the sample surface

13.3. Greek symbols and their derivatives

The prefix “ Δ ” of transient quantities is disregarded in the alphabetical ordering of the list. Parentheses point to the introduction or definition of the symbol.

α	(effective) absorption coefficient of the pump light in the sample
α^{mic}	absorption coefficient of the pump light in the photoconductive inclusions of a composite
β	Cole-Davidson exponent (3.3)
γ	damping rate of a driven harmonic oscillator (3.5)
Γ	the gamma function
δ	<i>in</i> Section 3.1 — Cole-Cole exponent (3.3) <i>in</i> Subsection 4.5.1 — parameter of the residual theorem (4.18) <i>in</i> Chapter 7 — fitted diameter of larger nanocrystal aggregates

Complex permittivity:

ϵ	— (<i>macroscopic</i>) of a composite = effective permittivity
$\Delta\epsilon$	— the transient part of ϵ induced by photoexcitation
ϵ_0	— of vacuum, 8.854185×10^{-12} F/m
$\Delta\epsilon_{\text{Drude}}$	— permittivity contribution of photocarriers in the Drude model
ϵ_{m}	— (<i>microscopic</i>) of insulating parts (matrix) of a two-component composite
ϵ_{p}	— (<i>microscopic</i>) of photoconductive parts of a two-component composite
$\Delta\epsilon_{\text{p}}$	— the transient part of ϵ_{p} induced by photoexcitation
ϵ_{pol}	— dielectric strength of polaron ionization response (8.23)
η	proportionality constant between ω_0 and ω_{p} (3.6)
θ	relaxation time in the Debye conductivity model (3.7)
ϑ	carrier scattering angle in the DS approach (Section 3.7)
κ	auxiliary argument of the hypergeometric function (5.30)
κ^*	complex conjugate of κ
A	depolarization factor of in the Bergman EMT (Subsection 3.4.3)
λ	wavelength, central wavelength of an ultrashort pulse

Charge carrier mobility:

μ	— in general
$\mu_{d,\delta}$	— in NCs with diameter d , δ calculated by Monte Carlo method (Chapter 7)
μ_{Drude}	— according to the Drude model (3.1)
$\mu_{\text{Drude-Smith}}$	— according to the Drude-Smith model (3.30)
$\mu_{\text{e,h}}$	— of electron, hole polarons (8.8)
$\mu_{\text{Hv,Lt}}$	— of the heavier, lighter polaron type (Subsection 8.1.4)

μ_H	— in the DC limit of the Dyre’s hopping model (Section 3.2)
μ_{ij}	— calculated from Kubo formula (<i>tensor</i> , (3.28))
μ_0	vacuum permeability (5.6)
ν	linear frequency
ξ	quantum yield of photogeneration of mobile carriers
$\xi_{H,L}$	fraction of photogenerated carriers in the high- and low-density region (8.12)
ρ	(mass) density of a material
$\Delta\Sigma$	transient sheet conductivity (5.41)
Σ_R	ratio of the reflective area of the boundary of a unit cell versus the total surface of the unit cell (Chapter 9)

Complex conductivity:

σ	— <i>macroscopic</i> (effective) conductivity of a sample
$\Delta\sigma$	— transient part of σ induced by photoexcitation
$\Delta\sigma^{\text{av}}$	— averaged for all photocarriers across the excited region (8.1)
$\Delta\sigma^{\text{mic}}$	— <i>microscopic</i> transient photoconductivity of photoconductive parts of a two-component composite (Section 3.4)
$\Delta\sigma_0^{\text{mic}}$	— $\Delta\sigma^{\text{mic}}$ at the photoexcited surface (5.11)
$\Delta\sigma^{\text{perc}}$	— transient <i>macroscopic</i> (effective) conductivity of a percolated material/component (5.12)
$\Delta\sigma^{\text{non-perc}}$	— transient <i>macroscopic</i> (effective) conductivity of a non-percolated material/component in the VBD approximation (5.24)
τ_0	scattering time of charge carriers in the low-density limit (8.2)
$\tau_{0e,h}$	scattering time of electrons, holes in the low-density limit (8.9)
$\tau_{0Hv,Lt}$	scattering time of the heavier, lighter polaron type in the low-density limit (Subsection 8.1.4)
τ_A	scattering time of charge carriers on acoustic phonons (8.3)
τ^{av}	characteristic scattering time of carriers distributed in sample with a varying concentration (8.1)
τ_{DS}	characteristic time of the DS model (Section 3.7)
τ_H	scattering time of charge carriers in the high-density plasma region (8.12)
τ_S	scattering time of charge carriers in the Drude model (3.2)
τ_{max}	maximal time of charge carrier hopping (Section 3.2)
τ_{min}	minimal time of charge carrier hopping (Section 3.2)

Pump photon fluence in a single excitation pulse:

ϕ	— transmitted through the front interface of the sample = the true excitation photon fluence
ϕ_{inc}	— incident on the sample front surface
$\chi^{(2)}$	second-order susceptibility tensor (2.12)
Ω_0	(central) frequency of an optical pulse
$\Delta\Omega$	bandwidth of an optical pulse

- ω angular frequency — Fourier counterpart of time t . All spectra are plotted against linear frequency $\omega/2\pi$.
- ω_0 undamped resonance frequency of a harmonic oscillator (3.5)
- $\Delta\omega_0$ frequency shift of phonon mode
- ω_p on Page 11 — Fourier counterpart of pump–probe delay t_p
elsewhere — plasma frequency of charge carrier ensemble (3.6)